MAGNETIC RESONANCE STUDIES OF PARAMAGNETIC CENTRES IN OXIDE CRYSTALS

by

P. McGeehin B.A.

Being a thesis
submitted to the University of Keele
for the Degree of Doctor of Philosophy

Department of Physics,
University of Keele,
Keele, Staffordshire.

April, 1974.

ABSTRACT

The results reported in this thesis were obtained using Electron Paramagnetic Resonance. Studies were made of previously neutron irradiated crystals of $CaWO_4$ and CaO, and of the system $CaO : Gd^{3+}$.

A spectrum in a heavily neutron irradiated sample of $CaWO_4$ was observed only below 120 K. At 77 K it was described by the tetragonal spin Hamiltonian ($S = \frac{1}{2}$, $I = 5/2$)

$$\mathcal{H} = g_{\parallel} \mu_B B_z S_z + g_{\perp} \mu_B (B_x S_x + B_y S_y) + A_{\parallel} S_z I_z + A_{\perp} (S_x I_x + S_y I_y)$$

with parameters

$$g_{\parallel} = 1.8491 \pm 0.0003$$
$$g_{\perp} = 1.7162 \pm 0.0003$$
$$A_{\parallel} = 0.0030 \pm 0.0003 \ cm^{-1}$$
$$A_{\perp} = 0.0331 \pm 0.0003 \ cm^{-1} .$$

By considering various nuclear reaction schemes it is shown that the spectrum is probably due to Re^{6+} generated by nuclear transmutation of tungsten during irradiation. At 4.2 K absorption lines from both Re^{185} and Re^{187} exhibiting tetragonal symmetry were observed, the spin Hamiltonian parameters being, for Re^{187}

$$g_{\parallel} = 1.8549 \pm 0.0002$$
$$g_{\perp} = 1.7164 \pm 0.0002$$
$$A_{\parallel} = 0.0042 \pm 0.0002 \ cm^{-1}$$
$$A_{\perp} = 0.0324 \pm 0.0002 \ cm^{-1}$$

and for Re^{185}, assuming the same parameters parallel to the unique axis,

$$g_{\perp} = 1.7167 \pm 0.0002$$
$$A_{\perp} = 0.0321 \pm 0.0002 \ cm^{-1} .$$

As expected, the concentration ratio of these two isotopes in the crystal was different from that found in nature. Preliminary ENDOR experiments showed conclusively that rhenium was responsible for the spectrum, the nuclear g-factor for the most abundant isotope in the

crystal, Re^{187}, being

$$g_N = 1.27 .$$

By studying the large number of forbidden transitions in the spectrum at 4.2 K the value

$$P_{||} = -0.0008 \pm 0.0003 \ cm^{-1}$$

was determined for the axial nuclear electric quadrupole parameter in the spin Hamiltonian. The variation of the spectrum linewidth was also investigated as a function of both angle in the crystal ab plane and temperature.

Two new aspects of the CaO : Gd^{3+} system are reported. Firstly, forbidden $\Delta M_S = 2$, 3, 4 and 5 transitions of the usual cubic spectrum were observed, and the sign of the principal crystal field parameter in the spin Hamiltonian describing this spectrum was confirmed to be negative. Secondly, a spectrum due to Gd^{3+} in sites of orthorhombic symmetry was observed. The zero field splitting of this spectrum is larger than the energy of the X-band quantum, resulting in a complex angular variation. Using the parameters given in Table 4.2 the spectrum at Q-band was fitted to the spin Hamiltonian ($S = 7/2$)

$$\mathcal{H} = g \mu_B \underline{B}.\underline{S} + \frac{1}{3}(b_2^0 O_2^0 + b_2^2 O_2^2) + \frac{1}{60}(b_4^0 O_4^0 + b_4^2 O_4^2 + b_4^4 O_4^4) + \frac{1}{1260}(b_6^0 O_6^0 + b_6^2 O_6^2 + b_6^4 O_6^4 + b_6^6 O_6^6) .$$

The x, y and z axes of the centre are $\langle 110 \rangle$, $\langle \bar{1}10 \rangle$ and $\langle 001 \rangle$ crystal axes. Models for the crystal field surrounding the ion are discussed.

A spectrum exhibiting motional averaging effects was observed in a sample of high purity, neutron irradiated, CaO. At 77 K the motion was frozen in, producing an orthorhombic spectrum described by the spin Hamiltonian ($S = \frac{1}{2}$, $I = \frac{1}{2}$)

$$\mathcal{H} = \mu_B(g_z S_z B_z + g_y S_y B_y + g_x S_x B_x) + A_z S_z I_z + A_y S_y I_y + A_x S_x I_x$$

with parameters

$$g_x = 2.0088 \pm 0.0001$$
$$g_y = 2.0042 \pm 0.0001$$
$$g_z = 2.0074 \pm 0.0001$$
$$A_x = 0.0040 \pm 0.0001 \ cm^{-1}$$
$$A_y = 0.0079 \pm 0.0001 \ cm^{-1}$$
$$A_z = 0.0044 \pm 0.0001 \ cm^{-1} \ .$$

The z axis of the spectrum is parallel to crystal $\langle 100 \rangle$ axes. x and y axes are at both 35° and 55° to $\langle 100 \rangle$ axes in the $\{100\}$ plane perpendicular to the z axis. A major change in the spectrum occurred in the temperature range 180 - 210 K, when two sets of lines coalesced. At room temperature this motionally averaged spectrum was described by the axial spin Hamiltonian given above, with $S = \frac{1}{2}$ and $I = \frac{1}{2}$. The parameters were

$$g_{\parallel} = 2.0067 \pm 0.0001$$
$$g_{\perp} = 2.0064 \pm 0.0001$$
$$A_{\parallel} = 0.0077 \pm 0.0001 \ cm^{-1}$$
$$A_{\perp} = 0.0051 \pm 0.0001 \ cm^{-1} \ .$$

The unique axis was parallel to $\langle 100 \rangle$ crystal axes. By considering the variation in linewidth of the spectrum above the transition temperature the activation energy of the reorientation motion was found to be 0.07 eV. A detailed model for the centre incorporating the molecular ion OH^{2-} is proposed.

ACKNOWLEDGMENTS

The author would like to thank:

Professor D.J.E. Ingram for the provision of research facilities.

Dr.B.Henderson for his encouragement, supervision and stimulating conversation.

Dr.A.E.Hughes of UKAEA, Harwell for the provision of experimental crystals.

Dr.D.E.Dugdale and other members of the Physics Department for stimulating discussions.

Dr.R.Dowsing of University College, Swansea and Mr.Paul Collis of the Computer Centre, Keele for programming assistance.

The Technical Staff of the Physics Department for their help and cooperation.

The Science Research Council for supporting the research programme and providing a maintenance grant, and UKAEA, Harwell, for additional financial support.

His wife, Faye, for encouragement and for the care and patience involved in typing this thesis.

CONTENTS

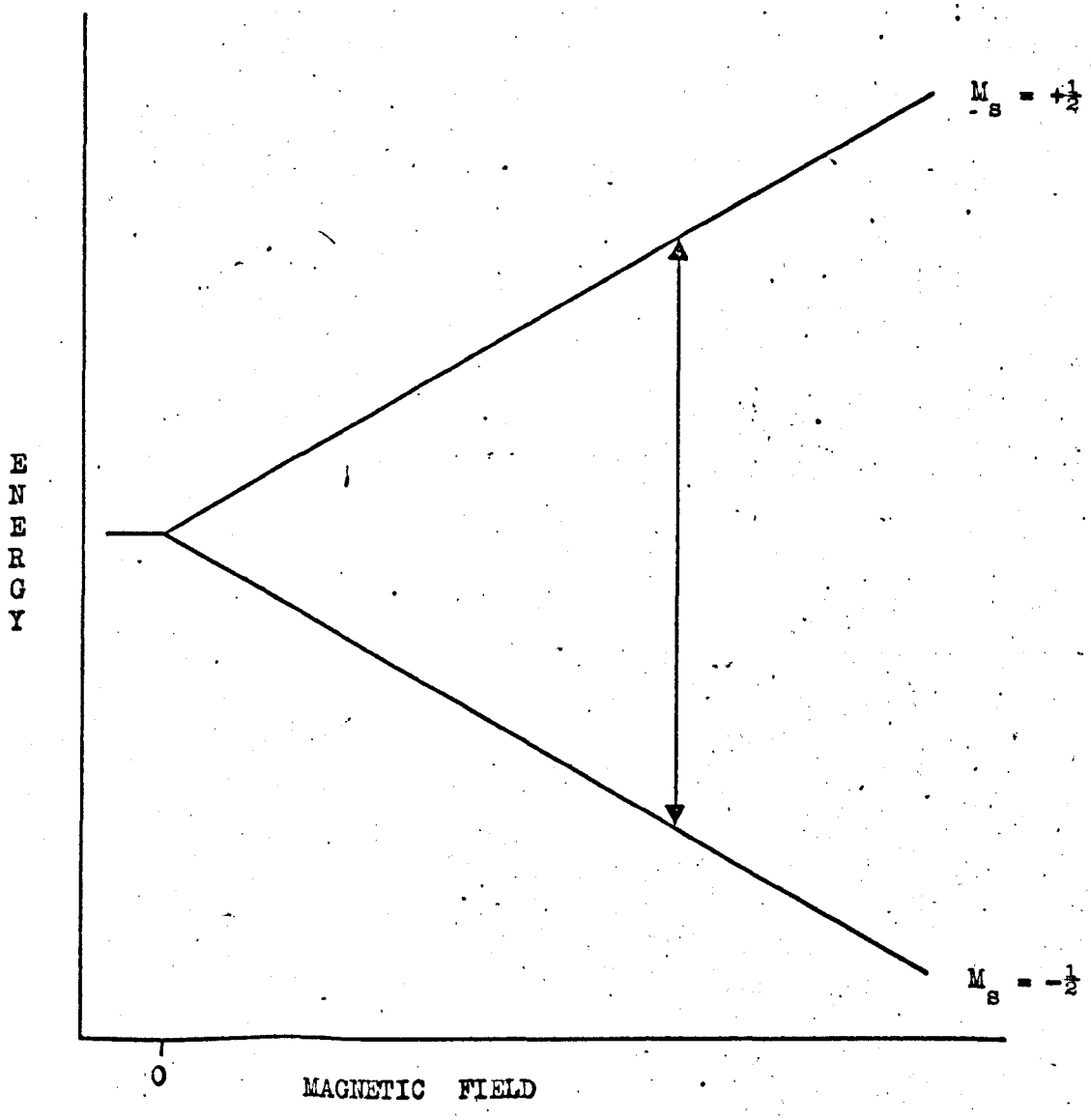

FIGURE 1.1 Diverging energy levels of an electron in a magnetic field. The vertical arrow indicates a transition which can occur when the energy of the incident microwave quantum equals the energy difference between the two levels.

CHAPTER I

THEORY OF ELECTRON PARAMAGNETIC RESONANCE

1.1 Introduction

This chapter summarizes the theoretical background needed to interpret the experimental results obtained from the application of electron paramagnetic resonance in solid state physics.

The electron paramagnetic resonance (EPR) experiment involves the measurement of the magnetic field at which atoms or ions with a permanent magnetic moment absorb microwave energy. An isolated ion with total angular momentum $J\hbar$ has an associated magnetic moment $-g_J \mu_B \underline{J}$ where g_J is the Landé g-factor, μ_B is the Bohr Magneton, and $\hbar$ is Planck's constant. In an external magnetic field B the $2J + 1$ states identified by their magnetic quantum number M_J have energy $M_J g \mu_B B$, where the g-factor is only equal to g_J when there is negligible interaction between the ion and its surroundings. In the simplest case $J = S = \frac{1}{2}$ and the two energy levels $M_S = \pm\frac{1}{2}$ diverge with energy according to figure 1.1. A transition, indicated by the arrow, occurs when the energy difference between the states is equal to that of the applied microwave field:

$$h\nu = g \mu_B B. \qquad 1.1$$

The behaviour of the magnetic moment when a transition occurs can be described in classical terms. In a magnetic field B the magnetic moment μ precesses about B with an angular frequency $\omega_J = g_J \mu_B B / \hbar$. A magnetic field B_1 rotating at ω_J in the same sense as the magnetic moment and applied perpendicular to B exerts a constant torque on the magnetic moment. In the frame of reference rotating at ω_J about B the magnetic moment precesses about B_1 with an angular frequency $\omega_1 = + g_J \mu_B B_1 / \hbar$. Every half cycle of this motion it changes from being parallel to B to being antiparallel, so there is an alternating

component of the magnetic moment perpendicular to B and the magnetic moment can exchange energy with the oscillating field.

According to equation 1.1 for $g = 2$ and $\nu = 10$ GHz, $B \sim 0.35$ T. As sensitivity decreases at lower frequencies, and magnetic fields higher than 1.6 T are not easily generated, most experimental work has been done at frequencies near to 10 GHz, corresponding to wavelengths in the centimetre range.

Sensitivity is an important consideration in EPR. At thermal equilibrium the population difference between the upper and lower levels governs the power absorption by the magnetic system. Applying Boltzmann statistics under the assumption that $h\nu \ll kT$ we find that

$$n \simeq \tfrac{1}{2} N \frac{h\nu}{kT} . \qquad 1.2$$

Here $T > 4$ K, n is the population difference between the levels and N the total population. At room temperature and a frequency of 10 GHz, we find that $n/N \sim 0.1\%$. Equation 1.2 also shows that provided the loss of energy by relaxation and other processes is greater than the absorption, the sensitivity of the EPR experiment varies inversely with the absolute temperature of the sample.

The term 'electron paramagnetic resonance' is generally applied to experiments on paramagnetic atoms or ions (usually transition metals) which are impurities in a diamagnetic host lattice. In these systems the g-value generally deviates from the 'free spin' value of the electron of 2.0023, on account of orbital contributions to the magnetism. The host lattice also interacts with the ion and modifies its magnetic properties, so that an investigation of the latter allows the former to be studied. In contrast to EPR, 'electron spin resonance' is the term generally used to describe similar experiments carried out on systems where there is negligible orbital contribution to the overall magnetism.

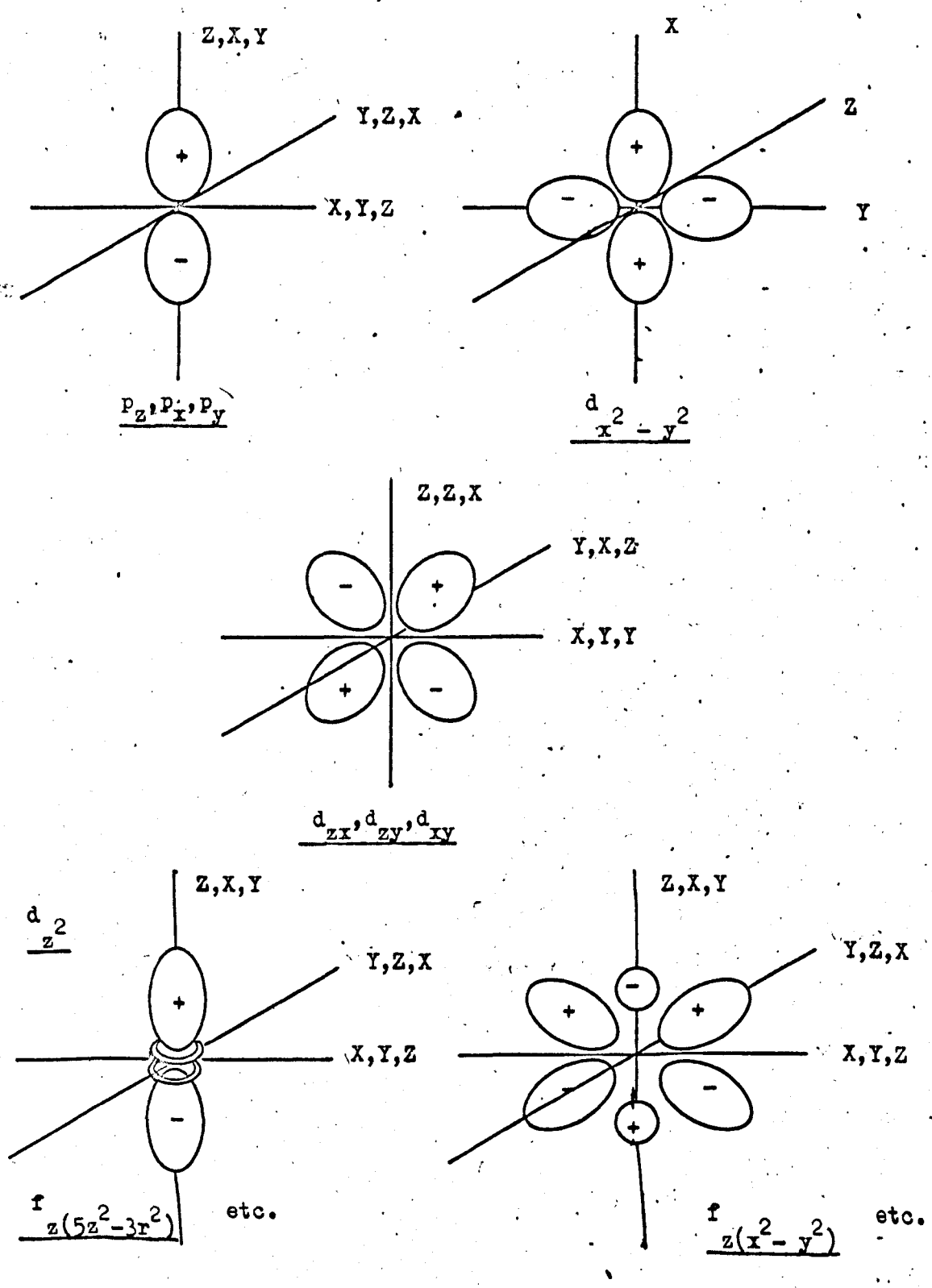

FIGURE 1.2 Schematic forms of the real angular dependence functions for p-, d- and f-orbitals indicating regions of high electron density. After Figgis (1966).

1.2 The structure of free atoms and ions

The classical Hamiltonian for a one electron atom is

$$\mathcal{H} = \frac{1}{2m} p^2 + V(r) \qquad 1.3$$

where V, a function of r alone, is the electrostatic potential, p the momentum of the system and m the rest mass of the electron. In its quantum mechanical form equation 1.3 is

$$\mathcal{H} = -\frac{h^2}{8\pi^2 m}\nabla^2 - Z_{eff}\frac{e^2}{r} \qquad 1.4$$

where Z_{eff} is the effective nuclear charge. Equation 1.4 is the only Hamiltonian for the atom which has explicit closed expressions for the energies and eigenfunctions of the stationary states. Referred to a set of spherical polar coordinates, the wavefunctions which give solutions of the form

$$\mathcal{H}\psi = E\psi \qquad 1.5$$

(E being the energy) are

$$\psi_{n,l,m_l} = R_{n,l}\, Y_l^{m_l} \qquad 1.6$$

where n is the principal quantum number, l the quantum number specifying the orbital angular momentum of the electron, and m_l the quantum number specifying the component of this angular momentum in a unique direction. The conditions on n, l and m_l (all integers) are

$$n \geq 0 \; ; \; l = 0, 1 \ldots\ldots (n-1) \; ; \; -l \leqslant m_l \leqslant l \; . \qquad 1.7$$

The functions $R_{n,l}$ describe the time averaged probability of finding an electron in the specified orbital at a distance r from the nucleus, but for multi-electron atoms they are not particularly useful. The imaginary spherical harmonics $Y_l^{m_l}$ describe the directional properties of the orbitals. From real combinations of these functions electron density diagrams can be constructed, and these give a physical representation of the orbitals. Figure 1.2 illustrates the s, p, d and f orbitals corresponding to states with l = 0, 1, 2 and 3 respectively.

For multi-electron atoms additional terms are included in the Hamiltonian which take account of the mutual electrostatic repulsion between the electrons, and the magnetic coupling which occurs between the spin and orbital momenta. Adding a coulomb repulsion term to equation 1.4 gives

$$\mathcal{H} = \sum_{k=1}^{n} \left[\frac{1}{2m} p_k^2 - \frac{Ze^2}{r_k} \right] + \sum_{k<l}^{n} \frac{e^2}{r_{kl}} , \qquad 1.8$$

and the corresponding wave equation is

$$\left[\sum_{k=1}^{n} \left(\frac{-\hbar^2}{2m} \nabla_k^2 - \frac{Ze^2}{r_k} \right) + \sum_{k<l}^{n} \frac{e^2}{r_{kl}} \right] \psi = E \psi . \qquad 1.9$$

In classical mechanics the two important constants of the motion of an isolated system are the total energy and the total angular momentum. In quantum mechanics, using the Hamiltonian 1.8, it is found that there are two kinds of angular momentum which are constants of the motion. These are the total orbital angular momentum $\underline{L} = \sum_i \underline{l}_i$ and the total spin angular momentum $\underline{S} = \sum_i \underline{s}_i$. Both $\underline{L}$ and $\underline{S}$ commute with the Hamiltonian 1.8, and so $\mathcal{H}$, $\underline{L}^2$, L_z, $\underline{S}^2$ and S_z form a set of five commuting observables and we can classify the states of an atomic system by taking them as simultaneous eigenfunctions of these five observables. Unfortunately the Schroedinger equation 1.9 cannot be solved exactly, so we generally use the reasonably accessible simultaneous eigenfunctions of $\underline{L}^2$, L_z, $\underline{S}^2$, and S_z which are approximate eigenfunctions of $\mathcal{H}$. Exact eigenfunctions of $\mathcal{H}$ are then expansions of the complete set for the other four observables, the justification for this lying in reasonable comparison with experimental data.

From a discussion of the addition of angular momenta it can be shown that there is a complete set of eigenfunctions of $\underline{S}^2$, $\underline{L}^2$, $\underline{J}^2$, and J_z (where $\underline{J} = \underline{L} + \underline{S}$), associated with the complete set of functions of $\underline{L}^2$, L_z, $\underline{S}^2$ and S_z through Wigner's formula (Griffiths 1961, p 19). Any function from either complete set is simultaneously an eigenfunction of

$\underline{S}^2$ and $\underline{L}^2$ and any such complete set is called a Russell-Saunders coupling scheme. The particular values of S and L for any eigenfunction have a marked bearing on its energy, but S_z and L_z do not. Consequently each set of $(2S + 1)(2L + 1)$ individual states (one for each allowed pair $S_z L_z$) characteristic of particular values of L and S are degenerate. They are known as terms, written ^{2S+1}L, where L is S, P, D, F, G, H etc according as L = 0, 1, 2, 3 etc. $(2S + 1)$ is the multiplicity of the term.

The most important term which has yet to be incorporated into the Hamiltonian of a many electron atom is the spin orbit coupling energy. If the electron is moving round the nucleus, an observer on the electron sees the positive nucleus orbiting him with opposite and equal angular momentum. The motion of the nucleus sets up a magnetic field at the electron, so that orientations of the electron magnetic moment relative to this field have different energies. As the spin angular momentum vector is directly opposed to the magnetic moment vector, and lowest energy occurs when the magnetic moment is parallel to $\underline{l}$, there is a positive coupling between the spin and orbital constants of an electron in an atomic system. Summed over n electrons the spin orbit coupling is written as

$$\sum_{k=1}^{n} \xi(r_k)\, \underline{l}_k \cdot \underline{s}_k \qquad 1.10$$

The assumption of LS - coupling means that the coupling is small compared with the energy between terms, and so off diagonal matrix elements of 1.10 between two such terms can be ignored. Then inside each term the Wigner-Eckart Theorem (Abragam and Bleaney 1971, p624) allows 1.10 to be replaced by the single scalar product

$$\lambda\, \underline{L} \cdot \underline{S} \qquad . \qquad 1.11$$

This leads to the fact that the energy of various (J, L, S) multiplets originating from a given (L, S) vary as $\frac{\lambda}{2} J(J + 1)$, a Landé interval rule. Thus the main effect of the spin orbit coupling is to remove the degeneracy of the various levels belonging to a term. The usefulness of the $SLJM_J$

coupling scheme lies in the fact that whereas the spin orbit term commutes with $\underline{J}$, it does not in general commute with $\underline{S}$ or $\underline{L}$.

Before concluding this section two remarks should be made. Firstly most calculations on atomic structure are carried out using the central field approximation - it is supposed that each electron moves in an average, spherically symmetric potential due to nucleus and all other electrons. The eigenfunctions used are of the one electron type (Equation 1.6), being products of an angular part conveniently taken to be one of the hydrogen type functions, with an adjustable radial function. Thus the hydrogen-type electron density diagrams remain extremely useful.

The second point is that the separation between terms in transition metals is generally $\sim 10^4$ cm^{-1} * (L-S coupling $\sim 10^2 - 10^3$ cm^{-1}), and so at room temperature and below only the ground term will be occupied. The ground term may be found using Hunds Rules. It has

i. Maximum total spin

ii. Maximum total orbital momentum consistent with i, taking account of the exclusion principle.

The rules sum up the fact that individual electrons try to share as little space as possible, and if their spins are parallel they must be in different orbitals. The ground state of the free ion is made up of the 2J+1 states characterized by the low energy value of J. States with minimum J have lowest energy in the first half of an unfilled shell, maximum J when the shell is more than half full.

* Energy units of cm^{-1} (inverse centimetres) are defined by $E(cm^{-1}) = \frac{E}{hc}$

1.3 The effect of the crystal environment on the ground state of paramagnetic ions

The general principles of the techniques used to predict the effect of the crystal on entrapped ions are now indicated. Specific examples will be considered later when they become relevant to the discussion of the experimental results.

1.3.1 The crystal field approximation

The energy levels of ions in crystals are usually described in terms of the crystal field approximation. All the ions in the crystal are considered to be point charges, and the resultant electric field modifies the usual orbital motion of the unpaired electrons. The electric field is of order $\frac{e^2}{r}$ i.e. $\sim 6 \times 10^4$ cm^{-1} for r = 0.2 nm. It is usual to subdivide the effects of the crystalline electric field into three categories based upon the strength of its interaction with the electronic motion.

1.3.1.1 Weak Crystal Field

For the rare earth and actinide ions the magnetic f-shell electrons are shielded from the crystalline electric field by s and p electrons in outer shells. The crystal field interaction is then weaker than the spin-orbit coupling and the free ion classification of the atomic states remains valid. The weak crystal field effect is manifest as a small splitting ($\sim$10 - 100 cm^{-1}) of the (2J + 1) degenerate ground state.

1.3.1.2 Intermediate Crystal Field

For iron group ions the crystal field is generally a stronger interaction than the spin-orbit coupling. The (2L + 1) orientations of the orbital angular momentum are separated by $\sim 10^4$ cm^{-1} and only the lowest level is populated. If this is an orbital singlet we have 'spin only' magnetism with a g-value close to 2.0.

1.3.1.3 Strong Crystal Field

The crystal field is considered to be so strong that it breaks down

the coupling between one electron and another. Hunds rules do not apply, and the situation is more accurately described by covalent bonds. Platinum and palladium group ions generally fall into this category.

1.3.2 Qualitative discussion of the Crystal Field

The problems involved in rigorous calculations of the effect of a crystal on the properties of an ion are legion, and approaches can be made on a variety of levels. Indeed, in the simplest cases an appeal to physical intuition yields much information, though of a necessarily qualitative nature. Unfortunately, even rigorous calculations often lead only to estimates of the energies involved.

By using the electron density diagrams of figure 1.2 and allowing negatively charged ions to approach the ion in various symmetrical arrangements it is quite easy to see qualitatively which of a particular set of orbitals will be destabilized most. However, the splitting of the ground term of an ion caused by the crystal field can be found more elegantly using group theory.

1.3.2.1 Group Theory

Group theory can be applied to the splitting of energy levels in a crystalline electric field because the Hamiltonian from which the energy levels are derived is unchanged by a symmetry operation of the electric field. It can be shown that the eigenfunctions of the Hamiltonian are bases for irreducible representations of the symmetry group. The irreducible representations are the simplest ways of describing the operations of the symmetry group mathematically. Further, the matrices which describe the transformations of a set of k eigenfunctions corresponding to a k-fold degenerate eigenvalue are a k-dimensional irreducible representation of the group. Consequently we may use the set of five d-orbitals (or seven f-orbitals) of an atom as a basis for a representation of the point group of the local crystal environment of the atom. If this representation is reducible (say) into a two dimensional and a three dimensional irreducible representation,

we can say that the d-orbitals (in this case) are split by a field of this particular symmetry into a doubly degenerate and a triply degenerate energy level. We can then use the transformation properties of the individual orbitals to say which belong to which level, but we cannot indicate which level is of lowest energy using group theory alone.

The extension of this technique to P, D or F terms is as follows. Assuming that the spin function is entirely independent of the orbital functions, which have the form

$$\psi = R(r)\Theta(\theta)\Phi(\phi) , \qquad 1.12$$

only the function

$$\Theta(\phi) \sim \exp(im\phi) \qquad 1.13$$

is altered by rotations about the axis of quantisation i.e. the axis from which θ is measured, as $R(r)$ is invariant. Because the $\Phi(\phi)$ factor of the wave function for a D term is $\exp(iM\phi)$ in exact analogy to the $\Phi(\phi)$ factor for a single d-electron, its rotation properties, which depend only on M, are exactly analogous to those of the single electron d-orbitals, which depend only on m. Thus the splittings of various sets of one-electron orbitals apply to the splittings of analogous Russell-Saunders terms - an F term splits like f orbitals.

Strictly speaking the above discussion only applies to the region where the splitting between terms is much larger than the splitting caused by the crystal field. However, several theorems exist which allow the intermediate field states to be obtained from a comparison between the weak and infinitely strong field cases. The latter are effectively infinitely larger than the interelectronic repulsion energies.

1.3.3 Point charge calculations of energy levels of magnetic ions in crystalline electric fields

If the crystalline electric field effects originating from some symmetrical arrangement of point charges are considered as a perturbation on the appropriate free ion wave functions and energy levels, we need to

find the perturbing Hamiltonian and its matrix elements. Using perturbation theory the energy levels in the crystal field can be found.

1.3.3.1 Determining the Perturbing Hamiltonian

Using the simple point charge model the perturbing Hamiltonian is essentially the electrostatic potential $V(r,\theta,\phi)$ due to the surrounding point charges at a point (r,θ,ϕ) near the magnetic ion in question (the origin):

$$V(r,\theta,\phi) = \sum_j \frac{q_j}{|(\underline{R}_j - \underline{r})|} \qquad 1.14$$

where q_j is the charge at the j^{th} neighbouring ion, a distance R_j from the origin. If the magnetic ion (charge q_i) is at (r_i,θ_i,ϕ_i) the crystal energy will be

$$W_c = \sum_i q_i V_i = \sum_i \sum_j \frac{q_i q_j}{|(\underline{R}_j - \underline{r}_i)|} \qquad 1.15$$

the summation i being over electrons in unfilled shells.

The potential 1.14 can be calculated either in cartesian coordinates, or in terms of the spherical harmonics Y_n^m, n and m bearing no relation here to the atomic quantum numbers. In cartesian coordinates it is usual to expand the potential up to terms of sixth degree. Generally, however, it is far more convenient to express the potential in spherical or tesseral harmonics as a general formula for its evaluation can easily be derived, and it is far easier to calculate its matrix elements in this form.

In general the potential function must reflect the point symmetry of the lattice site in question, so it must be invariant under the operations of the point group. The less symmetric the site, the more terms occurring in the expansion. The expressions for the potential also depend critically on the axes chosen, being simplest when the axes are the symmetry axes of the point group. However, if the lattice site has a centre of inversion no odd-n terms occur, and if the z axis is m fold, terms in Y_n^m

$^6S,d^5$	$^2D,d^1$,oct.	$^2D,d^1$,tet.	$^3F,d^2$,oct.	$^3F,d^2$,tet.
$^1S,d^0$,	$^5D,d^6$,oct.	$^5D,d^6$,tet.	$^4F,d^3$,tet.	$^4F,d^3$,oct.
d^{10},	$^5D,d^4$,tet.	$^5D,d^4$,oct.	$^4F,d^7$,oct.	$^4F,d^7$,tet.
pct,tet	$^2D,d^9$,tet.	$^2D,d^9$,oct.	$^3F,d^8$,tet.	$^3F,d^8$,oct.

(a)

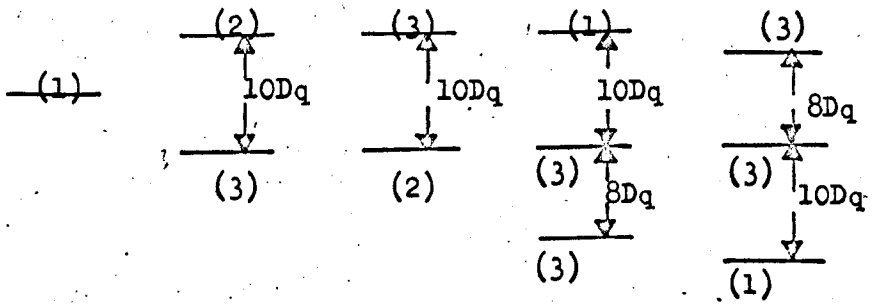

(b)

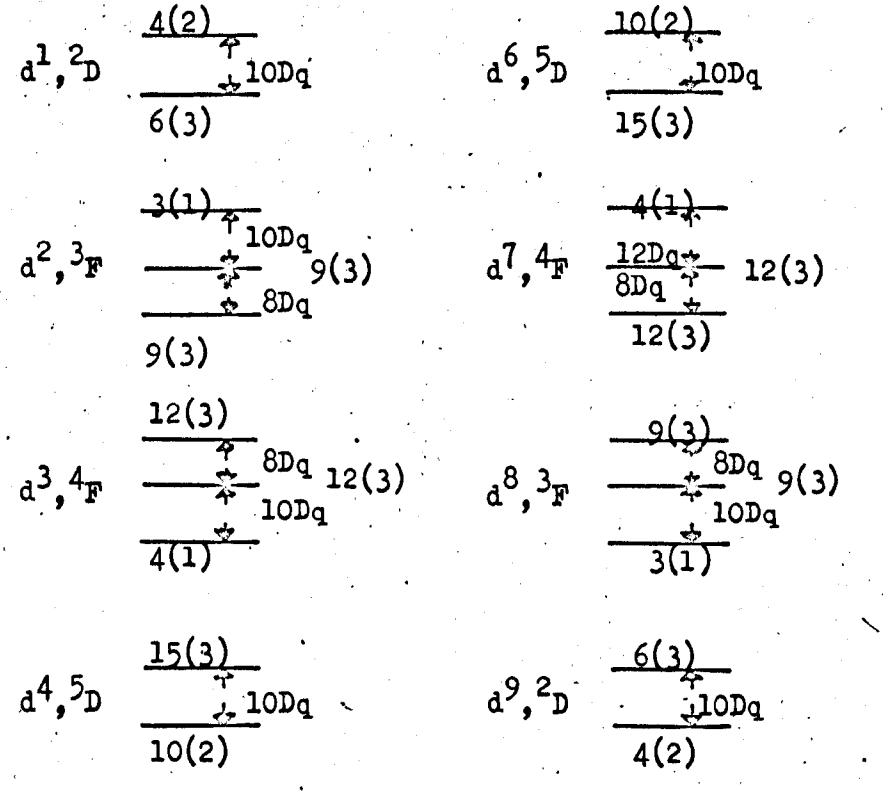

FIGURE 1.3 Splitting pattern of common ground terms in tetrahedral and octahedral symmetry. The numbers given are the total (spin x orbital) degeneracy of the level. Numbers in parenthesis refer to the orbital degeneracy alone.
(a) The configurations which give rise to a given splitting pattern.
(b) The digrams for a given term and configuration for an octahedral crystal field: invert for tetrahedral stereochemistry.

and Y_n^{-m} are found in the expansion.

1.3.3.2 Calculation of the matrix elements of the crystal potential perturbing Hamiltonian

The matrix elements of the perturbing Hamiltonian are calculated between free ion states, and the resultant matrix will then be diagonalized to find the energy levels and eigenfunctions in the crystal field. If the crystal potential is larger than the spin-orbit coupling (3d ions in ionic lattices) the free ion wavefunctions are characterized by $|L,S,L_z,S_z\rangle$, whilst for the 4f group ions the spin-orbit coupling is larger and the wavefunctions are characterized by $|L,S,J,J_z\rangle$.

The most convenient method for evaluating the matrix elements of the crystal potential between wavefunctions specified by a particular value of angular momentum (L or J) involves the use of an angular momentum 'operator equivalent' to the perturbing Hamiltonian which acts only on the angular part of the wavefunction in the coupled system. The equivalent operator is determined from any function of the coordinates x,y,z by replacing them by (say) J_x,J_y and J_z respectively, always allowing for the non-commutation of the latter three. This operator then has the same transformation properties under rotation as the potential, and it is generally written as a sum of terms O_n^m analogous to the Y_n^m. The operators O_n^m are tabulated in most references e.g Hutchings 1964, together with their matrix elements.

Using the appropriate combinations of the O_n^m we can calculate the matrix elements of the full expansion of the perturbing potential, and so determine the energies of the eigenfunctions by diagonalizing the matrix. The coefficients of the O_n^m, the B_n^m, are not easy to calculate, and they are generally the parameters to be determined in the EPR experiment.

In Figure 1.3 the splittings of various terms in octahedral and tetrahedral coordination are shown. It can be seen that one splitting pattern serves for several configurations in different symmetries. Inversion of a pattern accounts for many others.

1.3.4 Degeneracy of levels in the crystal potential

Kramers' theorem (Kramers, 1930) is a very important general theorem dealing with the energy levels of magnetic ions in a crystalline environment. It states that the energy levels of odd-electron ions under an electrostatic interaction of any nature are at least twofold and evenly degenerate. As a consequence of this the matrices of the crystal field Hamiltonian always factorize into at least two similar matrices. When Kramers' theorem does not apply Jahn and Teller (1937) have shown that the surroundings of a magnetic ion will distort and always tend to give non degenerate energy levels. Thus, even-electron ions tend to have singlet energy levels in crystals.

1.4 Calculation of the magnetic properties of the ground state: the Spin Hamiltonian

We now extend the discussion to the determination of the magnetic properties of the ground state of an ion in a crystal, and so demonstrate the plausibility of the spin Hamiltonian. The spin Hamiltonian describes the experimental results of EPR in terms of a ficticious spin and other experimentally determined parameters. Formally the problem consists in finding the eigenvalues of a Hamiltonian operator $\mathcal{H}$ which combines the effects of crystal field, spin-orbit coupling, applied magnetic field and any possible nuclear interactions. Neglecting the latter we write

$$\mathcal{H} = \mathcal{H}_{crys.} + \mathcal{H}_{s.o.} + \mathcal{H}_{magn.} \qquad 1.16$$

This Hamiltonian operates on a set of states $|M_L, M_S\rangle$, and solutions of the equation

$$\mathcal{H}\,|M_L', M_S'\rangle = E|M_L', M_S'\rangle \qquad 1.17$$

are required, where the eigenkets are linear combinations of the original states. This equation is usually solved approximately using perturbation theory: the interactions are taken in descending order of magnitude, each one being regarded as a small perturbation on the preceding term. In the iron group the order is essentially

$$\mathcal{H}_{crys} \gg \mathcal{H}_{s.o.} \gg \mathcal{H}_{magn} \quad ; \qquad 1.18$$

for the rare earth (4f and 5f) groups this is altered to

$$\mathcal{H}_{s.o.} \gg \mathcal{H}_{crys} \gg \mathcal{H}_{magn}. \qquad 1.19$$

The form of $\mathcal{H}_{crys}$ has already been illustrated, while $\mathcal{H}_{s.o.}$ takes the form of equation 1.11 with $\underline{L}$ and $\underline{S}$ being regarded as angular momentum operators. To obtain the operator describing the magnetic Zeeman interaction with the external field B we consider the orbital and spin contributions separately, having energies $\mu_L . \underline{B} = \mu_B \underline{L} . \underline{B}$ and $\mu_S . \underline{H} = 2\mu_B \underline{S} . \underline{B}$:

$$\mathcal{H}_{magn} = \mu_B \underline{B}(\underline{L} + 2\underline{S}) \qquad 1.20$$

1.4.1 Magnetic properties in a weak crystal field

The magnetic properties of the trivalent rare earth ions are determined essentially by the number of electrons in the 4f shell. In the free ions the coupling between these electrons is almost perfect L-S coupling, and the ground state is predicted by Hund's Rules. However, the spin-orbit coupling energy is not negligible compared with the coulomb energy. Consequently splittings occur within the ground multiplet which do not obey the Lande interval rule, and corrections must be applied in deriving the value of the spin-orbit coupling parameter.

In a crystalline environment the magnetic electrons of the rare earth ions are only slightly affected because of the shielding effect of the 5s and 5p electrons. Interactions with the ligand ions have energies of approximately 10 - 100 cm^{-1}, which are small compared with the spin-orbit coupling. We can therefore work in terms of J with possible corrections for coupling to states of different J. In an external field $\underline{B}$ the diagonal electronic Zeeman interaction takes the appropriate form of equation 1.20,

$$\mathcal{H} = g_J \mu_B (\underline{B} . \underline{J}) \quad . \qquad 1.21$$

The crystal field is described by the equivalent operators O_n^m and it reflects the symmetry of the lattice site. Terms with m = 0 contain only J_z; they are diagonal for all M_J, and the same for $\pm M_J$. A crystal potential

containing only such terms will produce a series of doublets $|\mp M_J\rangle$, with a singlet $|0\rangle$ if J is integral. When m and n are both non-zero the states $|J, M_J+ m\rangle$ and $|J, M_J- m\rangle$ are mixed with $|J, M_J\rangle$. If second order matrix elements must be considered they will be between states of different J. For ions with an odd number of electrons, therefore, the crystal field lifts the degeneracy of the $|+M_J\rangle$ .....$|-M_J\rangle$ states completely, except for the necessary degeneracy imposed by Kramers' Theorem, and the levels consist of $(J + \frac{1}{2})$ doublets. Generally the separation between doublets is ~10 - 100 cm^{-1}, so that only transitions within a doublet are observed with microwave radiation of energy~1 cm^{-1}.

To find the resonance condition the Zeeman interaction for each doublet is calculated using equation 1.21. In the case of axial symmetry J_x and J_y have equal matrix elements, which are different from J_z. Consequently the electronic Zeeman term within each doublet is described by a spin Hamiltonian with an effective spin $S = \frac{1}{2}$ and a cylindrically symmetric g-factor:

$$\mathcal{H} = g_{\parallel}\mu_B B_z S_z + g_{\perp}\mu_B(B_x S_x + B_y S_y) \qquad 1.22$$

with

$$g_{\parallel} = 2g_J\langle +M_J| J_z| +M_J\rangle$$
$$\text{and} \quad g_{\perp} = g_J\langle +M_J| J_+| -M_J\rangle \qquad 1.23$$

for $|\mp M_J\rangle$.

1.4.2 Magnetic properties in an intermediate crystal field

The $3d^n$ transition metal ions are frequently observed in ligand fields of intermediate strength. The electrostatic approach is used to determine their ground state magnetic properties although it is not readily applicable because the charge distributions and relative positions of the ions are not accurately known. In addition the electrostatic energy change for the magnetic electrons is not a small perturbation, and there is overlap between electron wavefunctions on ligand and ion. A rigorous calculation would treat the complex of ion and ligands as a whole, but the spin-operator

form of the ligand field interaction

$$\mathcal{H}_{\text{ligand}} = \sum_{m=2,4} \sum_{n=-m}^{m} B_m^n O_m^n \qquad 1.24$$

remains useful because it faithfully reflects symmetry considerations. The B_m^n are determined by experiment, and the O_m^n are written in terms of L rather than J because the spin-orbit coupling may be regarded realistically as a perturbation on the crystal field. Quite often, however, the splitting of an F term of these $3d^n$ ions is larger than the separation between the ground F term and the excited P term. When this is the case the strong field approach is needed.

Where L-S coupling remains valid and the cubic field results in the ground orbital state being a singlet, general formulae for the magnetic properties of the ions may be deduced. The effective spin $\hat{S}$ in the spin Hamiltonian is then generally the same as the true spin S. When the ground orbital state is not a singlet the situation is more complex.

1.4.2.1 The spin Hamiltonian for an orbital singlet state

We now consider the consequences of applying perturbations to an orbital singlet state in the form of the spin-orbit coupling and Zeeman interactions:

$$\mathcal{H}_p = \lambda(\underline{L}.\ \underline{S}) + \mu_B(\underline{L} + 2\underline{S}).\ \underline{B}\ . \qquad 1.25$$

For an orbital singlet $|0\rangle$ all diagonal components of the orbital angular momentum are zero,

$$\langle 0|\underline{L}|0\rangle = 0 \qquad 1.26$$

and so the spin-orbit coupling has no first order effect on $|0\rangle$. We expect a g-value near to 2.00, with the energy of $|0\rangle$ being shifted by

$$\langle 0\ |\lambda\underline{L}.\ \underline{S} + \mu_B(\underline{L} + 2\underline{S}).\ \underline{B}\ |\ 0\rangle = 2\mu_B\underline{S}.\ \underline{B}\ . \qquad 1.27$$

However, the spin-orbit coupling can have an effect to second order in perturbation theory which can be as large as the first order Zeeman interaction. Second order perturbation theory connects $|0\rangle$ to higher lying

non-degenerate states $|n\rangle$ with energy E_n ($n = 1.....n$), and it shifts the energy by

$$-\sum_{n\neq 0}\frac{\langle 0|\lambda\underline{L}\cdot\underline{S}+\mu_B(\underline{L}+2\underline{S})\cdot\underline{B}|n\rangle\langle n|\lambda\underline{L}\cdot\underline{S}+\mu_B(\underline{L}+2\underline{S})\cdot\underline{B}|0\rangle}{E_n-E_o} \quad 1.28$$

Ignoring terms in the square of the magnetic field, the important terms in the numerator of 1.28 are

$$-\sum_{i,j=x,y,z}\sum_{n\neq 0}\lambda^2\langle 0|L_i|n\rangle\langle n|L_j|0\rangle\ S_iS_j \quad 1.29$$

and

$$-2\sum_{i,j=x,y,z}\sum_{n\neq 0}\lambda\mu_B\langle 0|L_i|n\rangle\langle n|L_j|0\rangle\ S_i\cdot B_j \quad . \quad 1.30$$

Since $\underline{S}$ is a constant for orbital states all other terms in 1.28 are zero, and $\underline{S}$ can be taken out of the matrix elements in 1.29 and 1.30. Adding the energies 1.27 and 1.28 we obtain for the energy of the ground state, correct to second order in perturbation theory,

$$\mathcal{H}_S = 2\mu_B\underline{B}\cdot\underline{S} - \sum_{i,j=x,y,z}\Lambda_{ij}\left[\lambda 2\mu_B\cdot B_iS_j+\lambda^2S_iS_j\right] \quad 1.31$$

where the tensor

$$\Lambda_{ij} = \sum_{n\neq 0}\frac{\langle 0|L_i|n\rangle\langle n|L_j|0\rangle}{E_n-E_o} \quad 1.32$$

contains all the information about interactions with excited orbital states. Rearranging 1.31 to bring together terms linear in $\underline{B}$ gives

$$\mathcal{H}_S = \sum_{i,j=x,y,z}\left[2(\delta_{ij}-\Lambda_{ij})\mu_BB_iS_j-\lambda^2\Lambda_{ij}S_iS_j\right] \quad 1.33$$

where δ_{ij} is the Kroneker delta. In tensor notation equation 1.33 becomes

$$\mathcal{H}_S = \mu_B\underline{B}\cdot\underline{g}\cdot\underline{S}+\underline{S}\cdot\underline{D}\cdot\underline{S} \quad 1.34$$

where g and D are real symmetric tensors, diagonal if expressed in terms of the principal axes of the system i.e.

$$\begin{aligned} g_{ii} &= 2(1-\lambda\Lambda_{ii}) \\ D_{ii} &= -\lambda^2\Lambda_{ii} \end{aligned} \quad 1.35$$

Equation 1.34 is usually called the spin Hamiltonian of the ground orbital state. The parameters $\underline{g}$ and $\underline{D}$ are experimentally determined so as to give the best fit to the values of the magnetic field B at which transitions occur.

Equation 1.34 can be written in different ways depending on the symmetry of the ligands around the magnetic ion. In a cubic environment the term $\underline{S}.\underline{D}.\underline{S}$ is a constant and the spin Hamiltonian is simply

$$\mathcal{H}_S = g\mu_B \underline{B}.\underline{S} \quad . \qquad 1.36$$

In tetragonal or trigonal symmetry where $\Lambda_{zz} = \Lambda_{\parallel}$ and $\Lambda_{xx} = \Lambda_{yy} = \Lambda_{\perp}$ it is usual to write

$$\mathcal{H}_S = g_{\parallel}\mu_B S_z B_z + g_{\perp}\mu_B(B_x S_x + B_y S_y) - \lambda^2(\Lambda_{\parallel} S_z^2 + \Lambda_{\perp}(S_x^2 + S_y^2) \quad . \qquad 1.37$$

The last term of 1.37 can be rearranged to give

$$D(S_z^2 - \tfrac{1}{3}S(S+1)) \equiv \tfrac{1}{3}B_2^0 O_2^0 \quad . \qquad 1.38$$

For ions with orthorhombic symmetry $\Lambda_x \neq \Lambda_y \neq \Lambda_z$ and the most appropriate form of the spin Hamiltonian is

$$\mathcal{H}_S = \mu_B(g_z B_z S_z + g_y B_y S_y + g_x B_x S_x) + D(S_z^2 - \tfrac{1}{3}S(S+1)) + E(S_x^2 - S_y^2) \quad . \qquad 1.39$$

The term $(S_x^2 - S_y^2)$ is equivalent to the operator O_2^2 .

The general derivation of the spin Hamiltonian for intermediate fields is modified in the presence of bonding effects (see Owen and Thornley 1966) and the spin-spin interaction (Abragam and Bleaney 1970).

Finally it should be mentioned that the spin Hamiltonian for S-state ions contains the terms of equation 1.24 written in terms of S in weak, intermediate and strong crystal fields. The splittings introduced between the spin states are small, being brought about by high order interactions with the crystal field. This will be considered explicitly in a later chapter dealing with the EPR spectra of Gd^{3+} in calcium oxide.

1.5 Additional terms in the spin Hamiltonian: Hyperfine Structure

Hyperfine structure was one of the more important discoveries

made in the early EPR experiments on diamagnetic single crystals containing nominally isolated paramagnetic ions. Hyperfine structure has both magnetic and electrostatic origins.

1.5.1 Magnetic Hyperfine Interaction

This is the most important interaction arising from the coupling between the nuclear magnetic moment and the magnetic field at the nucleus due to the electron cloud. Alternatively it may be regarded in terms of the interaction between the electron magnetic moment and the magnetic field set up by the nuclear magnetic moment. The magnetic moment of the electrons is due partly to their orbital motion, and partly to their spin.

A coupling between the nuclear spin and the orbital motion of the electron arises because the magnetic moment of the nucleus, regarded as a point dipole, produces a magnetic vector potential which interacts with the electronic current density. There is also an interaction between the nuclear magnetic moment and the magnetization associated with the electron spin. This energy is

$$W = -\underline{\mu}_I \underline{B}_e \qquad 1.40$$

where $\underline{B}_e$ is the magnetic field at the nucleus due to the electron spin. B_e has contributions from both 'outside' and 'inside' the nucleus. The former gives a simple dipolar contribution derivable from classical E-M theory, which vanishes in an electron spin density of spherical symmetry. This term is also zero for a single s-electron, although in this case a contribution from the electron magnetization 'inside' the nucleus must be considered. This electron-nuclear spin coupling is usually referred to as the 'Fermi-Segre' or 'contact hyperfine'interaction.

Each of these three interactions can be represented quantum mechanically by carrying out classical calculations and then using the method of equivalent operators developed by Abragam and Pryce (1951) which is discussed in section 1.3.3.2. The equations are slightly different for atoms where $\underline{L}$ and $\underline{S}$ are coupled to form a resultant $\underline{J}$, as in the 4f group.

In this case the sum of orbital and spin-dipolar contributions reduces to the simple form

$$\mathcal{H} = A_J (\underline{I}.\underline{J}) , \qquad 1.41$$

whilst the contact term can be written

$$\mathcal{H} = A_S'(\underline{I}.\underline{J}) . \qquad 1.42$$

For an atom with LS coupling the contact term is

$$\mathcal{H} = A_S (\underline{I}.\underline{S}) \qquad 1.43$$

but there is no simple form of the orbital and spin-dipolar terms.

In more accurate work account has to be taken of both the precession of the closed electron shells in the field of the nucleus which produces a diamagnetic shielding effect, and the relativistic increase in the mass of the electron which effectively reduces its magnetic moment. Additionally, for heavier nuclei it may be necessary to correct for the finite extent of the nuclear magnetization. The different distributions of nuclear magnetization for two isotopes of the same element may produce a 'hyperfine anomaly' where the ratio of the contact hyperfine interactions for the two isotopes is not in the ratio of their magnetic moments.

Calculations of the orbital and spin-dipolar contributions to the magnetic hyperfine interaction involve the parameters $\langle r_L^{-3} \rangle$ and $\langle r_S^{-3} \rangle$. These are values of the $\frac{1}{r^3}$ integrals found in the equivalent classical energy expressions, averaged over the radial functions of all the electrons in the atom. These parameters would be equal in a hydrogen type atom, but in a many electron atom the resultant hyperfine structure is the vector sum of contributions from different electrons. A closed shell has no hyperfine structure, but the electrostatic repulsion between electrons when an open shell is present gives rise to an exchange interaction which causes all those spins in closed shells parallel to the spins in the open shells to have slightly different energies from those electrons in the closed shells with antiparallel spins. Differences in their radial wave functions result in a change in the values of $\langle r^{-3} \rangle$. This mechanism applied particularly to

s-electrons allows explanation of the anomalously large hyperfine interactions of atoms with half filled shells (e.g. Mn^{2+}) where no hyperfine splitting is expected since L = 0. The effect of the exchange interactions on the s-electrons in the closed shells cause a small imbalance in the spin density at the nucleus which can give a large contact contribution to the hyperfine structure. This is usually referred to as 'exchange' or 'core polarization'. An additional contribution may come from the 'configuration interaction' which arises through a ground configuration becoming slightly contaminated with excited configurations containing unpaired s-electrons. The resultant contact interaction can cause appreciable nuclear coupling in the ground term without altering its other properties noticeably.

The magnetic hyperfine interaction splits the electronic energy levels and it is incorporated into the spin Hamiltonian by extending the operator for the free atom. It is written as

$$\mathcal{H} = (\underline{S}.\ \underline{A}.\ \underline{I}) \qquad 1.44$$

where $\underline{I}$ is the nuclear spin operator. $\underline{A}$ is a real, usually symmetric, tensor for which the cross terms vanish when referred to its principal axes, leaving

$$\mathcal{H} = A_x S_x I_x + A_y S_y I_y + A_z S_z I_z \qquad 1.45$$

to be added to the spin Hamiltonian.

1.5.2 The Electrostatic Hyperfine Interaction

The energy of the electrostatic interaction between the nucleus and an electron takes the form

$$W_E = \frac{1}{4\pi\epsilon_0}\iint \frac{\rho_e \rho_n}{|r_n - r_e|}\, d\tau_n d\tau_e \ . \qquad 1.46$$

This expression can be expanded in terms of products of spherical harmonics referred to the nuclear and electronic coordinates, in a similar way to that outlined for the crystal field potential. The first term in such an expansion represents the coulomb interaction between nucleus and electrons, which must strictly be modified to take account of the finite electronic charge density inside the nucleus. The second term has no effect, and

the third term in the spherical harmonic expansion is the quadrupole term (Y_m^n with m=2) which arises from asymmetry in the charge distributions. The nuclear charge distribution can be asymmetric for $I \geqslant 1$. Asymmetry of the electronic charge distribution arises through interaction with the crystal field. The spherical harmonics are regarded as tensor operators, and the ones involving the nuclear coordinates go over into a form involving the nuclear spin operator I, and its components. The'electronic harmonics' are replaced by operator equivalents involving the orbital angular momentum of each electron, which are then summed over all the electrons. (These replacements are allowed on account of the Wigner-Eckart Theorem, and are analogous to the corresponding operations in the crystal field calculation). For each state of an electronic doublet the interaction can be represented in terms of the nuclear operators only, with suitable multiplying factors to take account of the orbital parts. In cartesian coordinates these terms can be written in the form

$$\mathcal{H} = \underline{I} \cdot \underline{P} \cdot \underline{I} \qquad 1.47$$

appropriate to a spin Hamiltonian with $S = \frac{1}{2}$. We expect $\underline{P}$ to be a symmetric tensor which can be reduced by choosing suitable axes to the form

$$P_x I_x^2 + P_y I_y^2 + P_z I_z^2 \quad . \qquad 1.48$$

In axial symmetry this becomes

$$P_{||} \left\{ I_z^2 - \tfrac{1}{3} I(I+1) \right\} \qquad 1.49$$

where in the most common nomenclature

$$P_{||} = \frac{3eQ}{4I(2I-1)} \cdot \frac{\partial^2 V}{\partial z^2} = \frac{3}{2} P_z \quad . \qquad 1.50$$

In equation 1.50 e is the electronic charge, and the differential is the electric field gradient at the nucleus due to both the ion and the crystal field potential. Q is a constant used in the introduction of the nuclear operator equivalents.

Additional positive or negative contributions to the electronic hyperfine structure can arise when closed shell electrons are distorted by

the electric field gradients to which they are subjected. This is the Sternheimer Effect. In addition half filled shells with spherical symmetry can also contribute a small quadrupole interaction through distortions in their radial functions due to relativistic effects.

1.5.3 The Nuclear Zeeman Interactions

The term

$$-\mu_N \underline{B}\cdot\underline{g}_N\cdot\underline{I} \qquad 1.51$$

which represents the direct interaction of the nuclear magnetic moment with the external field can also be added to the spin Hamiltonian. Due to shielding effects g_N is not a scalar quantity equal to the ordinary nuclear g-factor.

1.5.4 The General Spin Hamiltonian

The spin Hamiltonian which can generally be used to describe the results of EPR experiments is, in the notation of the preceeding sections,

$$\mathcal{H} = \mu_B \underline{B}\cdot\underline{g}\cdot\underline{S} + \sum_m \sum_{n=-m}^{m} B_m^n O_m^n + \underline{S}\cdot\underline{A}\cdot\underline{I} + \underline{I}\cdot\underline{P}\cdot\underline{I} - \mu_N \underline{B}\cdot\underline{g}_N\cdot\underline{I} \qquad 1.52$$

where the O_m^n are written in terms of the spin S. The terms required in any particular situation must be gleaned from experimental evidence, with the variation of the spectrum as the magnetic field direction is changed with respect to the crystal axes being important. The number of absorption lines occurring, both strong (allowed transitions) and weak (forbidden transitions), is helpful in determining the values of the electron and nuclear spins.

1.6 The observation of resonance

So far we have implied that when a transition occurs the 'spin system' absorbs energy at a precise value of the magnetic field. In fact, for microwave energy to be absorbed there must be a finite transition probability, and the absorption actually occurs over a finite range of magnetic field centred on the resonance value.

1.6.1 The transition probability

When the energy difference between any two levels of the spin system in the applied magnetic field equals the energy of the incident microwave quantum, a transition can in principle occur. The only constraint on the occurrence of a transition is the transition probability. This important quantity may be estimated using time dependent perturbation theory. For a magnetic ion experiencing an additional perturbation in the form of an oscillating microwave magnetic field

$$B = B^1 \sin\omega t \qquad 1.53$$

the transition probability is

$$W_{12} = \frac{\gamma^2}{h^2} g(\nu)\beta^2 \left| \langle 1| \underline{B}^1.g.\underline{S} |2\rangle \right|^2 \qquad 1.54$$

where $\langle 1|$ and $|2\rangle$ are the spin levels between which a transition is anticipated. The function $g(\nu)$ is a normalized lineshape function. For EPR to be observed B^1 must be perpendicular to the static field B, and transitions in which the electronic spin quantum number changes by ± 1 are most strongly allowed i.e. the selection rule for EPR is $\Delta M_s = \pm 1$. If hyperfine levels are involved the nuclear quantum number does not change for an allowed transition. However, the study of so-called forbidden transitions (any transitions outside the realm of the allowed) can often be rewarding.

1.6.2 Absorption lineshape

The phenomenon of resonance is well known in physics. In the case of electron paramagnetic resonance a classical description of the resonance is often useful, and by analogy with similar effects in classical physics we expect the energy absorption curve to have width and shape characteristic of the system. Occasionally magnetic resonance absorption curves are Lorentzian in shape; less frequently they are Gaussian. In general the observed lineshapes lie somewhere between these two extremes. Very broad lines make accurate measurements of spin

Hamiltonian parameters rather difficult; they may even cause a resonance to be obscured completely. It is if some interest therefore to outline the mechanisms by which lines are broadened.

1.6.2.1 Inhomogeneous line broadening

An absorption line is said to be inhomogeneously broadened if it is really an envelope of a number of narrower but unresolved lines. A simple example occurs if the applied magnetic field has poor uniformity, as sharp resonances can occur in different parts of a crystal at apparently different fields. The width of the line is then determined by the inhomogeneity in the magnetic field. However, inhomogeneous broadening mainly results from:

(i) the dipolar interaction between unlike magnetic ions which causes each ion to 'see' the true field plus contributions from different magnetic ions in the crystal. A random distribution of such ions results theoretically in a Gaussian lineshape.

(ii) unresolved hyperfine structure. Crystals often contain non-magnetic ions with nuclear moments which can produce small splittings in the electronic energy levels. Each absorption is then the sum of a large number of unresolved hyperfine absorptions.

(iii) inhomogeneity in the crystal lattice. Any irregularity in the crystal lattice will alter the crystal field acting on each magnetic ion resulting in a spread of the energy levels.

1.6.2.2 Homogeneous line broadening

Homogeneous line broadening arises from the finite lifetime of the upper state involved in the resonance. It is often called 'lifetime broadening' because it arises from the Uncertainty Principle

which relates the width ΔE of an energy level to the lifetime Δt of the corresponding state by the relation

$$\Delta E . \Delta t \sim \hbar \qquad 1.55$$

or

$$\Delta \nu \sim \frac{1}{2\pi \Delta t} . \qquad 1.56$$

If we relate Δt to some relaxation time of the system i.e. $\Delta t \simeq \frac{1}{p}$ where p is the probability per unit time of a relaxation process being effective, equation 1.56 implies that any relaxation time shorter than $\sim 10^{-8}$ seconds will dominate the linewidth, and possibly make the resonance undetectable.

Any interaction between the magnetic ion and its surroundings can broaden the line if it results in energy being transferred from the ion following excitation by the microwave field. Spontaneous emission is negligible at microwave frequencies, and the two common sources of homogeneous broadening are spin-lattice relaxation (characterized by a relaxation time T_1) and the spin-spin interaction between similar magnetic ions (characterized by T_2). Both are interesting properties of the system which can be measured: they are described in the two following sections.

1.6.3 Spin-lattice relaxation

Spin-lattice relaxation is a two step process involving the transfer of energy from the spin system to the lattice vibrations and thence to the thermal bath with which the lattice is in contact. If the coupling of the lattice to the bath is very inefficient (i.e. has a long relaxation time) any attempt to measure relaxation times will result only in a measurement of the characteristic time for lattice/bath energy transfer. Phonons can get 'hot' because of this and they can 'cool' again by mechanisms which depend on the crystal size and the concentration of magnetic ions. The existence of this 'phonon bottleneck' can be ascertained experimentally.

The coupling between spin system and lattice occurs mainly because of the interaction of the magnetic ion with the crystal field: it occurs through the crystalline electric field being modulated by the lattice vibrations. Since the crystal field interacts directly only with the orbital motion of the magnetic electrons, the strongest spin-lattice interaction will occur for ions whose ground states contain appreciable orbital contributions. Three mechanisms have been postulated for spin lattice relaxation:

(i) Direct Process. Relaxation occurs by the emission of a phonon of energy equal to the energy difference between the two spin levels. The relaxation time of this process is calculated to vary as the inverse of the absolute temperature of the lattice.

(ii) Raman Process. This is a two phonon process in which relaxation occurs by the absorption of a phonon by the excited spins promoting them to virtual levels, followed by the emission of a phonon of higher energy equal to the sum of the energy of the first phonon and the incident microwave quantum. The requirement of two phonons implies that this process will tend to occur at higher temperatures. Indeed, it occurs generally above $4^{\circ}K$, and for a Kramers ion T_1 varies as T^{-7}.

(iii) Orbach Process. This is rarer than the Raman Process, but it is similar in that it involves the absorption and then emission of phonons, but this time promotion is to an actual ionic energy level. T_1 varies here exponentially. This is a process involving two resonant direct process transitions, in contrast to the Raman Process which involves non-resonant scattering.

1.6.4 Spin-spin interaction

When nearby paramagnetic ions are identical the adjacent spins can increase the efficiency of relaxation besides contributing to the inhomogeneous width of the absorption curve. The oscillating magnetic fields produced by the spins precessing at the same rate allows the exchange of quanta. Additional broadening results, and the lifetimes of the quantum states of the individual ions are shortened.

The spin-spin interaction is also important in cross - relaxation processes when absorption lines overlap. Energy can be transferred quickly from one 'hot' spin system to another 'cold' system rather than to the lattice, and false relaxation times are obtained.

The spin-spin interaction is not very strong in magnetically dilute systems.

1.6.5 Power saturation

If we apply more microwave power to the spin system than can be removed by relaxation processes the populations in the Zeeman levels will become equal, and the intensity of the resonance absorption will decrease to zero. This property can be utilized to measure the spin - lattice relaxation times of the system either by increasing the incident power slowly to saturation and monitoring the decrease in power absorbed, or by quickly applying a very strong pulse of microwave power to the spin system and then watching its recovery to equilibrium using a small monitoring signal. This latter technique is known as pulse saturation recovery. Helium temperatures are generally needed for both these techniques.

Broadening is only a useful technique for measuring relaxation times of between 10^{-8} and 10^{-10} seconds. The high speed limit is determined by linewidth considerations, and the low speed limit by the inhomogeneous width of the resonance lines.

1.7 ENDOR

The term ENDOR is an acronym for Electron-Nuclear DOuble Resonance, and it describes a technique whereby direct nuclear transitions are observed by using the high sensitivity detection of EPR. An EPR hyperfine transition is partially saturated and an RF magnetic field is applied to the sample at righ angles to both the microwave and static magnetic fields. When the energy of the RF quantum equals the difference in energy between one of the levels involved in the EPR transition and another level whose M_I value is ± 1 relative to the first, a nuclear transition occurs. This transition is detected as a change in the intensity of the EPR signal, brought about by the change in population of the nuclear levels. In general, if M and m are electronic and nuclear quantum numbers respectively, the four ENDOR transitions $|M,m\rangle \longleftrightarrow |M, m \pm 1\rangle$ and $|M-1,m\rangle \longleftrightarrow |M-1,m \pm 1\rangle$ can usually be detected whilst saturating the $|M,m\rangle \longleftrightarrow |M-1,m\rangle$ electronic hyperfine line, except when $m = \pm I$, and then only two transitions can be observed.

Apart from the increased accuracy with which the hyperfine parameters are determined using ENDOR, their relative signs and the nuclear g-factor can also be found. ENDOR is invaluable in studying transferred hyperfine structure, caused by the interaction of electrons on one ion with the nucleus of another. This gives information on both the spatial extent of the electron wavefunction and the immediate environment of the ion.

A detailed theoretical and experimental treatment of ENDOR is given in Abragam and Bleaney,1970.

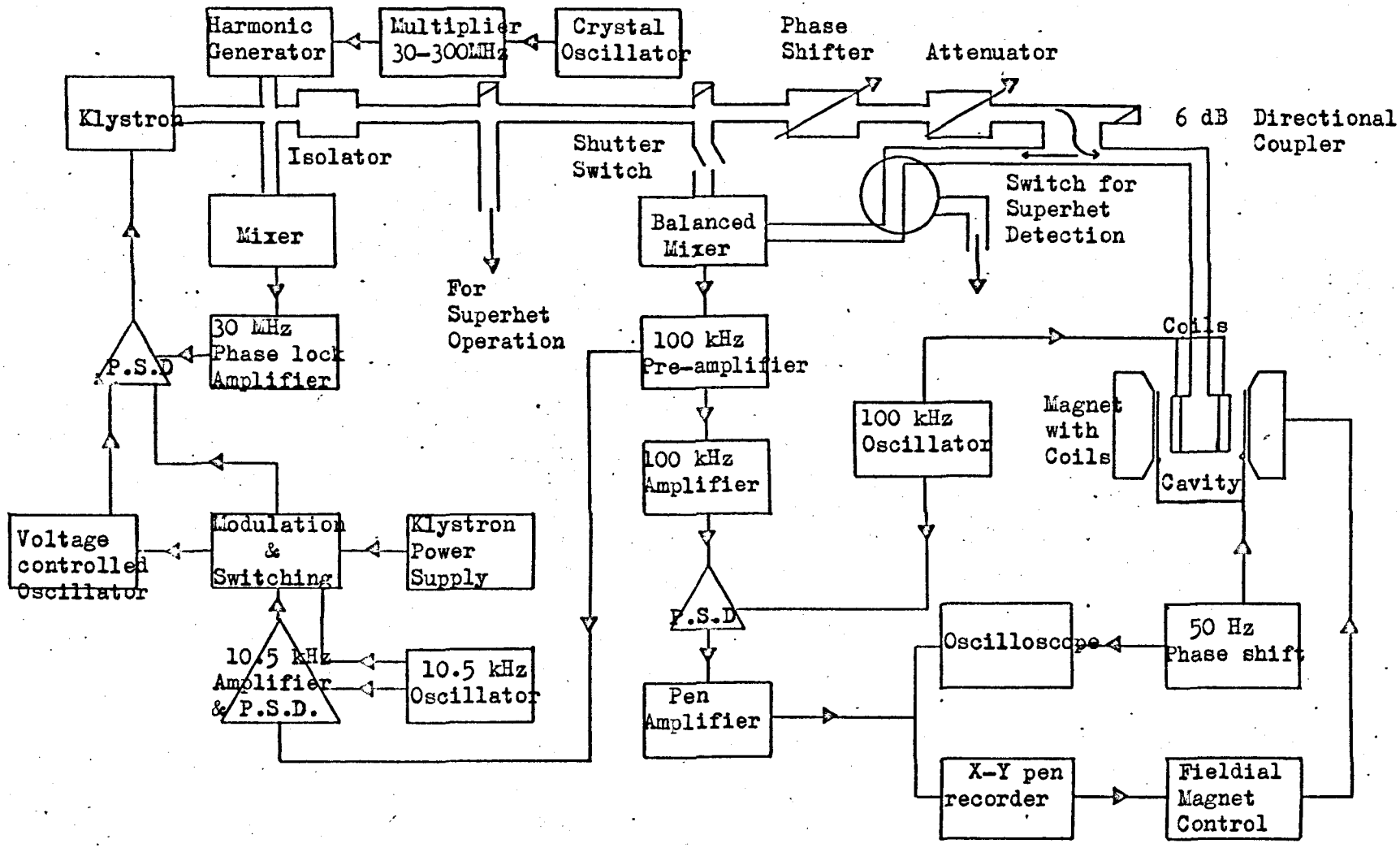

FIGURE 2.1 Decca X2 Spectrometer using simple detection.

CHAPTER II

EXPERIMENTAL TECHNIQUES

2.1 Introduction

Experiments at X-band frequencies in the temperature range between room temperature and 77 K were performed on a Decca X2 spectrometer, whilst for studies at 4 K a Varian superheterodyne spectrometer was used. A Varian 35 GHz microwave bridge was used for experiments at Q-band.

Both spectrometer systems utilize 9 inch Varian rotatable magnets capable of fields up to 0.9 T. The magnetic field for the Decca spectrometer is controlled by a Mk.II Fieldial unit, whilst the Varian spectrometer magnet, equipped with removeable shims which increase the field capability to 1.6 T for Q-band work, is controlled by a Mk.I Fieldial unit.

2.2 Decca Spectrometer

The Decca X2 spectrometer operates at a fixed frequency of 9.270 GHz with a tuneable rectangular TE_{102} cavity. The spectrometer frequency is maintained constant within ± 1 MHz by a phase-lock system which compares the 30 MHz beat frequency between the signal klystron and an optimized harmonic of a highly stabilized crystal oscillator with the 30 MHz output of a voltage controlled oscillator. The d.c. output of the phase-lock system is applied to the klystron reflector.

Figure 2.1 is a block diagram of the components of the spectrometer. Bucking power at the balanced mixer detector is obtained using a cross-guide coupler. A 6 dB directional coupler is used to apply power to the cavity and to direct reflected power to the detector.

Two cavity-lock systems are available to maintain sensitivity as the cavity frequency drifts, both using a 10.5 KHz voltage applied to the reflector of the klystron. This modulates the klystron frequency

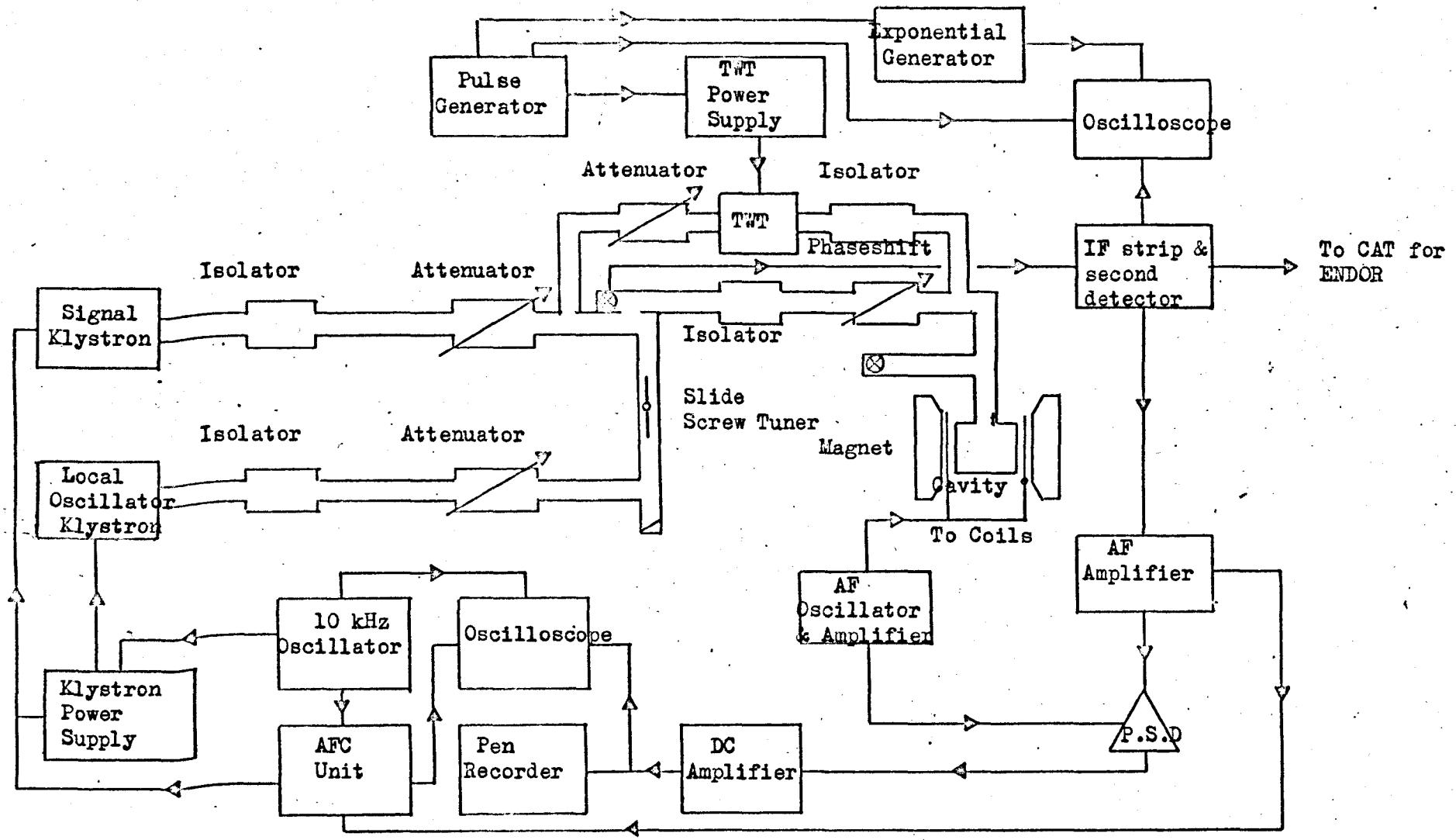

FIGURE 2.2 The Varian X-band Spectrometer with added equipment for measuring spin lattice relaxation times.

and a 10.5 KHz signal is obtained from the detector, the phase of which varies with cavity drift. Phase sensitive detection produces a d.c. output proportional to cavity drift which can be applied direct to the klystron, or to the voltage controlled oscillator of the phase-lock system.

The derivative of the resonance absorption is detected by using 100 KHz magnetic field modulation, tuned amplification and phase-sensitive detection.

2.3 The Varian Spectrometer

2.3.1 X-band spectrometer

A block diagram of the Varian spectrometer is shown in figure 2.2, together with the modifications used to measure spin-lattice relaxation times.

This spectrometer is much more flexible than the Decca system since it operates over the frequency range 9.1 to 10 GHz. The signal klystron is tuned to the cavity by obtaining the cavity dip in the centre of the mode, and the local oscillator is tuned to be 30 MHz away by obtaining the dip in the centre of the IF bandpass. Only the signal klystron is locked to the cavity by the automatic frequency control system (AFC) so the IF receiver has a bandpass of 1.5 ± 0.5 MHz to accommodate drift. Magnetic field modulation at audio frequencies or 100 KHz enables the first derivative of the absorption curve to be obtained by phase sensitive detection.

Measurements near to 4 K were made using resonant cavities which were immersed in liquid helium in an Oxford Instruments MD4 cryostat. For temperatures of 77 K and above a commercial Varian cavity is available.

2.3.2 Q-band Spectrometer

The microwave bridge of the 35 GHz spectrometer is illustrated in figure 2.3 - the same electronic units are used as in the X-band spectrometer. A circulator is used as the microwave bridge element. The

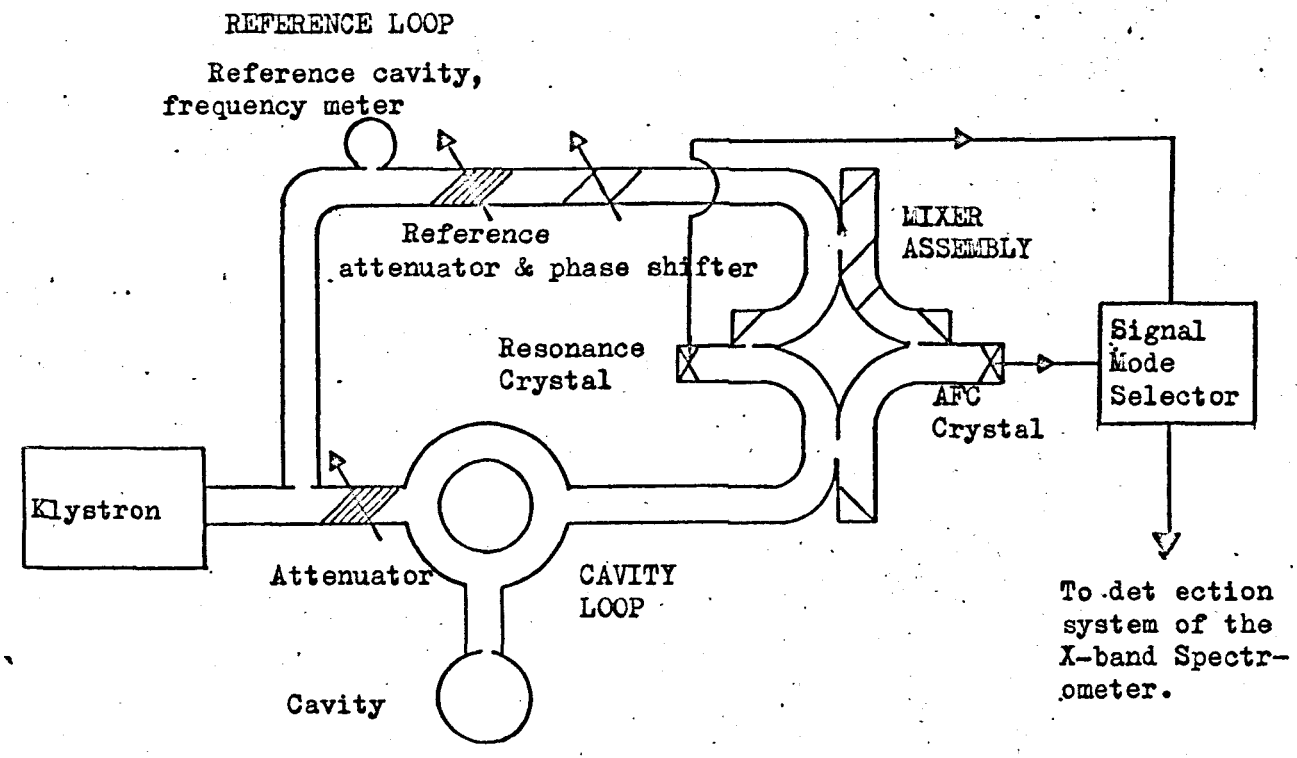

FIGURE 2.3 Varian Q-band microwave bridge. Power supplies and detection is via the X-band spectrometer.

reference loop which supplies bias to the resonance and AFC crystals contains a tuneable cavity to monitor the microwave frequency. The mixer assembly causes a phase difference of 90^{o} between the signal at the two crystals which facilitates the change from absorption to dispersion operation. The klystron is tuned to operate near to 35 GHz using the reference cavity and the klystron mode is then displayed to optimize cavity tuning and coupling.

A commercial cylindrical TE_{011} cavity is generally used for experiments down to 77 K, but at lower temperatures a similar cavity manufactured in the Departmental Workshop is used. Generally magnetic field modulation is at 100 KHz, although at low temperatures audio frequencies are used.

2.4 Fieldial Magnetic Field Regulator

The Fieldial regulator used to control the static magnetic field on both spectrometers is illustrated schematically in figure 2.4.

A Hall-effect crystal in the magnetic field is excited at 1.29 KHz, together with the field set and sweep range controls. The latter two are designed to maintain a fixed combined resistance throughout the range of control. The probe output Hall voltage is combined with the voltage from the field set and range controls at the input of the error amplifier. The sweep percent of range control produces a proportional error signal, the maximum amplitude of which depends upon the sweep range control. Zero input to the error amplifier results from static conditions. Any change results in an error signal voltage which, after phase sensitive detection, gives a d.c. output which is applied to the current controlling circuits in the magnet power supply. The resultant change in magnet current again results in zero voltage at the error amplifier. The stability of the system is better than 1 ppm short term for the Varian spectrometer magnet. Improved stability is achieved using the Mark II Fieldial in which the error amplifier, phase detector and Hall effect crystal are

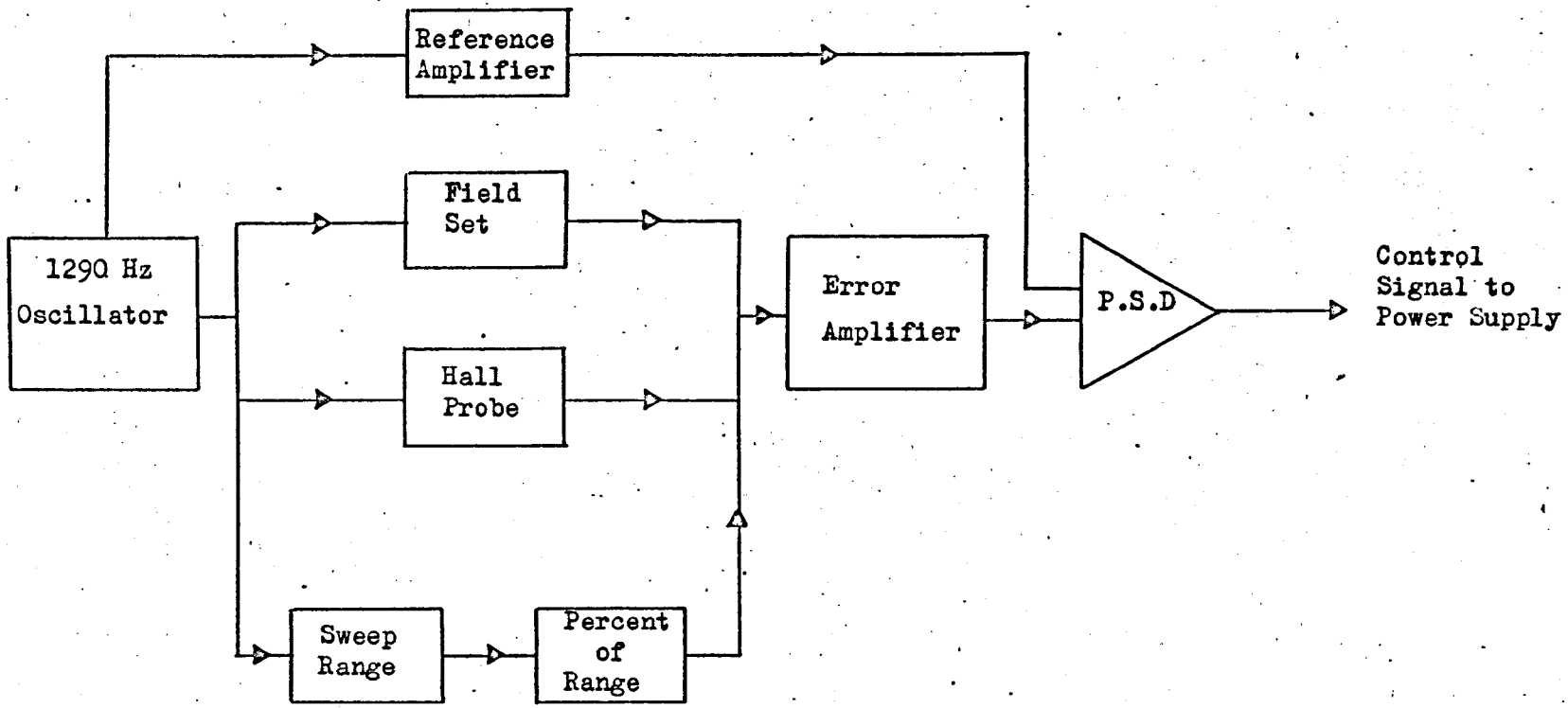

FIGURE 2.4 Schematic diagram of the Varian Fieldial Magnetic Field Regulator.

temperature stabilized.

The field control units have a d.c. voltage output which is proportional to the setting of the percent sweep control. This was used to drive the X-axis of an X-Y pen recorder. A proton/lithium resonance nmr probe and Hewlett-Packard counter was used to continuously monitor the magnetic field during experimental runs when this was possible, and the magnets were kept well calibrated and adjusted throughout the period of experimental work.

2.5 ENDOR Techniques

The little-used technique of frequency swept ENDOR was used to measure accurately the hyperfine parameters of Re^{6+} in calcium tungstate. The nuclear RF field obtained from a voltage swept frequency oscillator (0 - 110 MHz) was fed through a 5 Watt broad band power amplifier to a coil wrapped around the sample which was included in a nominally matched coaxial transmission line. The selected RF range, which is swept through rapidly (in ~0.5 sec), is synchronised with the channel address of a digital signal averager, the input to which is the d.c. output of the Varian spectrometer's IF strip. The EPR transition is just saturated, and a nuclear transition registers as a small change in this d.c. level. The RF was generally swept several hundred times to obtain good signal to noise. This type of ENDOR spectrometer was first discussed by Unruh (1971) and was constructed in our laboratory in conjunction with Mr.P.Benson.

2.6 Measurement of Spin Lattice Relaxation Times

Relaxation times were measured by saturating a transition with pulses of resonant microwave power and monitoring the recovery of the transition with low power radiation. Saturating power was derived from a travelling wave tube (TWT) which is fed a few milliwatts of power from the signal klystron. One watt pulses at this frequency are obtained by switching the TWT power supply using a pulse generator. The variable

pulse generator built by Beswick (1973) was modified to include a single shot facility needed for measuring long relaxation times.

The relaxation traces can be analysed by comparison with the output of a double exponential generator synchronised to the pulse generator, using a double beam oscilloscope.

CHAPTER III

INVESTIGATION OF A HEAVILY NEUTRON IRRADIATED SAMPLE OF CALCIUM TUNGSTATE

3.1 Introduction

van Uitert and Soden (1960) first suggested that the divalent metal ion tungstates might be useful diamagnetic hosts for incorporating paramagnetic ions. Although they could be grown only with some difficulty, it soon became clear that these compounds, and especially $CaWO_4$, were almost ideal for EPR purposes; when their suitability for solid-state maser action was realised, additional interest was stimulated. Since 1960 the scheelites (tetragonal tungstates) have been a fruitful area of research, particularly in Russia, where the use of $CaWO_4$ as a laser host has been extensively studied. EPR has now been used to examine many ions in the tungstates, and in some cases spin-lattice relaxation times have also been measured. Recently the Russians have followed work started in America on the effect of an external electric field on the EPR of impurity ions, because both cation sites lack inversion symmetry (see Mims and Gillen,1966 and Birchurin et al.,1971).

In addition to the impurity ions which have been studied in $CaWO_4$, several EPR investigations have been made into the defect structure of crystals exposed to X-rays, γ-rays or fast neutrons. These studies have been undertaken to help in the understanding of the defects involved in the coloration of calcium tungstate by prolonged laser action. Unfortunately the absence of hyperfine lines has often made the firm identification of defects impossible.

3.2 Crystal structure of calcium tungstate

The crystal structure of calcium tungstate (scheelite) is characterized by the space group C_{4h}^6. The tetragonal body-centred unit cell, in which there are four molecules, has the dimensions (Wycoff,1960)

$$a = b = 5.243 \pm 0.002 \text{ A}$$

$$c = 11.376 \pm 0.003 \text{ A} .$$

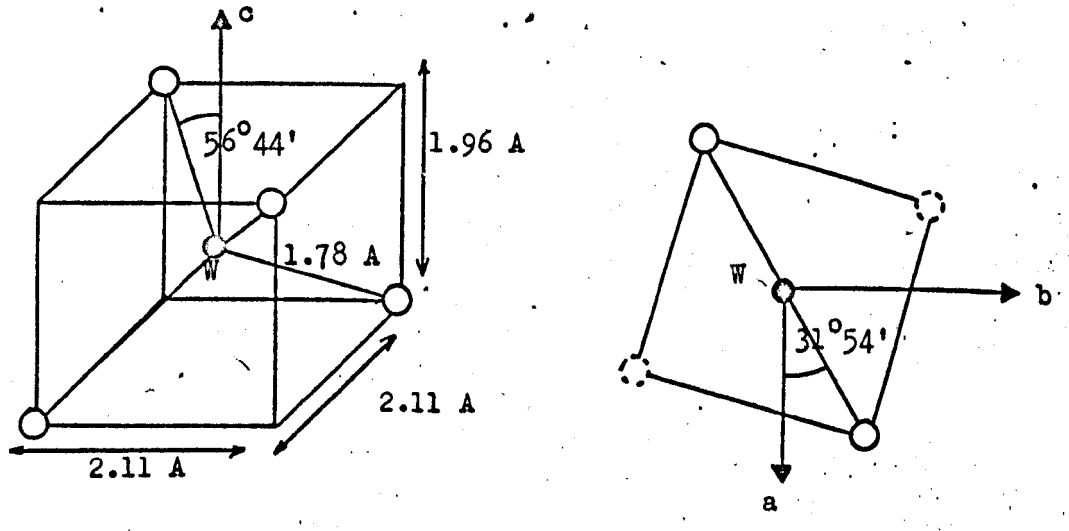

(a) Tungsten tetrahedron.

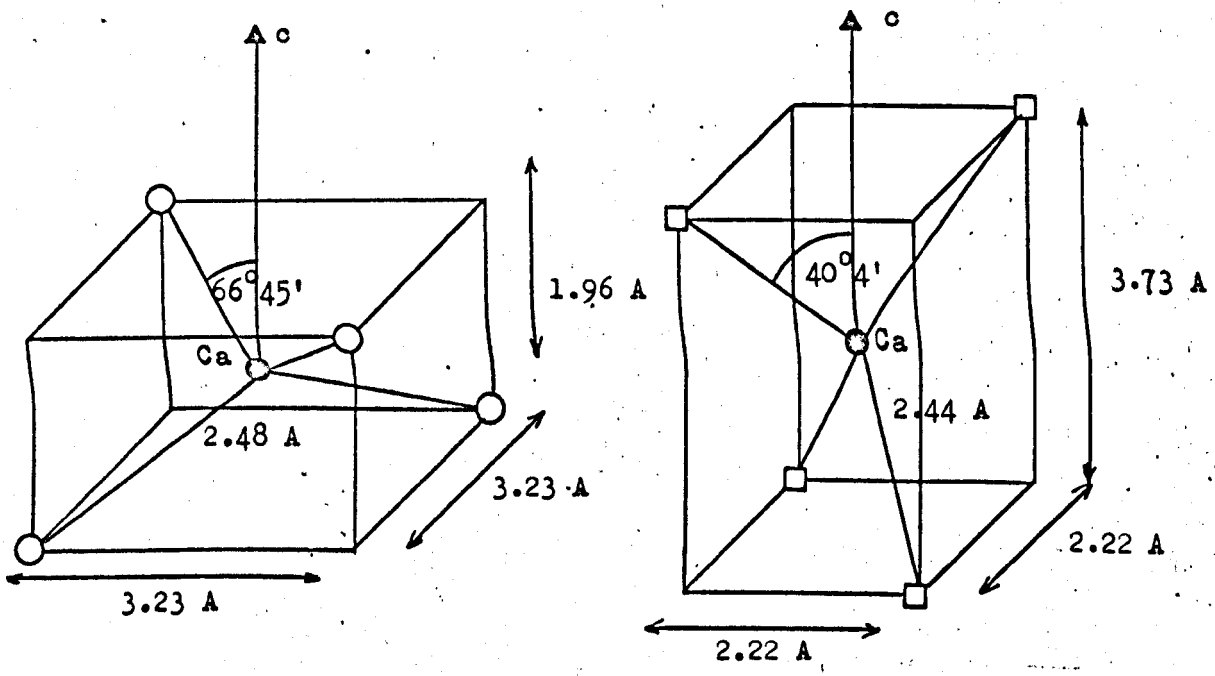

(b) Calcium tetrahedra

FIGURE 3.1 Oxygen tetrahedra about metal ions in calcium tungstate. After Hempstead and Bowers, 1960.

TABLE 3.1

Results of chemical and mass spectrographic* analysis of the boule from which the crystal was taken (units μg/g)

Al	Cl	Cu	Fe	K	Mg	Mn	Mo	Si	Sr
15	20	5	7	15	12	2	30	35	15

* Elements specifically sought but not detected included Ba, B, Cd, Ga, Ir, Na, Ni, P, Pb, Pt, Rh, Sb, Ti, V, Zn.

The structure is best viewed as being composed of WO_4^{2-} anions ionically bonded to Ca^{2+} cations. Each of the anions consists of a central W atom covalently bonded to four tetrahedrally disposed O atoms. Metal ion sites are found on planes separated by c/4 and perpendicular to the c axis. They are equivalent in pairs, indistinguishable by EPR, one pair being derived from the other by reflection through the body centre. Figure 3.1 shows the oxygen tetrahedra about the two metal ions, and the relationship of the tungsten tetrahedron to the crystal axes. The tetrahedron about the tungsten atom is squashed along the c axis, whilst surrounding the calcium atom there is one squashed and one extended tetrahedron. From the crystallographic data the point symmetry is S_4 at both metal ion sites. Mims (1965) has unambiguously established this for the calcium site using the results of electric field shift experiments on EPR lines.

3.3 The experimental crystal

The dark coloured neutron irradiated sample of calcium tungstate investigated by Weightman (1968) was used in these experiments. It was cut from a boule grown by the Czochralski method along the c axis by Cockayne at RRE, Malvern. The high purity of the sample is indicated by the chemical and mass spectrographic analyses of the crystals shown in Table 3.1. A preliminary EPR survey of the crystal down to 4.2 K prior to irradiation revealed that the only paramagnetic centres present were Mn^{2+} and Fe^{3+} (Henderson,1965). Irradiation in the DIDO reactor at UKAEA, Harwell in a flux of 2×10^{13} n $cm^{-2}s^{-1}$ for a period of four months resulted in a fast neutron dose of 2.7×10^{20} nvt. The corresponding thermal neutron dose was $\sim 10^{21}$ nvt. Weightman studied paramagnetic damage centres produced by the neutron irradiation. In the course of his work he first observed, but did not study, the spectrum reported here. Since the crystal was cut from a c axis boule this principal direction was easily determined. The directions of the other two principal axes were determined using the angular dependence of the A and C spectra

FIGURE 3.2 Angular variation of the spectrum at 77 K, B directed from the crystal ab plane to the c axis. Dashed lines indicate where the exact behaviour of the spectrum was difficult to follow.

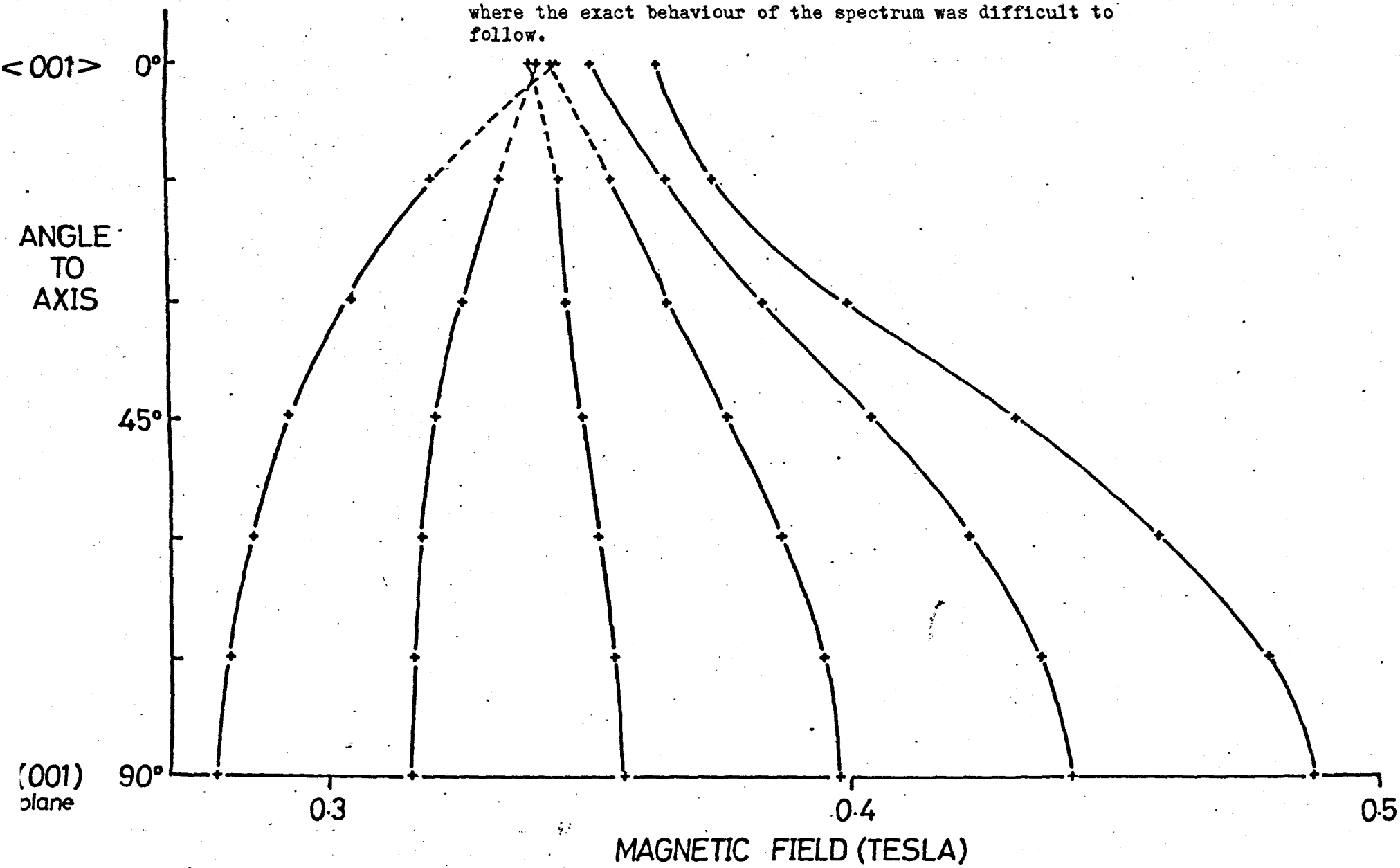

reported by Weightman (op cit), Weightman et al (1972,1973).

3.4 Preliminary investigation of the irradiated sample

The spectrum with the magnetic field, B, directed in the crystal ab plane consisted of six strong, broad lines which were observed only at temperatures of 77 K and below. They were partly obscured by sharp resonances from the large number of defects in the crystal. Spaced almost equally over a range of ~ 0.2 T, the lines were centred near $g \approx 1.72$. Only the line at highest field was not interfered with by defect resonances for crystal rotations about the c axis, but all the lines appeared invariant to within ~ 0.5 mT. When the crystal was rotated from a direction in the ab plane towards the c axis the lines converged to a magnetic field of ~ 0.35 T. The large number of other lines in this region of the spectrum made it impossible to establish whether this spectrum collapsed to a single line, crossed, or whether the lines moved close together at a turning point. Without accurate data in this critical region the nature of the centre and the form of the spin Hamiltonian describing it remained obscure. Table 3.1 shows that apart from manganese and iron the only other common elements in the crystal which normally have paramagnetic ions were copper and molybdenum, but both these were at a concentration too low to account for the observed spectrum. These preliminary experiments did not distinguish between an impurity ion and a lattice defect, so it was decided to anneal at high temperatures a sample cut from the irradiated crystal - lattice defects are generally removed by such treatment. The anneal was carried out at 1200 C for 24 hours, the temperature being increased and decreased slowly to avoid thermal shock. After this treatment the formerly black, opaque crystal was now a clear green colour. When it was examined in the EPR spectrometer the spectra due to all the defects had disappeared, but the six broad lines remained.

3.5 Investigations of the annealed sample at 77 K

After annealing the sample the orientation dependence of the six

(a) B almost exactly along the crystal c axis

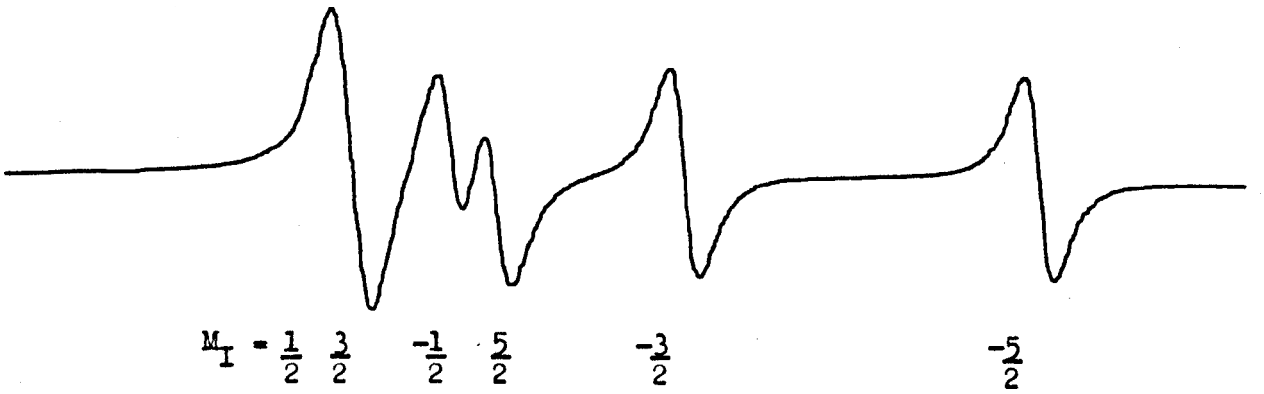

(b) B in the crystal ab plane, when the lines did not move.

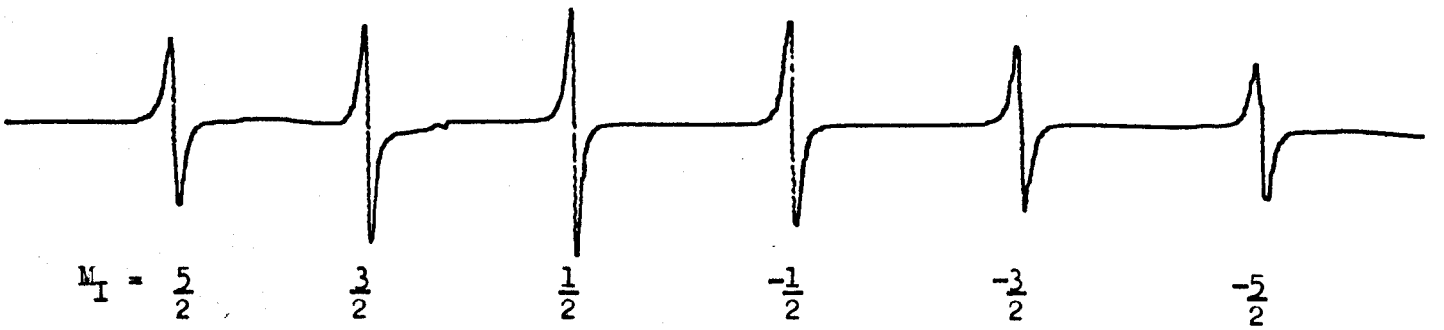

(c) B at 5° to the c axis, showing the large number of unresolved lines.

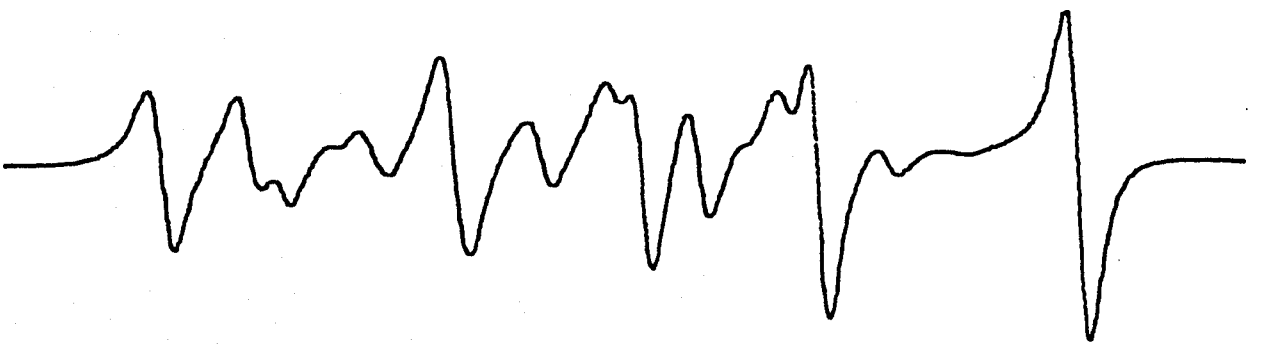

FIGURE 3.3 SPECTRUM AT 77 K.

FIGURE 3.4 (a) Schematic diagram of the energy levels of an $S = \frac{1}{2}$, $I = 5/2$ spectrum.

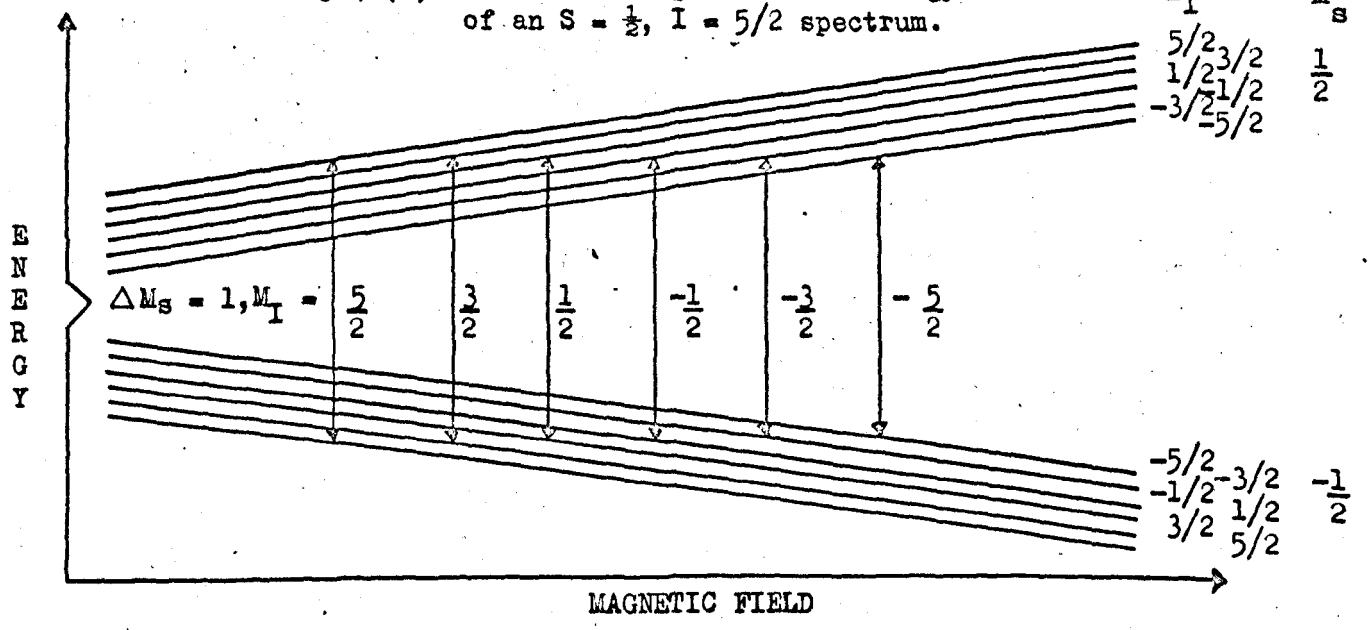

FIGURE 3.4 (b) Actual energy levels at 77 K, $\underline{B} \| c$. Vertical arrows indicate observed transitions for incident quantum of energy 0.30929 cm^{-1}.

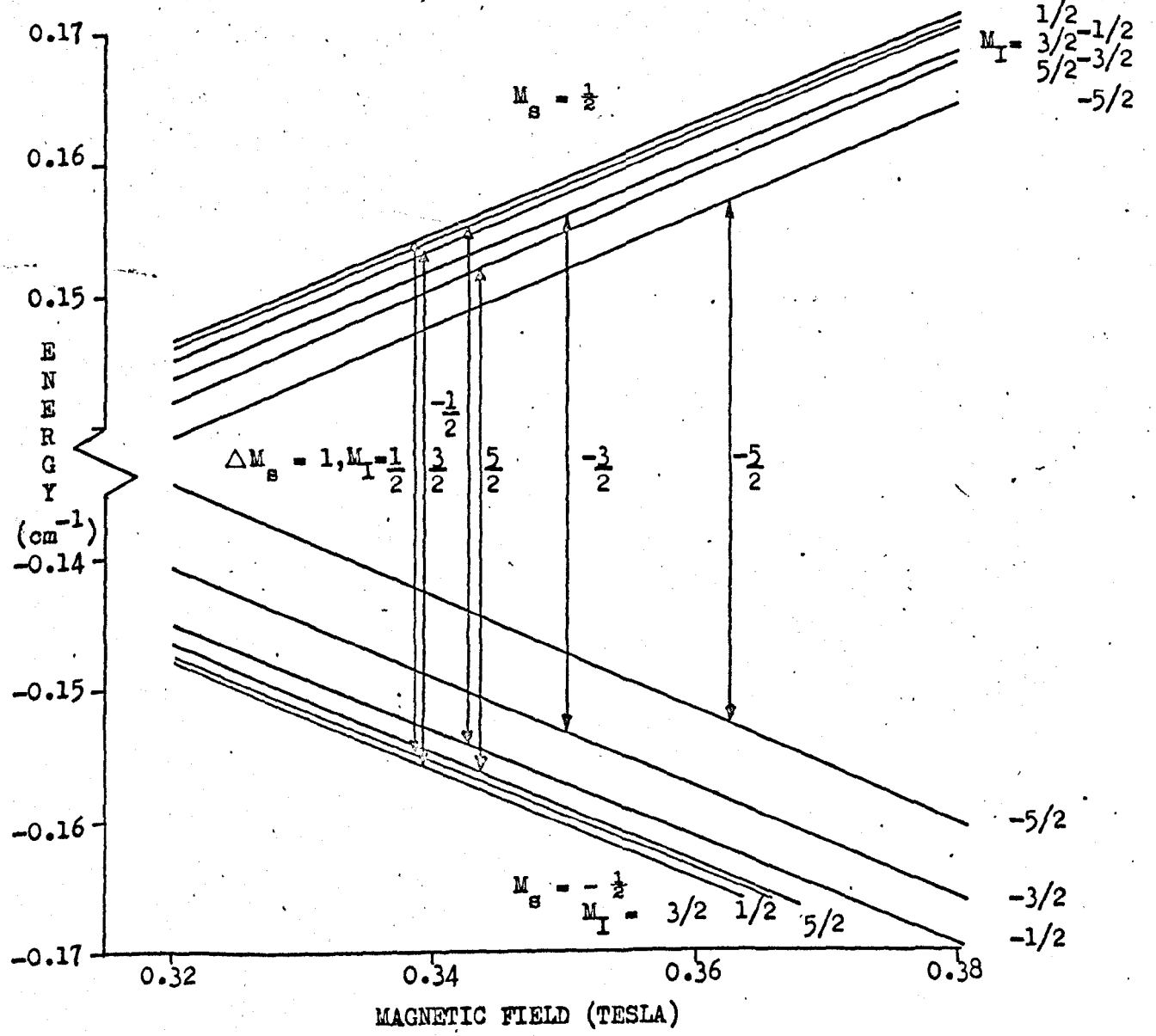

line spectrum was much simplified and the spin Hamiltonian parameters could be determined accurately. The line positions were confirmed to be invariant in the ab plane (Fig.3.3b), whilst crystal rotations in the magnetic field from the ab plane to the c axis (Fig.3.2) showed the involvement of a hyperfine interaction at an axially symmetric centre with $S = \frac{1}{2}$ and $I = 5/2$. However, the exact behaviour of the spectrum when the magnetic field was directed near to and along the c axis was difficult to follow. From 30° to within 1° of the c axis there were fifteen or more transitions, and some of these became more intense whilst others decayed as the c axis was approached. In Fig.3.3, (a) shows the spectrum with $\underline{B}$ directed almost exactly along the c axis, and (c) shows the spectrum with $\underline{B}$ at 5° to this axis when only the line to high field can be unambiguously identified as an allowed transition.

The large hyperfine splitting in the ab plane suggested that spin Hamiltonian parameters determined using perturbation theory would be inaccurate. Consequently the spin Hamiltonian for $S = \frac{1}{2}$, $I = 5/2$,

$$\mathcal{H} = g_{\parallel} \mu_B B_z S_z + g_{\perp} \mu_B (B_x S_x + B_y S_y) + A_{\parallel} S_z I_z + A_{\perp} (S_x I_x + S_y I_y) \qquad 3.1$$

was directly diagonalized using MNES, an iterative computer program written by Dowsing (1970) and modified by the author. This program, described in detail in Appendix A, obtains the best fit Hamiltonian parameters by a non linear least squares fit to the resonance data. The input data for this program consists of magnetic fields at resonance for specified orientations and starting values for the spin Hamiltonian parameters; in addition identification of the various transitions is required. The program solves Eq.3.1 for the energy levels, which are labelled 1,2,3.....12 in descending order of energy. The disposition of the 12 levels expected from a system with $S = \frac{1}{2}$ and $I = 5/2$ is illustrated schematically in Fig.3.4a. For small positive values of $A_{\parallel}$ and $A_{\perp}$ these levels can be identified by the usual $|M_S, M_I\rangle$ representation as shown, and allowed magnetic dipole transitions ($\Delta M_S = \pm 1$, $\Delta M_I = 0$) occur between levels 1-12, 2-11....6-7.

The best fit between measured and predicted transitions is then achieved by iteration of the spin Hamiltonian parameters in an order specified by the operator in the input data. Proceeding in this manner a good fit to the data was rapidly achieved for values of θ in the range 20° to 90°. However, for smaller values of θ, and especially for $\theta = 0^{\circ}$ ($\underline{B} \| c$ axis), the fit was unsatisfactory. It was realized that incorrect identification of the transitions was responsible for the poor fit, this being connected with the fact that the transitions, uncharacteristically for hyperfine structure, are not symmetrically spaced near $\theta = 0^{\circ}$ (Fig.3.3a,c). This problem was alleviated by writing a small computer program which solved the matrix of Eq.3.1 for $\underline{B}$ directed along the z (c) axis analytically. This can only be done for this orientation of the crystal in the magnetic field because the matrix factorizes into six 2 x 2 matrices. Allowed transitions for which the energy between levels was nearest to the energy of the microwave quantum were found for each observed field position using parameters which gave a reasonably good fit to the data. The appropriate levels were then identified in order of energy for the iterative program. The order of energy levels was found to be very sensitive to the size of $A_{\|}$ for all but the two high field transitions (5-8, 6-7), and this meant that when a new set of best fit parameters had been obtained, the old transition identifiers were no longer correct. The correct identifiers for these parameters could be found again using the small program, and these could then be fed into the iterative program using the last best fit parameters as the starting values. This procedure had to be repeated several times to obtain consistent agreement, but the process converged to give the following parameters:

$$g_{\|} = 1.8491 \pm 0.0003$$

$$g_{\perp} = 1.7162 \pm 0.0003$$

$$A_{\|} = 0.0030 \pm 0.0003 \ \text{cm}^{-1}$$

$$A_{\perp} = 0.0331 \pm 0.0003 \ \text{cm}^{-1} .$$

A nuclear electric quadrupole term was not included in the spin Hamiltonian at this stage because the shifts so introduced were smaller than the error involved in measuring the line positions, which is determined by the linewidth of $\sim$2 mT. The mean deviation of the experimental line positions from those calculated for the best fit parameters was $\sim$0.3 mT.

The transitions for the spectrum in the ab plane are identified by the nuclear quantum numbers of the levels between which they occur in Fig.3.3b, in accordance with Fig.3.4a, assuming $A_\perp > 0$. This is the normal labelling sequence for hyperfine transitions in EPR, ranging from $M_I = +5/2$ at low field to $M_I = -5/2$ at high field. This ordering of the hyperfine levels does not occur in the $\theta = 0^o$ orientation (Fig.3.4b) due largely to the fact that contributions of order $A_\perp^2/B$ are comparable with the first order shifts due to $A_{||}$. The term in $A_\perp$ contributes the only off diagonal elements in the matrix of the spin Hamiltonian when $\underline{B}$ is along the z axis, and these connect states of the type $|M_s,M_I\rangle$ with either $|M_s-1,M_I+1\rangle$ or $|M_s+1,M_I-1\rangle$. It is because these matrix elements are of order one fifth the size of the diagonal elements that they can so influence the order of energy levels - they cause changes in the eigenvalues greater than the splitting caused by $A_{||}$ alone. If $A_{||}$ or the magnetic field (i.e. frequency) were larger by a factor of approximately 2 the energy levels and transitions would be in the usual order. The changing order of energy levels as the magnetic field direction became coincident with the crystal c axis suggested that some of the EPR lines should cross each other. This was not observed experimentally because of the large number of obscuring forbidden transitions. Thus the dashed curves on Fig.3.2 indicate only allowed lines, the projected movement being based on their idealized character. The fact that the two high field lines were observed not to cross indicates that $A_{||}$ and $A_\perp$ have the same sign.

3.6 The identity of the centre

Following these experimental results a positive identification

of the centre assumed some importance. Nuclear Tables (Lederer, Hollander and Perlman,1967) show that there are four elements, aluminium, manganese, iodine and praseodymium each with one naturally occurring isotope with nuclear spin I = 5/2. Of these iodine was considered most unlikely since the most probable paramagnetic states arise from an electron in a 6s orbital, or a hole in a 5p orbital, neither of which would normally show a marked negative shift in the g-value. Aluminium also seemed unlikely for two reasons. Firstly it was found to be present at a level of only 15 ppm by weight before irradiation, a concentration too low to account for the intensity of the observed spectrum. Secondly, the most probable paramagnetic ion, Al^{2+}, exhibits the $3p^1$ electronic configuration which would not normally have a large g-shift. Garrison and DuVarney (1971) have observed Al^{2+} in axial sites in BeO to have g-values near 2.004; the isoelectronic B^{2+} ion also in an axial site in BeO has similar g-values. Praseodymium was dismissed as a serious candidate when a search in the literature revealed that crystals of $CaWO_4$ doped with the element had been grown, but no EPR spectrum was observed at X or Q-band down to 4.2 K (Kirton,1965). The EPR of Mn^{2+} substituting for Ca^{2+} is well known in calcium tungstate (Hempstead and Bowers,1960), and this spectrum was still visible in the sample at roughly the same low intensity as before irradiation. Consequently, unless the chemical analysis of part of the boule which was not irradiated was grossly unrepresentative of the rest, manganese seemed unlikely. Furthermore, the element would have to be present as Mn^{6+} ($3d^1$, $S = \frac{1}{2}$) to account for the observed spectrum, and this valence is known to be chemically unstable (Cotton and Wilkinson,1966).

In addition to the four elements discussed above, europium and rhenium each have two isotopes with I = 5/2. Europium can be discounted since the nuclear moments of the two stable isotopes, 3.441 and 1.521 nuclear magnetons respectively, would contribute an easily resolved splitting of ~ 10 mT between lines from different isotopes for a hyperfine

TABLE 3.2

Properties of Tungsten and Rhenium Isotopes

Isotope	Natural Abundance %	Thermal neutron capture cross-section (Barns)	Half-life	Magnetic Moment (Nuclear Magnetons)
^{180}W	0.135	<20		
^{182}W	26.46	20		
^{183}W	14.48	11		
^{184}W	30.67	2.1		
^{185}W		?	74 days	
^{186}W	28.4	36.0		
^{187}W		90.0	23.9 hours	
^{185}Re	37.07	110		3.1437
^{187}Re	62.93	70		3.1760

interaction of ~40 mT. This left as the only candidate rhenium, whose isotopes Re^{185} and Re^{187} have nuclear moments of 3.1437 and 3.1760 nuclear magnetons respectively. This small, 1%, difference in the magnetic moments of the two isotopes made the element a possibility, for the lines from each isotope could be obscured in the overall width of the resonance lines. However, an explanation for the presence of rhenium in the crystal had to be found, since it was not observed mass spectrographically before irradiation. That rhenium is on the right of tungsten in the Periodic Table of the Elements, in the third series of transition metals, suggested a likely explanation. Tungsten is present in calcium tungstate as essentially W^{6+}, $5d^0$. On the other hand Re^{6+} would be $5d^1$, a paramagnetic ion with $S = \frac{1}{2}$. Furthermore, Nuclear Tables indicated that nuclei of the naturally occuring tungsten isotopes could capture slow neutrons during irradiation, and decay by β^- emission to isotopes of rhenium (Lederer et al, op cit). The possibility of nuclear transmutations in the solid state was therefore examined in greater detail.

3.7 Neutron capture by tungsten nuclei

The ease with which a nucleus will absorb a neutron i.e. how large its neutron capture cross-section is, depends critically on the energy of the incident neutron. The most important energy range is between 0.001 and 1.0 eV, the thermal neutron region, when the neutron capture cross-section of most nuclei is generally highest. In this region the cross-section is usually inversely proportional to the neutron velocity, so the number captured is strictly proportional to the neutron density. The thermal neutron capture cross-section is therefore the most important parameter to bear in mind when discussing possible reactions.

The relevant properties of the five naturally occurring isotopes of tungsten are listed in Table 3.2. Although isotope 180 will capture a neutron to form radioactive W^{181}, its natural abundance is very small. Isotopes 182 and 183 form stable W^{183} and W^{184} on capture, but the two

FIGURE 3.5 Proposed nuclear reaction scheme for the generation of Re from W by neutron irradiation.

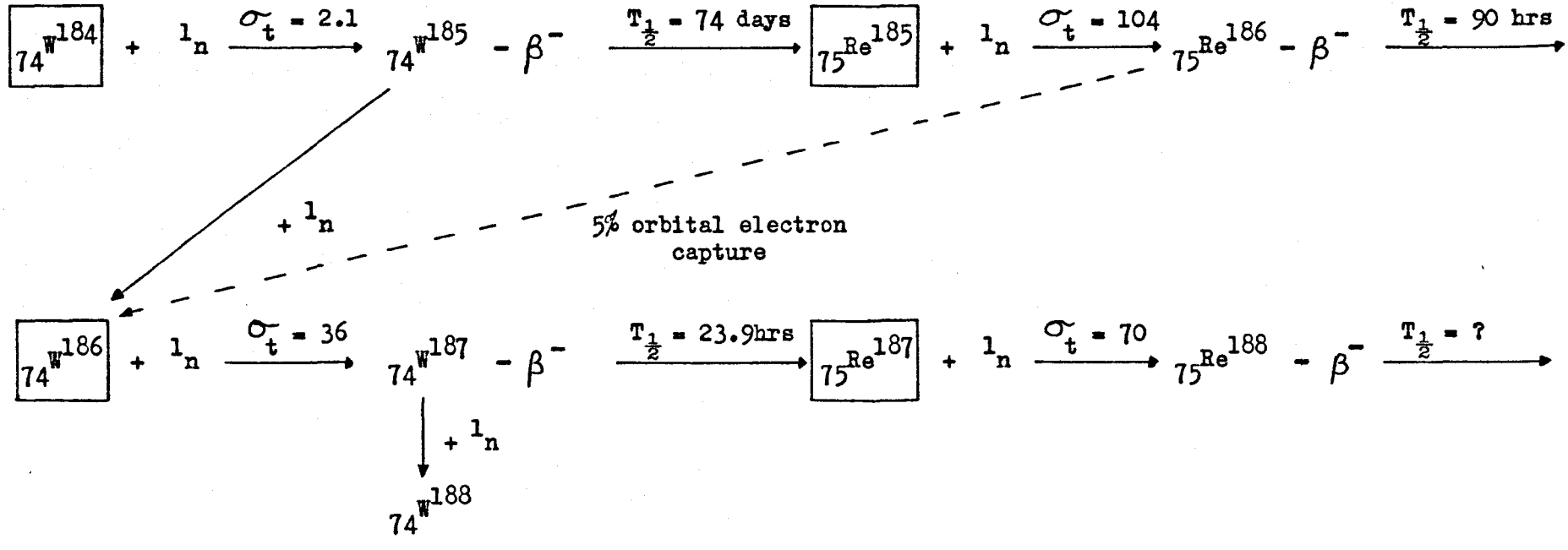

most abundant isotopes, W^{184} and W^{186}, both capture neutrons with reasonable facility to form radioactive W^{185} and W^{187} respectively. W^{185}, with a half life of 74 days, decays by β^- emission to $_{75}Re^{185}$, whilst W^{187} decays similarly to $_{75}Re^{187}$ with a half life of 23.9 hours. These are the only naturally occurring isotopes of rhenium, their abundances being 37.07% and 62.39% respectively. The proposed reaction scheme is illustrated in Fig.3.5, which shows that after formation both rhenium isotopes can capture neutrons, which drains their formation, but of the Re^{185} lost in this way, 5% will decay by orbital electron capture to form starting isotope W^{186}. For calculation purposes the reaction scheme can be generalized:

$$A + {}^1n \xrightarrow{\sigma_A} \underset{\sigma_B \downarrow + {}^1n}{B} - \beta^- \xrightarrow{\lambda_B} C + {}^1n \xrightarrow{\sigma_C} E. \qquad 3.2$$
$$D$$

A (thermal neutron capture cross-section σ_A) captures a neutron and forms B which decays by β^- emission with decay constant λ_B to form C, the element we wish to make. Some B or C can be lost by neutron capture (cross-section σ_B, σ_C) forming D or E. The rate of formation of B from A is

$$\frac{dN_B^t}{dt} = nv\,\sigma_A N_A^o \qquad 3.3$$

where nv is the thermal neutron flux, and N_x^t represents the density of species X at time t. Strictly speaking N_A^o should be replaced by $N_A^t = N_A^o - N_B^t$, but provided there is less than a 5% change in N_A the error introduced is less than 0.2%. Some of B will be lost by decay to C, and some by neutron capture:

$$-\frac{dN_B^t}{dt} = \lambda_B N_B^t + nv\,\sigma_B N_B^t \qquad 3.4$$

Hence the overall rate of formation of B is

$$\left[\frac{dN_B^t}{dt}\right]_{overall} = nv\,\sigma_A N_A^o - N_B^t(\lambda_B + nv\,\sigma_B) \qquad 3.5$$

Solving this equation for N_B^t, applying the condition that $N_B^o = 0$ at $t = 0$ gives

$$N_B^t = \frac{nv\sigma_A N_A^o}{(\lambda_B + nv\sigma_B)} \left[1 - e^{-(\lambda_B + nv\sigma_B)t}\right] \qquad 3.6$$

The rate of formation of C is the difference between its rate of formation by decay of B and its rate of loss by neutron capture:

$$\frac{dN_C^t}{dt} = \lambda_B N_B^t - nv\sigma_C N_C^t \qquad 3.7$$

This equation can be solved by the integrating factor method after substituting for N_B^t using Eq.3.6. Applying the condition that at $t = 0$, $N_C^o = 0$ we find that

$$N_C^t = \frac{\sigma_A N_A^o}{\sigma_C} \cdot \frac{\lambda_B}{(\lambda_B + nv\sigma_B)} \cdot \left(1 - \left[\frac{nv\sigma_C e^{-(\lambda_B + nv\sigma_B)t} - (\lambda_B + nv\sigma_B)e^{-nv\sigma_C t}}{nv\sigma_C - (\lambda_B + nv\sigma_B)}\right]\right) 3.$$

Equation 3.8 can be simpified by considering the numerical values of the quantities involved. For a four month irradiation time $t \sim 10^7$ seconds, and so the integrated dose (nvt) approached $\sim 10^{21}$ neutrons. Taking a mean value for the σ's of 10 barns, and for the λ's of 10^{-6} (Table 3.2) we find that

$$nv\sigma \sim 10^{-9} \quad ; \quad nv\sigma t \sim 10^{-2}$$
$$\lambda_B \sim 10^{-6} \quad ; \quad \lambda_B t \sim 10$$

Hence the approximations

$$nv\sigma_C - \lambda_B \sim -\lambda_B \; ; \quad \lambda_B + nv\sigma_B \sim \lambda_B$$
$$nv\sigma_C e^{-\lambda_B t} \ll 1 \; ; \quad e^{-nv\sigma_C t} \approx 1 - nv\sigma_C t$$

allow 3.8 to be simplified to

$$N_C^t = N_A^o \, nvt \, \sigma_A \, . \qquad 3.9$$

This particularly simple result is intuitively correct, for provided neither B nor C are drained by their own neutron capture, all the A converted to B will eventually decay to form C.

Application of Eq.3.9 to the neutron irradiation of tungsten allows us to calculate that the two rhenium isotopes should be generated in the ratio of their parent tungsten isotopes' capture cross-sections:

$$\frac{N_{Re^{185}}}{N_{Re^{187}}} = \frac{\sigma_{W^{184}}}{\sigma_{W^{186}}} = \frac{2.1}{36} \approx \frac{1}{17} \qquad 3.10$$

The concentrations of the two rhenium isotopes in the $CaWO_4$ crystal should be ~0.01 atom % (Re^{185}) and 0.2 atom % (Re^{187}), indicating that the heavier isotope should be produced almost exclusively.

An immediate test of this hypothesis was made by comparing the intensity of the six line spectrum with the weak Mn^{2+} lines. The former spectrum was ~3000 times more intense, though this figure can only be regarded as a crude estimate because of the widely different lineshapes and intensities. The assumption that all the manganese in the crystal was present as Mn^{2+} gave a figure of 0.6 atom % for the concentration of the unknown centre. Remembering not only the different lineshapes, but also the difficulties involved in measuring both the neutron dose and the trace concentration of manganese, the agreement between calculation and experiment suggested strongly that the spectrum was due to Re^{6+}. However, an additional experiment was proposed in order to give confirmatory evidence. By cooling the crystal to 4.2 K the linewidth might decrease sufficiently for the lines due to the lighter rhenium isotope to be observed in the wings of the main Re^{187} lines. A measurement of the intensity ratio of the two sets of lines would provide absolute evidence.

3.8 Experiments at 4.2 K

Before any attempt was made to obtain the angular variation of the spectrum at 4.2 K, the crystal was oriented with its c axis parallel to the axis of rotation of the magnet. In accordance with the data taken at 77 K, the lines did not move as the magnet was rotated. The linewidth, which had decreased by a factor of ~5, was observed to

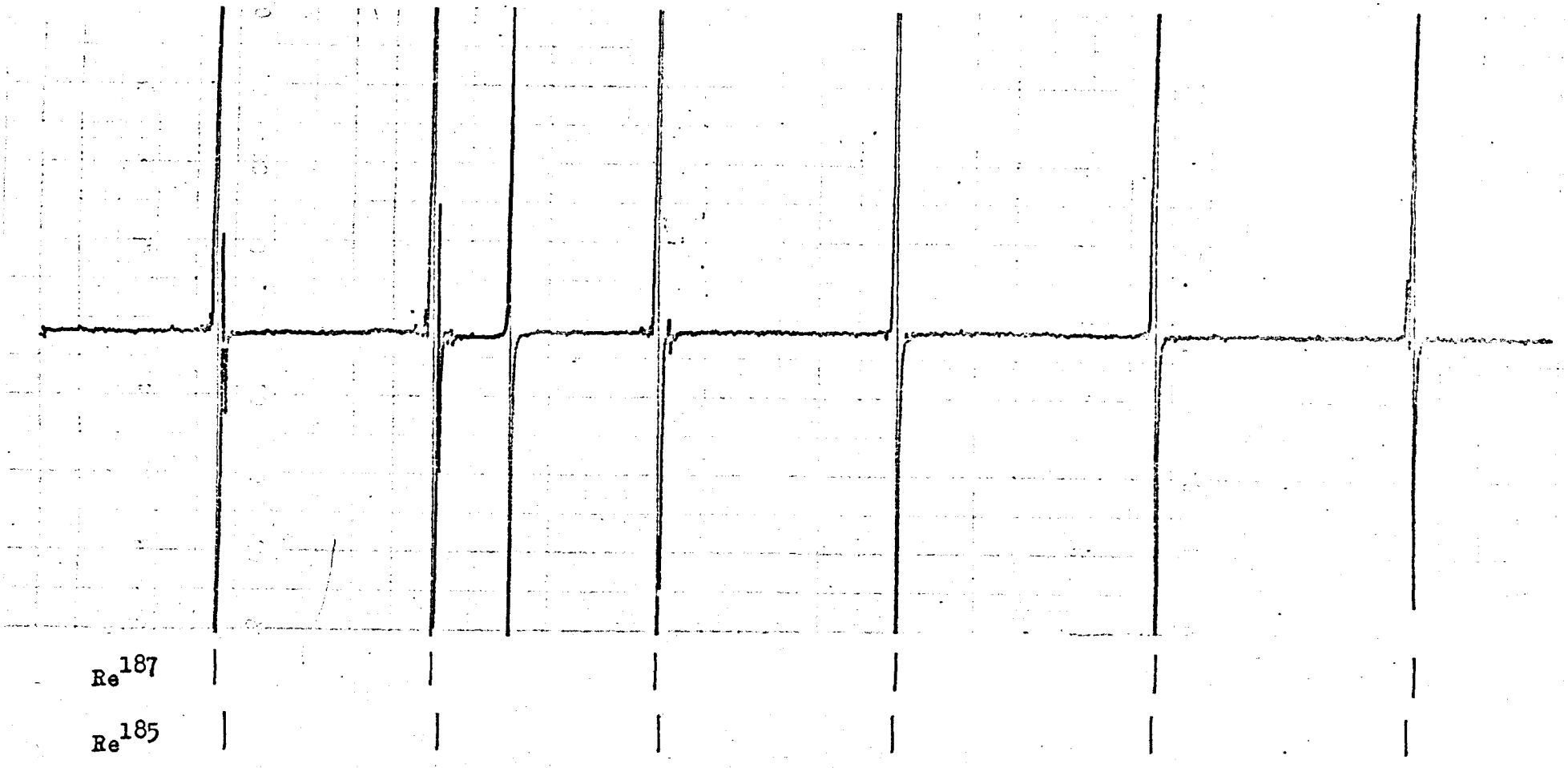

FIGURE 3.6 Re^{6+} at 4.2 K with $\underline{B}$ in the crystal ab plane showing lines due to Re^{185} in the wings of the larger Re^{187} lines. The narrow line third from the left is a carbon fibre g-marker. The total spread of the lines is ~0.2 T.

vary with angle, and at the position of minimum linewidth small lines were observed in the wings of all but one of the large lines. Figure 3.6 shows the whole spectrum recorded at this orientation of the magnetic field, with the small lines due to Re^{185} clearly visible on the $g \approx 1.71$ sides of the main lines. A rough estimate of the relative intensities of the two sets of lines gave a ratio of 10:1, compared with the calculated ratio of 17:1 and the ratio in nature of 2:3. This, together with the fact that the smaller lines were from a nucleus with slightly smaller magnetic moment, confirmed that rhenium, as Re^{6+}, was responsible for the spectrum.

Subsequent experiments were performed with the crystal mounted so that its c axis was in the plane of rotation of the magnet in order to further study the angular variation of the spectrum. Some difficulty was experienced in achieving the exact alignment of $\underline{B}$ along the c axis, since fine adjustments to the plane of the magnetic field could not be made with the low temperature cryostat in position. By performing an accurate experiment at 77 K the cut face on which the crystal was being mounted was found to be at an angle of 1.75° to the c axis. By using a wedge of this angle the spectrum in Fig.3.7 was recorded at 4.2 K with the magnetic field almost exactly along the c axis. The anticipated six lines are clearly visible, and an increase in linewidth would allow, misleadingly, a reconstruction of the 77 K spectrum for this orientation.

Several angular variation experiments were performed in order to obtain accurate data for fitting the spectrum to the spin Hamiltonian. Owing to the increased precision with which the line positions could be measured an axial nuclear quadrupole term of the form

$$P_{\parallel} \left(I_z^2 - \tfrac{1}{3}I(I+1)\right) \qquad 3.11$$

was added to the spin Hamiltonian 3.1. The angular variation of the spectrum was closely analogous to that at 77 K, but when a fit was attempted using the same transition identifiers there was again a

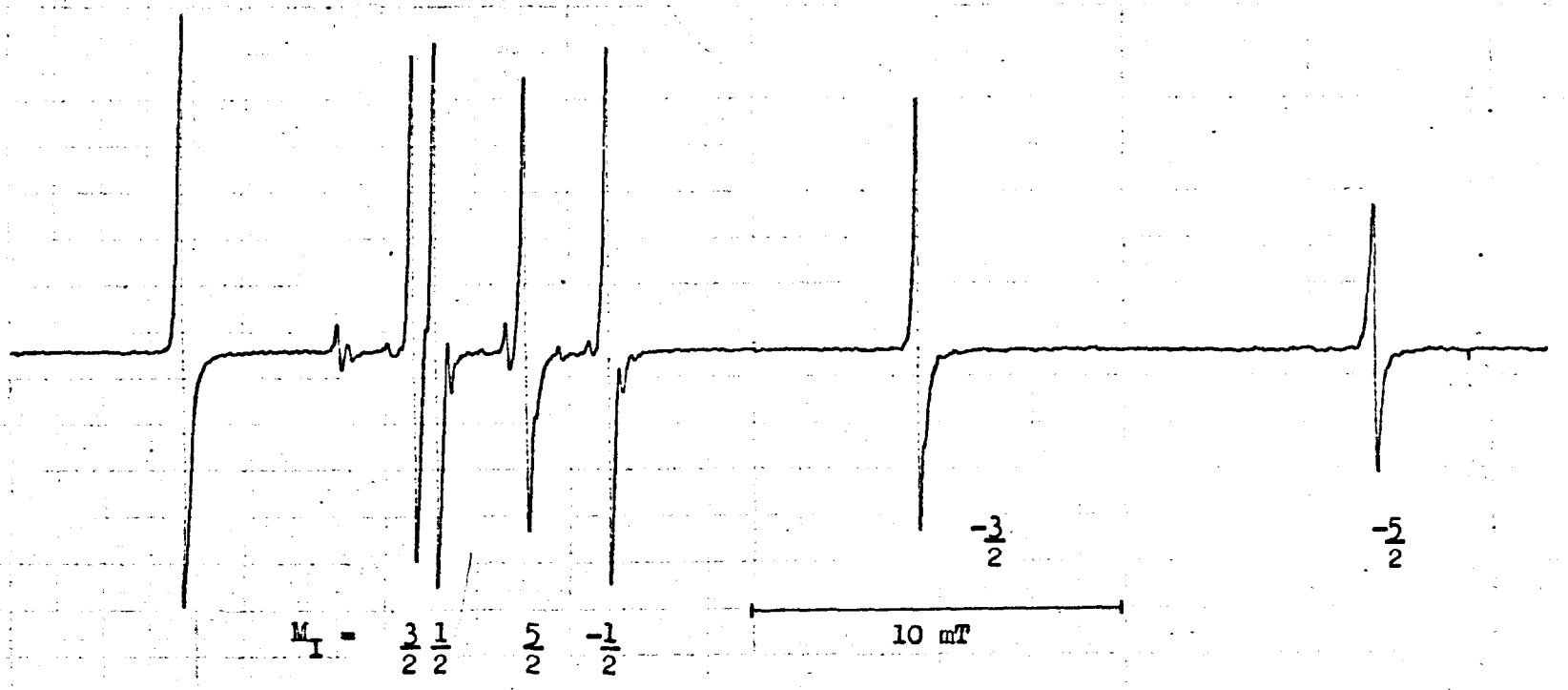

FIGURE 3.7 Spectrum of Re^{6+} at 4.2 K with $\underline{B}$ almost exactly along the crystal c axis. The line on the left is a carbon fibre g-marker at 0.3301 T.

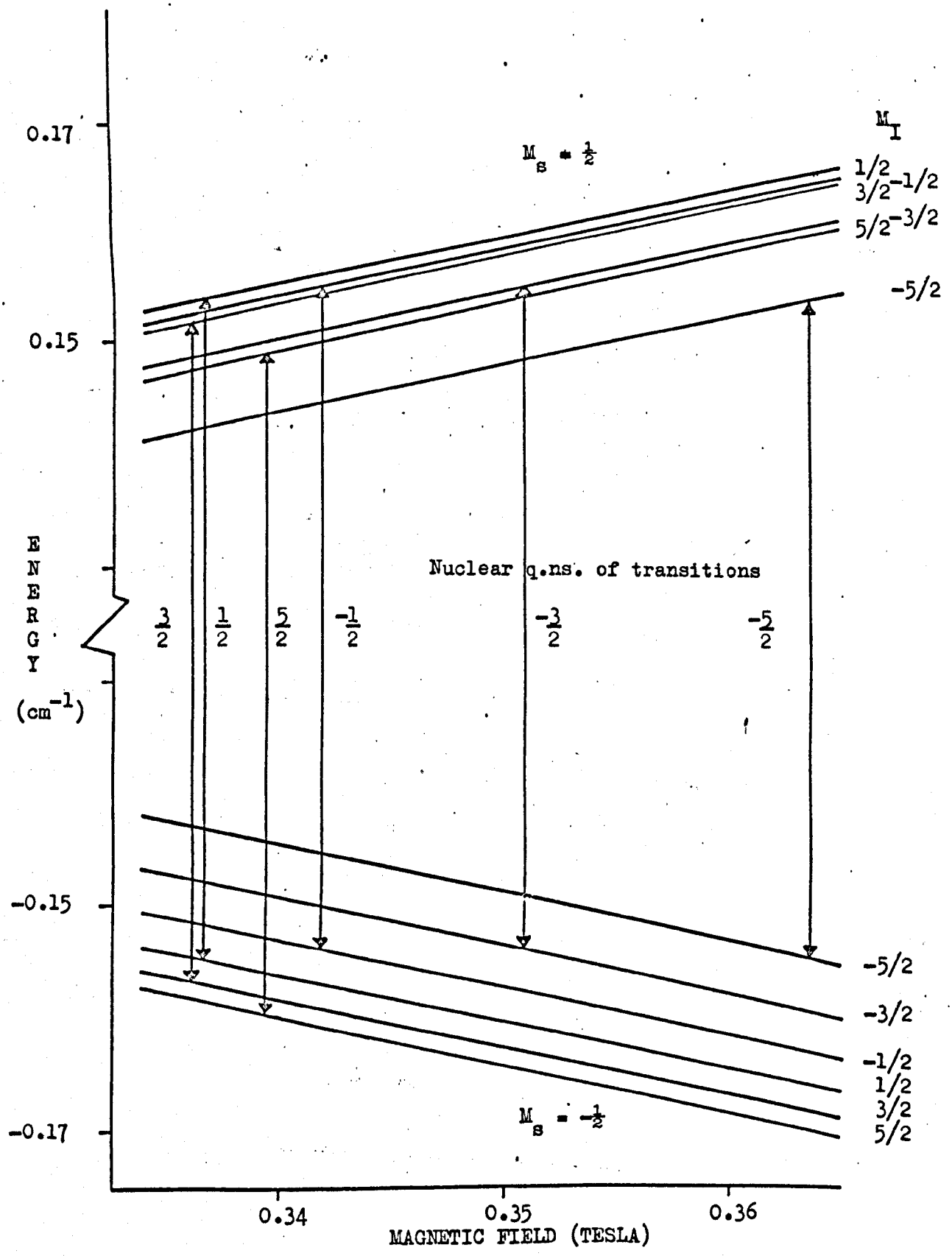

FIGURE 3.8 Energy levels of Re^{6+} at 4.2 K with $\underline{B} \| c$.

disparity at $\theta = 0^{\circ}$. The small program was used to reconstruct the energy levels for each best fit until consistent identifiers were found. The best fit spin Hamiltonian parameters were

$$g_{\parallel} = 1.8549 \pm 0.0002$$
$$g_{\perp} = 1.7164 \pm 0.0002$$
$$A_{\parallel} = 0.0042 \pm 0.0002 \quad cm^{-1}$$
$$A_{\perp} = 0.0324 \pm 0.0002 \quad cm^{-1}$$
$$P_{\parallel} = 0.0000 \pm 0.0003 \quad cm^{-1}$$

for Re^{187}, and for Re^{185}, assuming the same parameters parallel to the c axis,

$$g_{\perp} = 1.7167 \pm 0.0002$$
$$A_{\perp} = 0.0321 \pm 0.0002 \quad cm^{-1}.$$

The most interesting contrast with the 77 K parameters arises from the 30% increase in $A_{\parallel}$. This is sufficiently large to change the order of the energy levels, as can be seen from comparing Fig.3.8 with Fig.3.4b. The resultant EPR transitions, indicated by the long arrows, are also in different order. This is more closely related to that conventionally found in EPR due to the increased influence of $A_{\parallel}$. The zero value of $P_{\parallel}$ has been given because when the parameter was varied, no improvement on the fit could be obtained in the range of values quoted.

3.9 Forbidden transitions at 4.2 K

As at 77 K there were a large number of forbidden transitions when the magnetic field was directed near to the c axis, and the smaller linewidth facilitated the study of these lines. When the spectrum for Re^{187} was reconstructed by computer program ESRS (Dowsing,1970) using the above parameters, close agreement was obtained between the calculated and experimental positions and intensities of the allowed transitions. However, the fit to the forbidden transitions was not as good. Figure 3.9 shows the observed spectrum recorded with $\underline{B}$ at 20° to the c axis, and below this is the reconstructed spectrum, with which

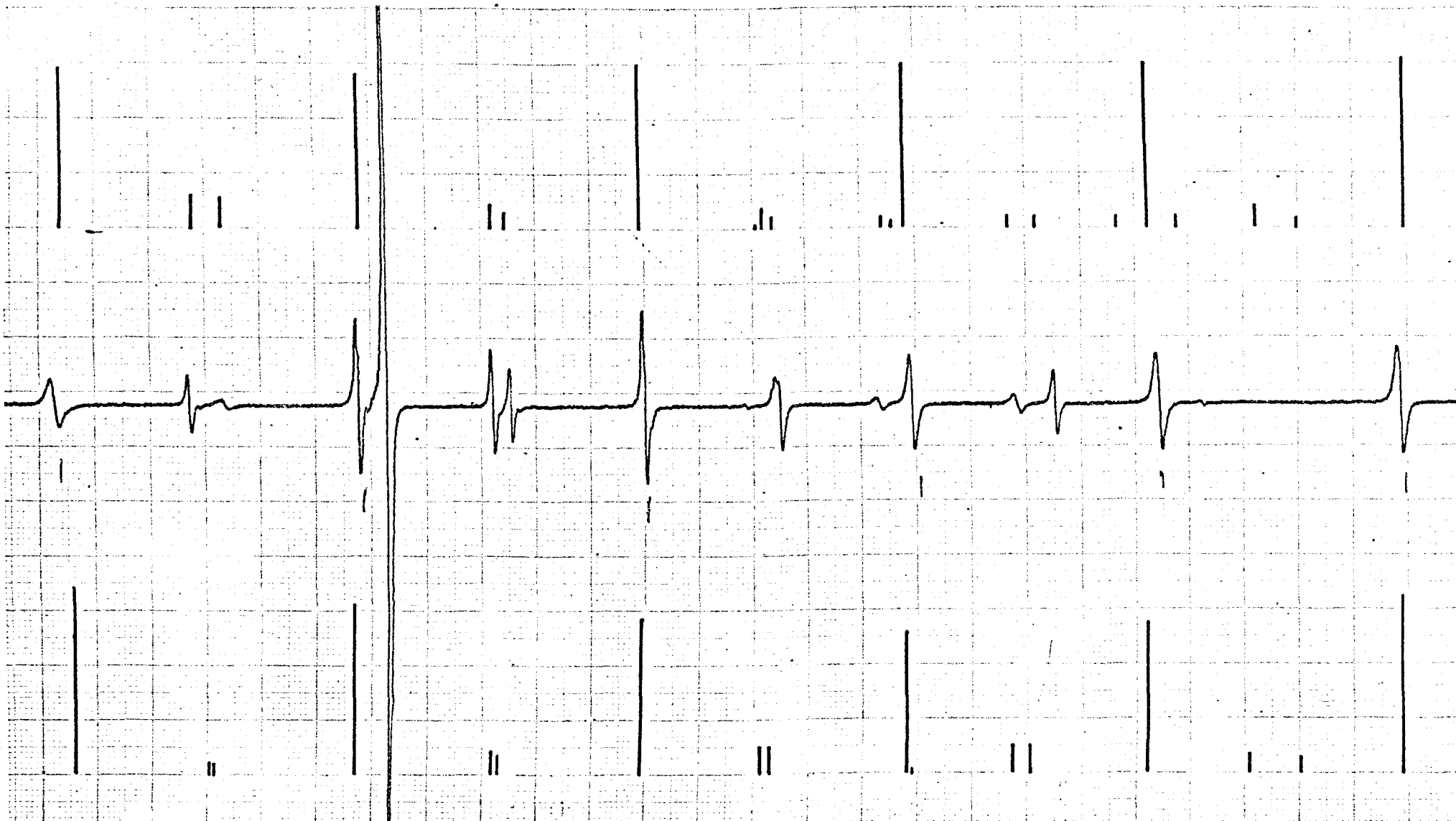

FIGURE 3.9 4.2 K Re^{6+} spectrum with $\underline{B}$ at 20° to the c axis. Below it is the line spectrum calculated for the best fit parameters and $P_{||} = 0.0000\ cm^{-1}$. The upper line spectrum was calculated using the same parameters except $P_{||} = -0.0008\ cm^{-1}$.

it can be compared. The vertical lines of the synthesized spectrum represent the calculated transition probabilities, proportional to the integrated intensity of the EPR lines; the high intensity lines on the left of Fig.3.9 is a carbon fibre g-marker. The poor fit of the forbidden transitions arises from the quadrupole term, Eq.3.11. This term, which has little effect on the allowed line positions, strongly influences both the position and intensity of the forbidden transitions. Consequently the spectrum was reconstructed with a quadrupole term varying between $\pm$ 0.001 cm^{-1} in increments of 0.0001 cm^{-1}. Generally speaking a positive value of $P_{||}$ resulted in greater splittings between pairs of forbidden lines and reduced intensities for the low field pairs. A negative quadrupole term also increased the splitting between pairs of lines, but it increased the transition probabilities of the low field lines. Examination of Fig.3.9 indicates that a negative value of $P_{||}$ is required; the value giving the most satisfactory synthesis was

$$P_{||} = -0.0008 \pm 0.0003 \ cm^{-1} .$$

The line spectrum at the top of Fig.3.9 was obtained using this value of $P_{||}$. The fit for the low field pairs of forbidden transitions and the allowed transitions is good, but the fit to the higher field forbidden transitions is not so satisfactory. As $P_{||}$ was made more negative, however, two competing effects were the increased splitting of the low field lines and the increasing intensity of the high field forbidden transitions, which had almost zero transition probabilities when $P_{||} = -0.0006 \ cm^{-1}$. This value of $P_{||}$ gave a low field forbidden line pair splitting of only 1.1 mT, half that observed. The larger error in $P_{||}$ reflects the difficulty in obtaining an exact fit to the observed spectrum.

Figure 3.10 is a plot of the experimentally observed line positions superimposed on the angular variation calculated using the best fit parameters for Re^{187} and $P_{||} = -0.0008 \ cm^{-1}$. The curves

FIGURE 3.10 Experimental line positions plotted against calculated angular variation with $\underline{B}$ near to the c axis. Dots represent experimental line intensities less than 1/3 rd., triangles intensities greater than 1/3 rd.

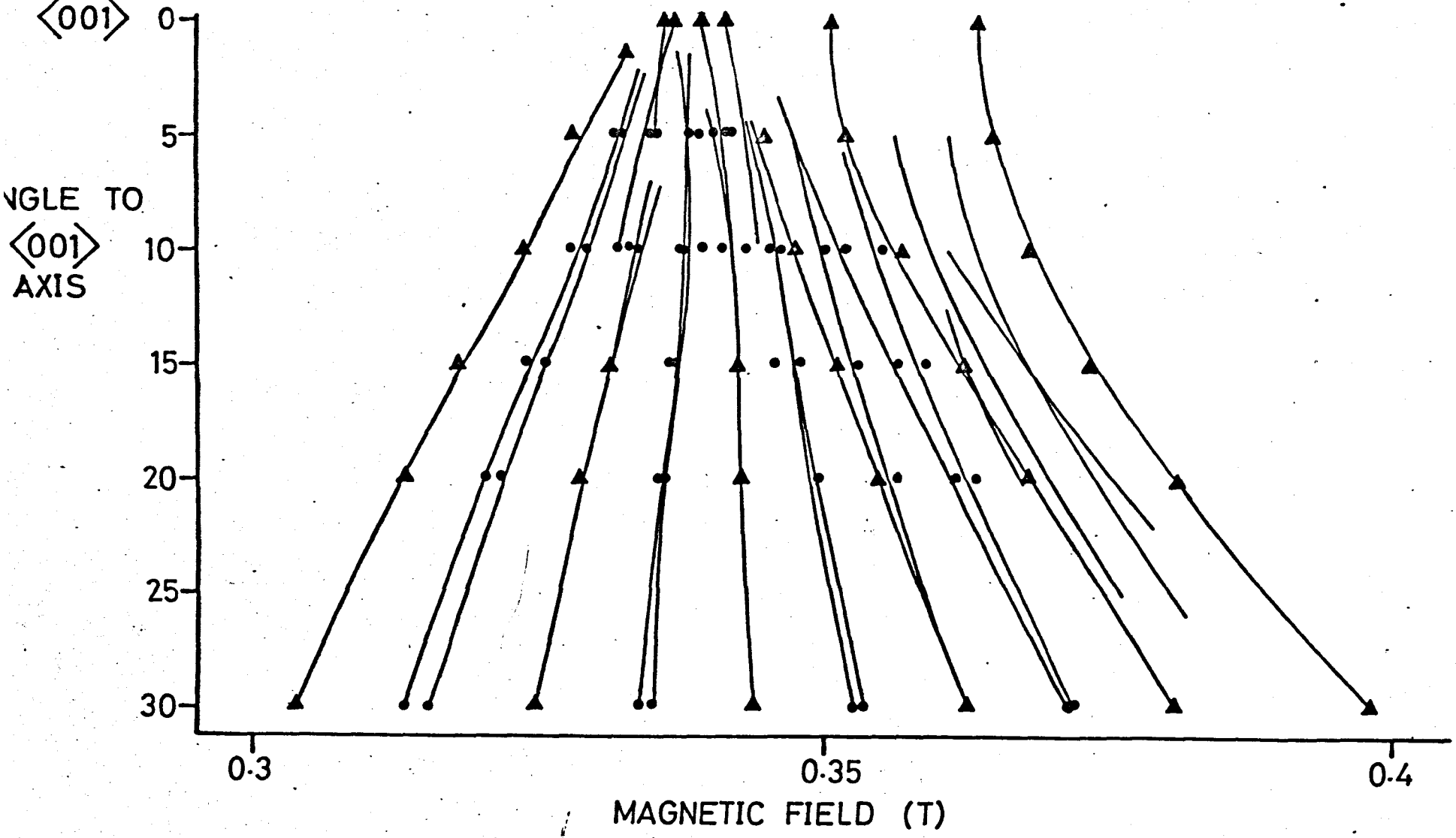

represent transitions which are calculated to be greater than 1/20 th the intensity of the transitions when $\theta = 0^{\circ}$, which are given the relative intensity 1.0. For clarity, those experimental points representing lines with relative intensity less than 1/3 rd. are indicated by dots, whilst those with intensities greater than this are represented by triangles. The overall agreement is good, and within experimental error, although the transitions calculated to occur at higher field were not generally observed. Additional terms in the spin Hamiltonian including the orthorhombic quadrupole interaction and small terms of the form $S.I^3$ and $S.I^5$ may account for this discrepancy, but they have not been investigated in detail. The incorporation of an orthorhombic quadrupole interaction would, however, be unusual in an otherwise axial system. Nevertheless some evidence was obtained for a departure from perfectly axial symmetry from linewidth studies in the ab plane. This would put an upper limit of 0.0002 cm^{-1} on the departure from axial symmetry, since it cannot be larger than the linewidth which essentially determines the experimental error.

Figure 3.10 illustrates precisely the behaviour of the spectrum as the magnetic field direction approaches the crystal c axis. The four low field lines of the six at $\theta = 0^{\circ}$ decay in intensity as θ increases, so that at 10° they have fallen to below 1/20 th of their original intensity. The 'allowed' transitions at $\theta = 15^{\circ}$ grow from what were previously low intensity lines. The most noticeable decrease in intensity occurs for the line to lowest field, which decays from relative intensity 0.5 to zero in less than five degrees. Clearly the crossing of EPR lines which was envisaged to occur at 77 K does not in fact happen, rather 'forbidden' and 'allowed' lines interchange, indicating the danger of using these terms when large hyperfine terms are found.

3.10 ENDOR at 4.2 K

The main advantage of ENDOR in the present studies is that

it allows the nuclear g-values, quadrupole terms and hyperfine parameters of the centre to be determined precisely. Normally precluded in EPR because of experimental inaccuracies, the determination of the nuclear g-value of a nucleus uniquely identifies it. In addition, ENDOR gives the sign of g_N relative to the electronic g-factor, and the sign of the quadrupole term relative to the hyperfine parameters. The measurements here are regarded as a preliminary survey, with the limited objective of measuring the nuclear g-value and so identifying the centre unequivocally. This attitude was determined by experimental limitations in the voltage swept oscillator of the ENDOR spectrometer, which confines measurements to nuclei with transitions in the range 0 - 110 MHz. A preliminary calculation showed that only for the low field EPR transitions near $\theta = 0^{\circ}$ would all the ENDOR lines be observable. This is just the region in which the overlapping lines allow cross - relaxation effects to "switch on" unexpected ENDOR transitions. Such effects have been observed quite frequently in the ENDOR spectra of defects (O'Mara, Davies and Wertz,1969, Henderson, Kolopus and Unruh, 1971, Unruh, Chen and Abraham,1973). Cross relaxation paths also result in nuclear spin-polarization which gives rise to lines of inverted phase. Furthermore a distorted r.f. waveform can result in the second harmonic of a particular frequency having sufficient power to excite an ENDOR transition: it is therefore observed at half the expected frequency. These experimental difficulties are fairly common in ENDOR, but they must be guarded against carefully. To avoid any ambiguity a computer calculation of all the possible ENDOR transitions for a given set of parameters was undertaken, in which provision was made for the stepwise variation of several of them. This procedure was adopted in place of the usual approach, which involves calculation of the parameters from the ENDOR spectrum, for two further reasons. Firstly the absence of some of the ENDOR transitions from the high field EPR

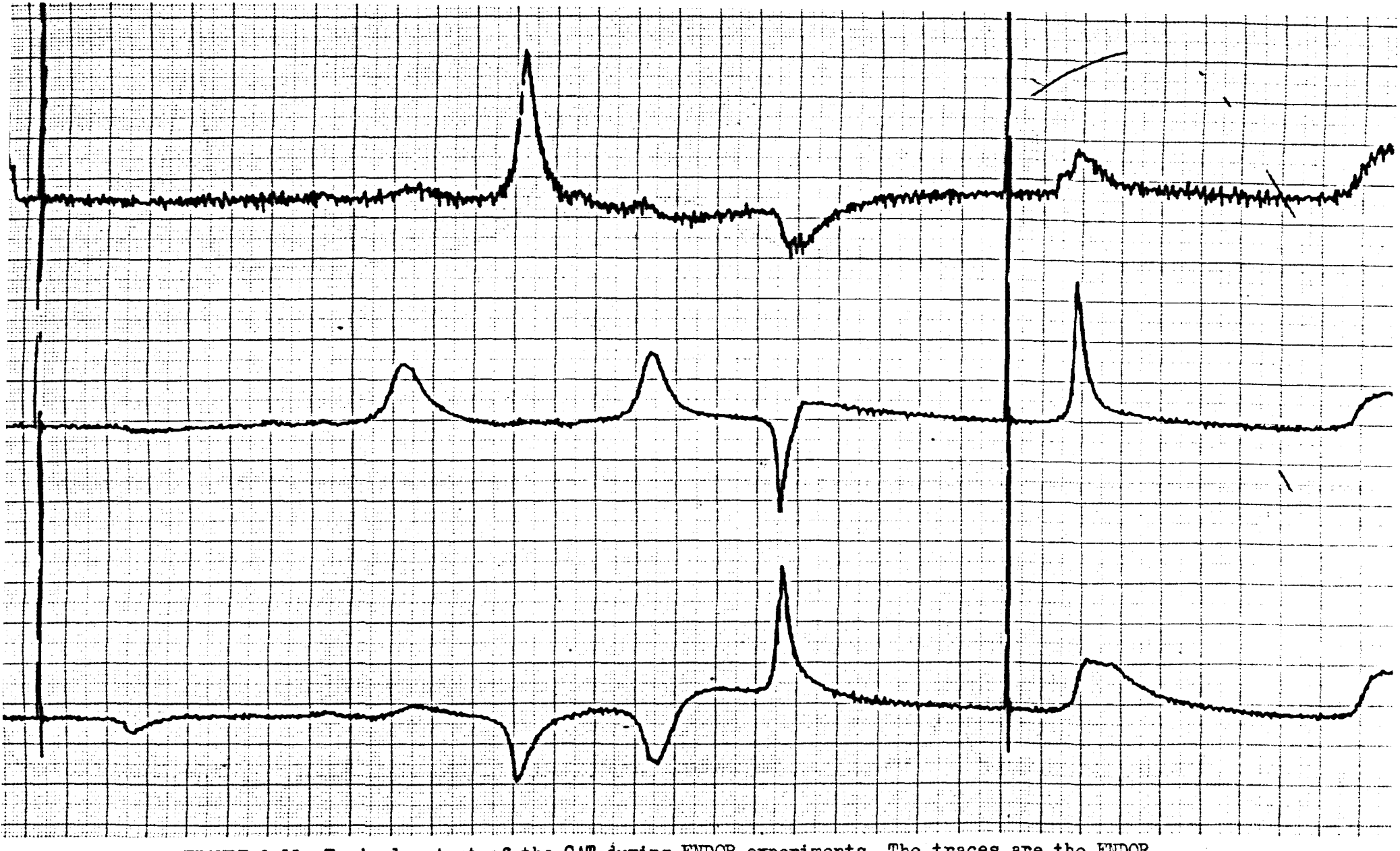

FIGURE 3.11 Typical output of the CAT during ENDOR experiments. The traces are the ENDOR signals from the three low field EPR lines when $\underline{B} \| c$, at 4.2 K; note the recurring pattern of lines and the changes of phase. Vertical lines on the extreeme left, and right of centre are frequency markers.

TABLE 3.3

Summary of ENDOR Results at 4.2 K

EPR line	Observed Frequency (MHz)	Calculated Frequency (MHz)	Identifying quantum numbers of the Endor transitions *		
0.3361 T	46.5	45.64	$-\frac{1}{2}$	3/2	5/2
	56.7	55.23	$\frac{1}{2}$	3/2	1/2
	66.7	65.87	$-\frac{1}{2}$	1/2	3/2
	87.9				
		124.48	$\frac{1}{2}$	5/2	3/2
0.3367 T	38.0	38.18	$\frac{1}{2}$	1/2	-1/2
	55.9	55.12	$\frac{1}{2}$	1/2	3/2
	66.3	65.93	$-\frac{1}{2}$	1/2	3/2
	88.1	88.42	$-\frac{1}{2}$	1/2	-1/2
0.3393 T	47.1	46.34	$-\frac{1}{2}$	3/2	5/2
	67.7 (x2 = 135.4)	123.32	$\frac{1}{2}$	5/2	3/2
	89.2				
0.3417 T	16.7				
	38.1	38.50	$\frac{1}{2}$	1/2	-1/2
		88.24	$-\frac{1}{2}$	1/2	-1/2
	109.0	108.61	$\frac{1}{2}$	-1/2	-3/2
		113.59	$-\frac{1}{2}$	-3/2	-1/2
0.3507 T	69.4 (x2 = 138.8)	141.45	$-\frac{1}{2}$	-5/2	-3/2
	93.6 (x2 = 187.2)	190.18	$\frac{1}{2}$	-5/2	-3/2
	108.5	108.26	$\frac{1}{2}$	-1/2	-3/2
		111.90	$-\frac{1}{2}$	-1/2	-3/2
0.3636 T	67.2 (x2 = 134.4)	136.80	$-\frac{1}{2}$	-3/2	-5/2
	94.1 (x2 = 188.2)	187.60	$\frac{1}{2}$	-3/2	-5/2

* The first column is the M_S quantum number of the levels involved, and the second two numbers are the M_I quantum numbers.

lines made the observed spectrum more difficult to interpret; the pattern of repeated ENDOR lines and their small movement on going from one EPR transition to the next greatly simplifies their identification. Secondly it was somewhat easier to incorporate the effects of crystal misorientation.

Figure 3.11 shows three typical ENDOR traces for the low field lines when $\underline{B}$ was directed along the c axis. The traces are the output of the Signal Averager after ~ 250 sweeps of the whole r.f. range in 25 seconds. Apart from the recurring pattern of lines the other noticeable feature is the change in phase of some of the lines. A comparison of the experimental and calculated ENDOR frequencies is given in Table 3.3, together with the magnetic field positions at which they were observed and their identifying quantum numbers. The calculated frequencies were obtained after allowing for a 1° mis - orientation of the crystal using the following parameters:

$$g_{\parallel} = 1.8549$$

$$g_{\perp} = 1.7164$$

$$A_{\parallel} = 0.0042 \ cm^{-1}$$

$$A_{\perp} = 0.0324 \ cm^{-1}$$

$$P_{\parallel} = -0.00048 \ cm^{-1}$$

$$g_N = 1.27 \ .$$

Several points should be made about the results in Table 3.3. The ENDOR lines at 87.9 MHz. (0.3361 T EPR line) and 89.2 MHz. (0.3393 T line) do not correlate with calculated frequencies: they are apparently $M_s = \frac{1}{2}$, $M_I = \frac{1}{2} \leftrightarrow -\frac{1}{2}$ transitions observed as a result of cross relaxation. The transition observed at 16.7 MHz when saturating the 0.3417 T EPR line was not accounted for, and the calculated transition at 88.24 MHz from this EPR line was not observed. Furthermore, several of the ENDOR lines are accounted for only in terms of harmonic generation by the r.f. power amplifier, since they occur at

approximately half the calculated frequency. In these cases there was an obvious correlation between the input level to the power amplifier, the distortion of the output from the power amplifier and the relative intensities of the ENDOR transitions.

The spin Hamiltonian parameters derived from the ENDOR and EPR experiments are in good accord, although the quadrupole term derived from the ENDOR study is rather smaller than that obtained from the EPR results. However, the most satisfying feature of the ENDOR results is the nuclear g-value, which vindicates completely the assertion that Re^{187} is the nucleus involved. Ideally the ENDOR experiments should be repeated as a function of orientation in the ac plane. This would resolve the problem associated with the magnitude of the quadrupole interaction and allow a thorough investigation of the large number of forbidden transitions observed. This, however, would require a broad band power amplifier and swept oscillator which operated to $\sim$ 1 GHz. These facilities are outside the range currently available in most research laboratories.

3.11 Linewidth variation of the spectrum

3.11.1 Variation with temperature

The spectrum was not detected at 300 K, but at 77 K the six lines were easily observed with a linewidth of $\sim$ 1.5 mT. At 90 K, however, the linewidth had increased to $\sim$ 2.0 mT, and at 120 K the linewidth was so large that the spectrum was no longer visible. When the spectrum was observed at 4.2 K the linewidth was decreased by a factor of 5 relative to that at 77 K, and at the lower temperature the spectrum saturated readily, approximately 60 dB attenuation ($\sim$ 0.1 μW power) being required for unsaturated observation. The explanation for the violent behaviour of the linewidth with temperature lies in lifetime broadening, the efficiency of the relaxation processes of the levels increasing rapidly with temperature.

Using Eq.1.56 we can estimate that at $\sim$80 K, the relaxation time T_1 is $\sim 10^{-9}$ secs. The deviation of the g-value correlates with this interpretation, as fast relaxation is generally associated with a large orbital contribution to the magnetism. In preliminary investigations the relaxation time was found to be $\sim$2 seconds at 4.2 K, too long to be measured accurately with the modified pulse saturation recovery apparatus available in the laboratory, and it had a strong angular dependence. It seems likely that at 4.2 K relaxation proceeds by a direct process involving the hyperfine structure, with T_1 inversely proportional to the absolute temperature. At temperatures slightly above this a two phonon Raman process probably takes over, with $T_1 \propto T^{-9}$, continuing to higher temperatures.

3.11.2 Variation in the ab plane

It is commonly found that the width of paramagnetic resonance lines cannot be reduced indefinitely by decreasing the concentration of magnetic ions in the crystal. Residual width at high dilutions can occasionally be attributed to the local magnetic fields generated by randomly distributed nuclei, strain, or mosaic structure in the crystal. Additionally Mims and Gillen (1966), hereafter referred to as MG, have shown that inhomogeneous line broadening can be caused by the electric fields generated inside a crystal by randomly distributed charged defects. If the paramagnetic ion is in an environment which lacks inversion symmetry, as in the case of Re^{6+} in $CaWO_4$ (the atom is assumed to be at the same site as the parent W atom), these electric fields give rise to proportional shifts in frequency which can be the most important factor in determining the width and shape of the resonance lines.

Illustrated in Fig.3.12 is the variation in width of the low field line of Re^{6+} for magnetic field rotations in the ab plane. The

FIGURE 3.12 Linewidth variation of the low field EPR line for B in the ab plane.

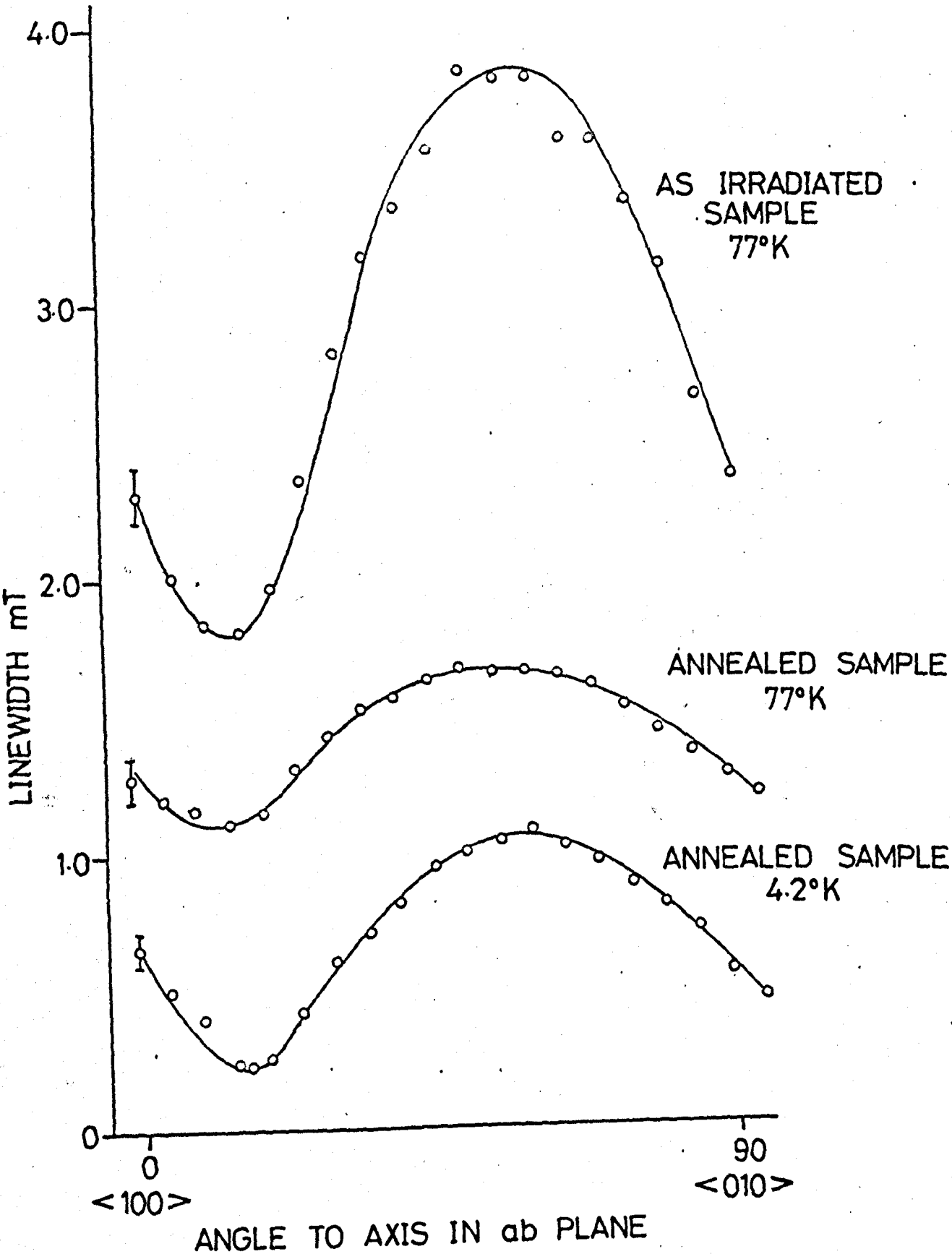

measurements at 77 K provide evidence for broadening due to the effects of both electric fields due to charged defects and elastic strain due to these and other defects, both of which decrease on annealing. However, the dramatic decrease in the number of charged defects following the high temperature anneal, suggests that electric field broadening made a significant contribution to the larger width of the lines in the as-irradiated sample. This is reinforced by the slight, rather than drastic, simplification in the strain pattern of a piece of $CaWO_4$ crystal viewed on a polarizing microscope before and after annealing. Unfortunately the residual lifetime width of the lines makes the true linewidth change difficult to estimate. This residual width is probably the reason why the ratio of maximum to minimum linewidth is less for the annealed sample. For this sample the low width limit is more determined by lifetime broadening than in the un-annealed sample, for which the dominant contribution comes from electric field and strain effects.

MG have investigated the effects of applied electric fields on the EPR of ions in $CaWO_4$ in some detail. Figure 3.13b gives an example of their results, comparing the variation in linewidth of the $M_s = 5/2 \leftrightarrow 3/2$ transition of Mn^{2+} ions as the magnetic field was rotated in the ab plane with the shift in line position of the same line in an electric field of 2500 kV m^{-1} applied along the c axis. Similar results were observed for other paramagnetic ions in $CaWO_4$, and MG concluded that the dominant contribution to the linewidth arises from internal electric fields. By comparison with the data presented in Fig.3.12 it is proposed that this explanation is valid also for the linewidth variation of Re^{6+}. The only discrepancy between the two figures is the position of the linewidth minimum relative to the crystal axes; this is not surprising since MG found

FIGURE 3.13 (a) Maximum and minimum width of the EPR lines of Re^{6+} as a function of magnetic field (annealed sample).

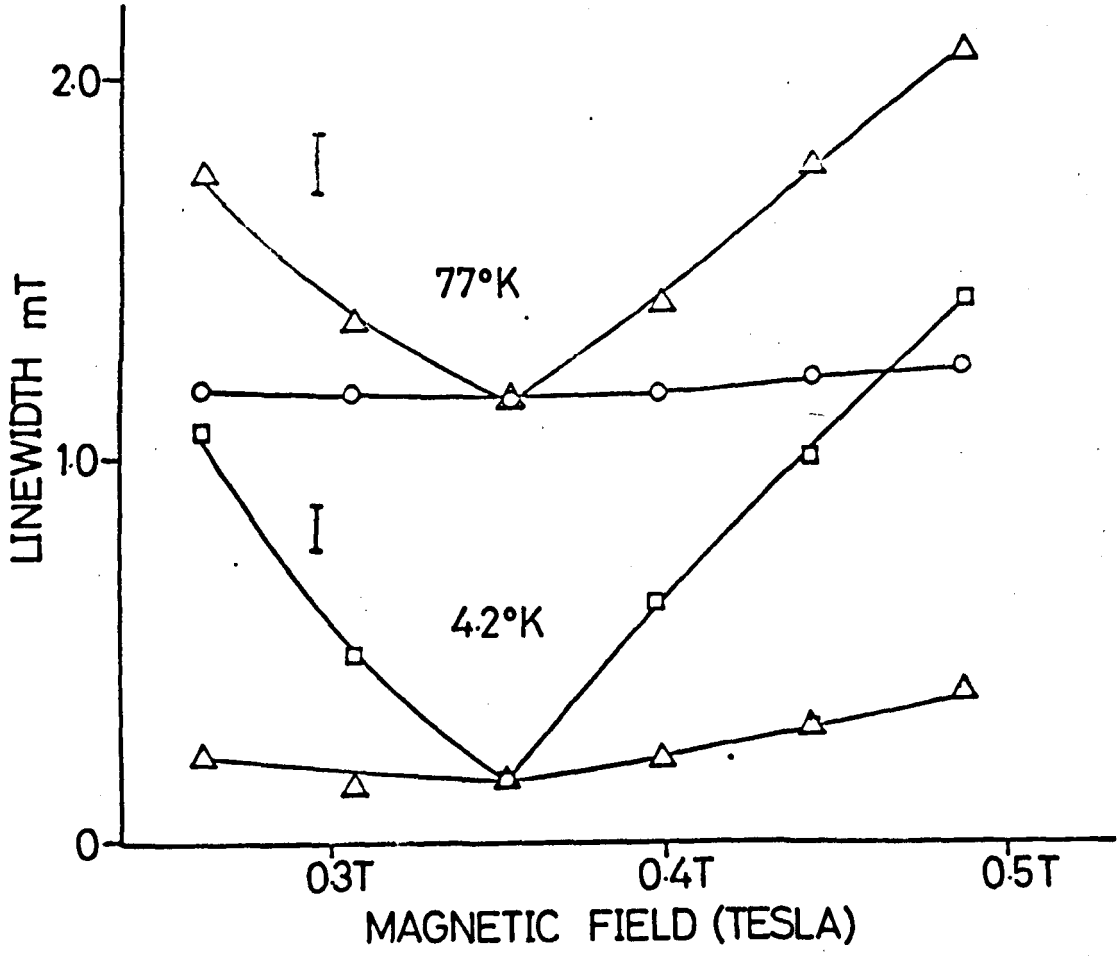

FIGURE 3.13 (b) Linewidth variation of the $M_s = 5/2 \leftrightarrow 3/2$ EPR line of Mn^{2+} in calcium tungstate. After Mims and Gillen (1966).

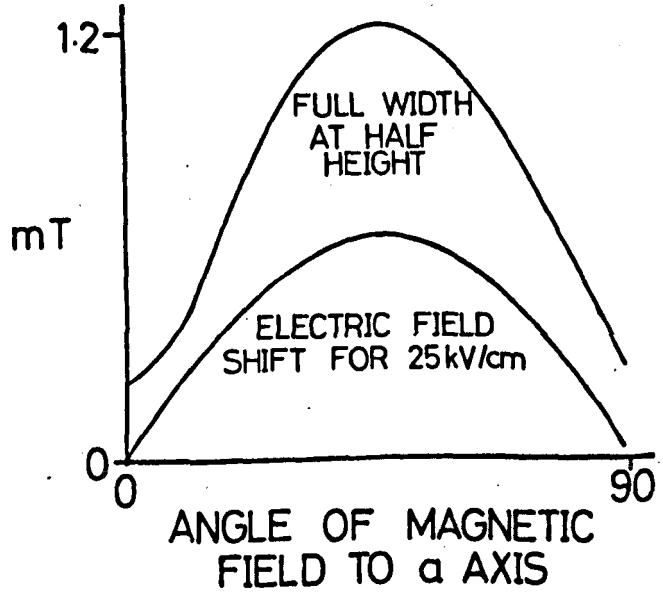

the position of the linewidth minimum to be different for each ion investigated.

MG calculated the lineshape and line broadening effect caused by an internal electric field by summing the electric field shifts due to a random distribution of doubly charged defects using a continuum approximation which ignores the discrete nature of the lattice. They found that the lineshape should be the Fourier transform of an exponential to the -3/2 power, which is intermediate between the Gaussian and Lorentzian lineshape functions. Experimentally the shapes of Re^{6+} lines at both 77 and 4.2 K had this intermediate character. The peak-to-peak width of the differential lineshape for an electric field along the c axis is found to be

$$\Delta\nu = 2.74 \frac{n^{2/3}\, 2e\, c}{4\pi \epsilon_0 \epsilon_z} \qquad 3.13$$

where n is the concentration of defects charge 2e, and c is the electric field shift in frequency units for unit electric field along the c axis of the crystal. ϵ_0 and ϵ_z are the permittivity of free space and of the crystal along $\underline{c}$ respectively. A maximum linewidth of 1.1 mT, corresponding to a frequency width of ~ 30 MHz gives

$$n^{2/3}\, c = 6.4 \times 10^{10} \text{ MHz (Volt-m)}^{-1}$$

A reasonable estimate for c is 5.0×10^{-6} MHz for an electric field of 1 Volt m^{-1}, giving a concentration of doubly charged defects of

$$n \approx 10^{18} \text{ cm}^{-3} \ (= 10^{24} \text{ m}^{-3}). \qquad 3.14$$

This is a typical result, to be compared with the rhenium concentration of $\sim 5 \times 10^{18}$ cm^{-3}. Since there is no charge imbalance between $(ReO_4)^{2-}$ and $(WO_4)^{2-}$, n is regarded as being typical of pure $CaWO_4$. MG point out, however, that their analysis can also be applied to strain induced broadening, in which case the lineshape need not be symmetrical. As distorted lineshapes were observed at some magnetic field orientations in the ab plane, a contribution from strain broadening

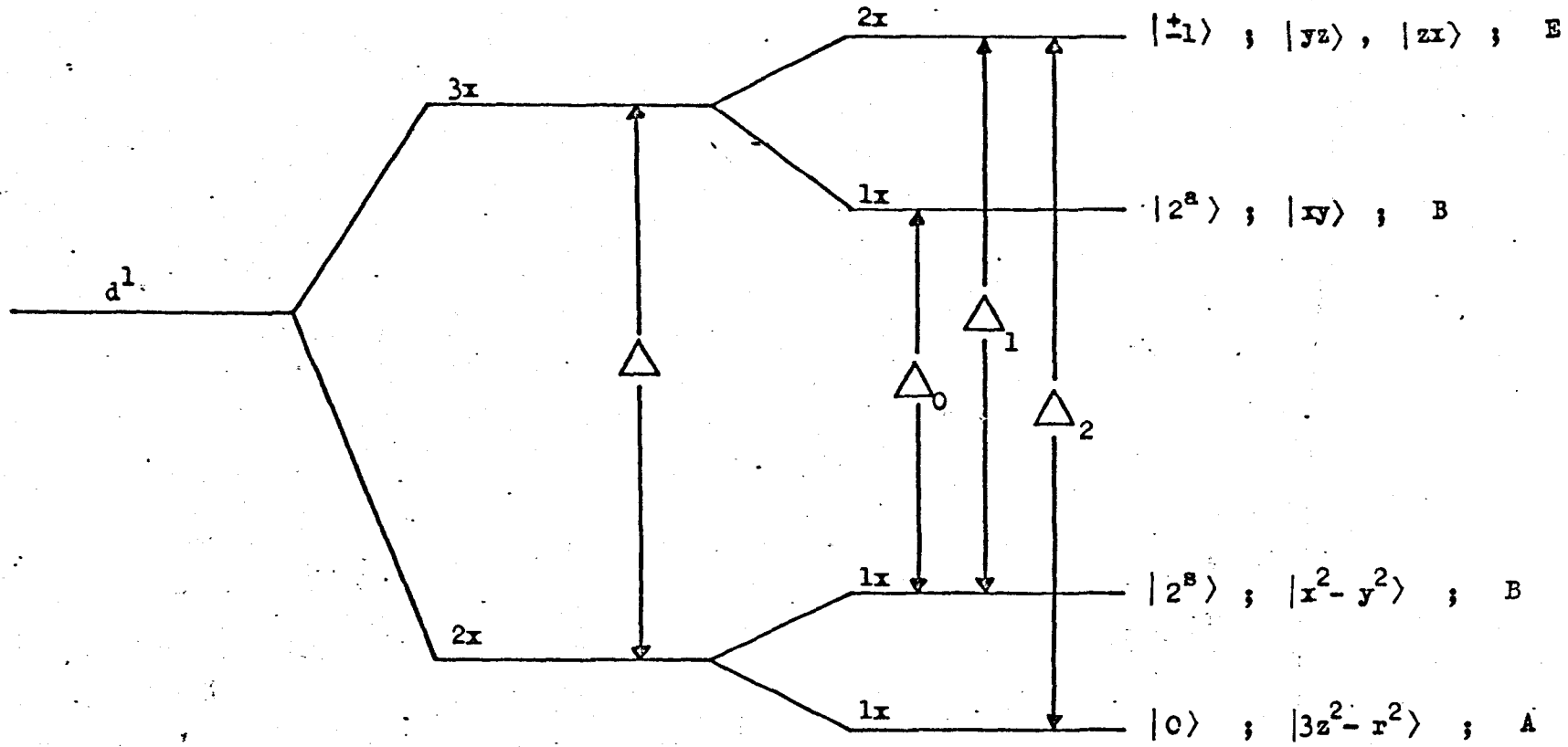

FIGURE 3.14 Orbital energy levels of a d^1 ion in a crystal field of tetrahedral symmetry with a tetragonal distortion.

cannot be ruled out.

Another feature of these results is the linewidth variation with both magnetic field and hyperfine line which is typical of inhomogeneously broadened resonance lines (Stoneham,1969). Figure 3.13a shows the variation with magnetic field of the maximum and minimum linewidth of each line in the annealed sample at both 77 K and 4.2 K. The width of the lines occurring for positive values of M_I is less,by roughly the same amount, than the corresponding line for M_I negative. Furthermore, the linewidth clearly depends on the quantum number M_I.

3.12 Discussion of the spin Hamiltonian parameters

The $5d^1$ electron of Re^{6+} gives rise to a ^2D free ion ground term. As Figure 3.14 illustrates, the ^2D term splits into a triply degenerate T_2 state and a doubly degenerate E state of lower energy in a crystal field of tetrahedral (T_d) symmetry. A compression along one of the two-fold axes reduces the symmetry to S_4, causing the E state to split into states of A and B symmetry. The T_2 state splits into a doubly degenerate E state and a B state. For the present purposes, the critical orbital is the one derived from the tetrahedral E state which has lower energy, since it is this orbital which is occupied by the single electron. Physically the $d_{x^2-y^2}$ orbital is expected to be stabilized by an extension of the tetrahedron, whereas the d_{z^2} orbital would be more stable under compression, since the electron density of the former orbital is concentrated in the plane perpendicular to the axis of the distortion.

Equation 1.35 allows second order expressions to be derived for the g-values expected from the occupation of either the d_{z^2} or $d_{x^2-y^2}$ orbital. For d_{z^2}

$$g_{\parallel} = 2 \qquad 3.18$$

$$g_{\perp} = 2 - \frac{6\lambda}{\Delta_2} \qquad 3.19$$

and for $d_{x^2-y^2}$,

$$g_{\parallel} = 2 - \frac{8\lambda}{\Delta_0} \qquad 3.20$$

$$g_{\perp} = 2 - \frac{2\lambda}{\Delta_1} \ , \qquad 3.21$$

where λ is the spin orbit coupling parameter, and the Δ's are shown in Fig.3.14. Bleaney, Bowers and Pryce (1955) have derived expressions for the hyperfine parameters. For d_{z^2}

$$A_{\parallel} = P\left(-K + \frac{4}{7} + \frac{6}{7}\frac{\lambda}{\Delta_2} \right) \qquad 3.22$$

$$A_{\perp} = P\left(-K - \frac{2}{7} - \frac{45}{7}\frac{\lambda}{\Delta_2} \right) \qquad 3.23$$

whilst for $d_{x^2-y^2}$

$$A_{\parallel} = P\left(-K - \frac{4}{7} - \frac{6}{7}\frac{\lambda}{\Delta_1} - \frac{8\lambda}{\Delta_0} \right) \qquad 3.24$$

$$A_{\perp} = P\left(-K + \frac{2}{7} - \frac{11}{7}\frac{\lambda}{\Delta_2} \right) . \qquad 3.25$$

Here K is a dimensionless constant which measures the contribution of s-configuration 'contact interaction' to the hyperfine structure and

$$P = 2g_N\mu_B\mu_N \left\langle r^{-3} \right\rangle_{av} . \qquad 3.26$$

From these expressions $g_{\parallel} > g_{\perp}$ and $|A_{\parallel}| < |A_{\perp}|$ if d_{z^2} is occupied, but for a $d_{x^2-y^2}$ orbital $g_{\perp} > g_{\parallel}$ and $|A_{\parallel}| > |A_{\perp}|$. Although $g_{\parallel}$ is rather smaller than is predicted by Eq.3.18, the measured spin Hamiltonian parameters indicate that for Re^{6+} in $CaWO_4$ the occupied ground orbital is indeed d_{z^2}. Since an appeal to higher orders in perturbation theory does not improve the interpretation, this conclusion rests on the assumption that the general features of the equations remain valid in a more complex molecular orbital computation, for it is anticipated that the bonding in the $[ReO_4]^{=}$ complex is almost entirely covalent.

The quality of the fit obtained using perturbation theory can be gauged by comparing the value of $\frac{\lambda}{\Delta_2} \approx 0.05$, obtained from the

substitution of $g_\perp = 1.716$ into Eq.3.19, with that implied by the colour of the samples. Untreated $CaWO_4$ crystals are perfectly clear and colourless, whilst the experimental sample was pale green due to a weak absorption band at $\sim 13{,}000\ cm^{-1}$. The commonly accepted value of λ estimated for 5d ions is $\sim 2{,}000 - 3{,}000\ cm^{-1}$ (Abragam and Bleaney, op cit, p.475), indicating that $\frac{\lambda}{\Delta} \sim 0.2$. It seems likely that only a molecular orbital calculation, taking account of the covalency of the complex, will explain the magnitudes of the observed shifts in $g_{||}$ and $g_\perp$. This is because large contributions to the g-shifts can arise from molecular orbitals which are connected to the ground orbital by spin-orbit coupling. Their energy separation from the ground orbital can be smaller than the crystal field splittings indicated by the ionic model.

The isotropic contribution to the hyperfine structure, PK, can be calculated using the above value of $\frac{\lambda}{\Delta_2}$ in Eqs.3.22 and 3.23. At 4.2 K $|PK| = 0.018\ cm^{-1}$ and at 77 K, $0.019\ cm^{-1}$. PK is the contact hyperfine term, which defines the s-character at the nucleus derived from core polarization. The quantity χ is generally introduced as a measure of the density of unpaired electron spin at the nucleus. In atomic units χ is given by

$$K \langle r^{-3} \rangle = -2/3\ \chi \quad . \qquad 3.27$$

The magnetic field at the nucleus can be found from χ since 1 a.u. = 4.21 x 2S Tesla. Generally χ is found to be of opposite sign to the nuclear g-factor (Freeman and Watson,1965), but in the present case the absolute sign of g_N was not determined. Consequently we assign χ negative in common with other results:

$$\chi = -\left| \frac{3\ PK}{4\ g_N\ \mu_N\ \mu_B} \right| \quad . \qquad 3.28$$

Hence, at 4.2 K $\chi = -8.9$ a.u. and at 77 K $\chi = -9.3$ a.u. The negative sign of χ means that the hyperfine fields are antiparallel to the net (spin) magnetic moment on the ion. No calculations of χ have been made

for 5d ions, but Freeman and Watson (1967) report computed values for a number of 4d ions which lie in the range -8 to -9 a.u. i.e. about three times as large as for 3d ions. Unfortunately the absence of theoretical data on the 5d ions precludes further comment on the trends established for 3d, 4d and 5d ions.

The order of magnitude difference between $A_{||}$ and $A_{\perp}$, and the change in $g_{||}$ and $A_{||}$ on cooling the crystal from 77 K to 4.2 K are further interesting features of the results. This can be best considered using an approach which separates the Hamiltonian hyperfine parameters into isotropic and anisotropic components. The axial hyperfine term in Eq.3.1

$$A_{||}S_zI_z + A_{\perp}(S_xI_x + S_yI_y)$$

can be written as the sum of the terms

$$a(S_zI_z + S_xI_x + S_yI_y)$$

and

$$b_1S_zI_z + b_2(S_xI_x + S_yI_y)$$

where a represents the isotropic hyperfine interaction and the b's the anisotropic contributions, provided

$$A_{||} = a + b_1$$

and

$$A_{\perp} = a + b_2 .$$

Using the condition that the anisotropic part can have zero trace without altering the resonance results we find that

$$a = \frac{A_{||} + 2A_{\perp}}{3} \qquad 3.29$$

and

$$b_2 = \frac{A_{\perp} - A_{||}}{3} . \qquad 3.30$$

At 4.2 K $a = 230 \times 10^{-4}$ cm^{-1} and $b_2 = 94 \times 10^{-4}$ cm^{-1}, indicating that the order of magnitude difference between $A_{||}$ and $A_{\perp}$ arises from the unusually large anisotropic contribution to the overall hyperfine

TABLE 3.5

Spin Hamiltonian parameters of nd^1 ions situated on the tungsten site in $CaWO_4$.

Ion	$g_{\parallel}$	$g_{\perp}$	$A_{\parallel}$ $(10^{-4}cm^{-1})$	$A_{\perp}$	Temperature °K	Reference
Cr^{5+}	1.988	1.943	4	23	4.2	Lingam et al (1969)
Cr^{5+}	1.989	1.945	3.5	23	23.0	Kedzie et al (1964)
$^{95}Mo^{5+}$	1.987	1.887	8.39	41.18	4.2	Azarbayejani & Merlo (1965)
$^{97}Mo^{5+}$	1.987	1.887	8.64	42.52	4.2	Azarbayejani & Merlo (1965)
$^{183}W^{5+}$	1.850	1.587 g_x 1.60 g_y	19.05	53 A_x 66 A_y	4.2	Azabayejani, Chu & Kikuchi, (1965)
$^{187}Re^{6+}$	1.8549	1.7164	42.0	324.0	4.2	This work
$^{185}Re^{6+}$	1.8549	1.7167	42.0	321.0	4.2	This work
$^{187}Re^{6+}$	1.8491	1.7162	30.0	331.0	77 K	This work

interaction. At 77 K $a = 231 \times 10^{-4}$ cm^{-1} and $b_2 = 100 \times 10^{-4}$ cm^{-1}, showing that the large change in $A_{||}$ on cooling really reflects a much smaller relative change in the anisotropic hyperfine interaction. Whilst $g_{\perp}$ and $A_{\perp}$ change little on cooling, $g_{||}$ changes by 0.006 in concert with $A_{||}$. In the absence of accurate data on the variation of the lattice parameters of $CaWO_4$ on cooling it is difficult to comment on this, except that these results might indicate a greater degree of contraction along the crystal c axis. They may also indicate, however, that $A_{||}$ and $g_{||}$ are more sensitive to the contraction, by a mechanism which the simple ionic model fails to take account of.

Table 3.5 lists the spin Hamiltonian parameters of the nd^1 ions Cr^{5+}, Mo^{5+} and Re^{6+} which have been observed in $CaWO_4$ using EPR. The most noticeable feature of these results is the closeness of the g-values of Cr^{5+} and Mo^{5+} to the free spin value, compared with the large departures of those of W^{5+} and Re^{6+}. The properties of the two lighter ions can be satisfactorily explained in terms of the ionic approach outlined above. Clearly this cannot be the case for W^{5+} and Re^{6+}. The major change in the parameters indicates that there are additional contributions to the g-shift (and hyperfine structure) of ions in the $[MO_4]^-$ complex in $CaWO_4$ on going from the second to third series of transition elements. Generally the large change in properties between ions in the same group in the periodic table occurs between the first and second series, and it is explained in terms of the change in ionic size. This explanation cannot apply in the present case as Mo^{5+}, W^{5+} and Re^{6+} have roughly the same ionic radius (Cotton and Wilkinson,1966). Clearly detailed interpretation of the results reported here awaits extension of the theory of nd^1 ions to the case of $5d^1$ ions in covalent tetrahedral and distorted tetrahedral sites.

3.13 Concluding remarks

The unique way in which Re^{6+} was generated in the $CaWO_4$ lattice allows some general points to be made about the use of neutron induced nuclear reactions to produce novel paramagnetic centres:

(i) the diamagnetic crystal must be pure, and contain few other paramagnetic centres.

(ii) the crystal should contain only one kind of nucleus which will capture neutrons easily. Generally this means that the crystal must have only one 'heavy' element in its chemical formula.

(iii) the radioactive intermediate must have an uncomplicated decay pattern, with a reasonably short half life.

(iv) the crystal should be able to withstand the high temperatures needed to anneal out lattice defects caused by fast neutrons.

If the paramagnetic species can be incorporated into the lattice by conventional crystal growing techniques no real advantage is gained, except that it may be possible to study just one isotope if there are several which would normally interfere with each other. In the case of rhenium, which is an unusual element to study using EPR, it would almost be impossible to grow $CaWO_4$ crystals containing the element in the 6+ valence state, as this is the least stable of all its common valence states. Some Re^{6+} compounds have been prepared, but they are generally unstable, and in common with the results reported here they have magnetic moments lower than the spin-only value (Cotton and Wilkinson, op cit).

The generation of rhenium from tungsten opens up a large number of possibilities for studying the element in different environments using EPR e.g. Re^{6+} in both the scheelites and monoclinic tungstates. Apart from a thorough EPR study, detailed ENDOR, spin-lattice

relaxation and electric field investigations would also be useful. These last three aspects were not pursued in detail here, and it is in these areas that much useful work on $CaWO_4 : Re^{6+}$ remains to be done.

CHAPTER IV

GADOLINIUM(III) IN CALCIUM OXIDE

4.1 Introduction

The alkaline earth oxide CaO is a dominantly ionic, divalent relative of the alkali halides. It has the face centred cubic structure characterized by rock-salt, with lattice parameter a = 4.797 A. Together with the other alkaline earth oxides, single crystals of CaO have been used in EPR for some time; good quality single crystals of reasonable purity or doped with a selected impurity can be grown by the arc-fusion method. Although the first member of the series, MgO, has received a major share of attention, interest has recently been focused on CaO and the other less stable members of the series. In particular, the effects of the internal electrostatic fields on both paramagnetic impurity ions and the point defects in the crystals have received considerable attention. Currently these crystals are also being used to study the properties of implanted ions, a possible application being radiation dosimetry.

In the alkaline earth oxides, paramagnetic impurity ions are most commonly found substitutionally on cation sites in crystal fields of cubic (O_h) symmetry. Ions in crystal fields of lower symmetry are found when they are either displaced from their normal sites, or associated with a nearby point defect. In general, fewer ions occupy sites of low symmetry, though when the ion requires charge compensation the possibility of a nearby defect is increased.

Gd^{3+} occupies a unique position in the lanthanide series of elements because the $4f^n$ electronic configuration is half full. The 4f electrons in this series exhibit, to first approximation, Russell - Saunders coupling, giving a free ion ground state for Gd^{3+} of $^8S_{7/2}$. However, this is not an accurate representation of Gd^{3+} substituted in

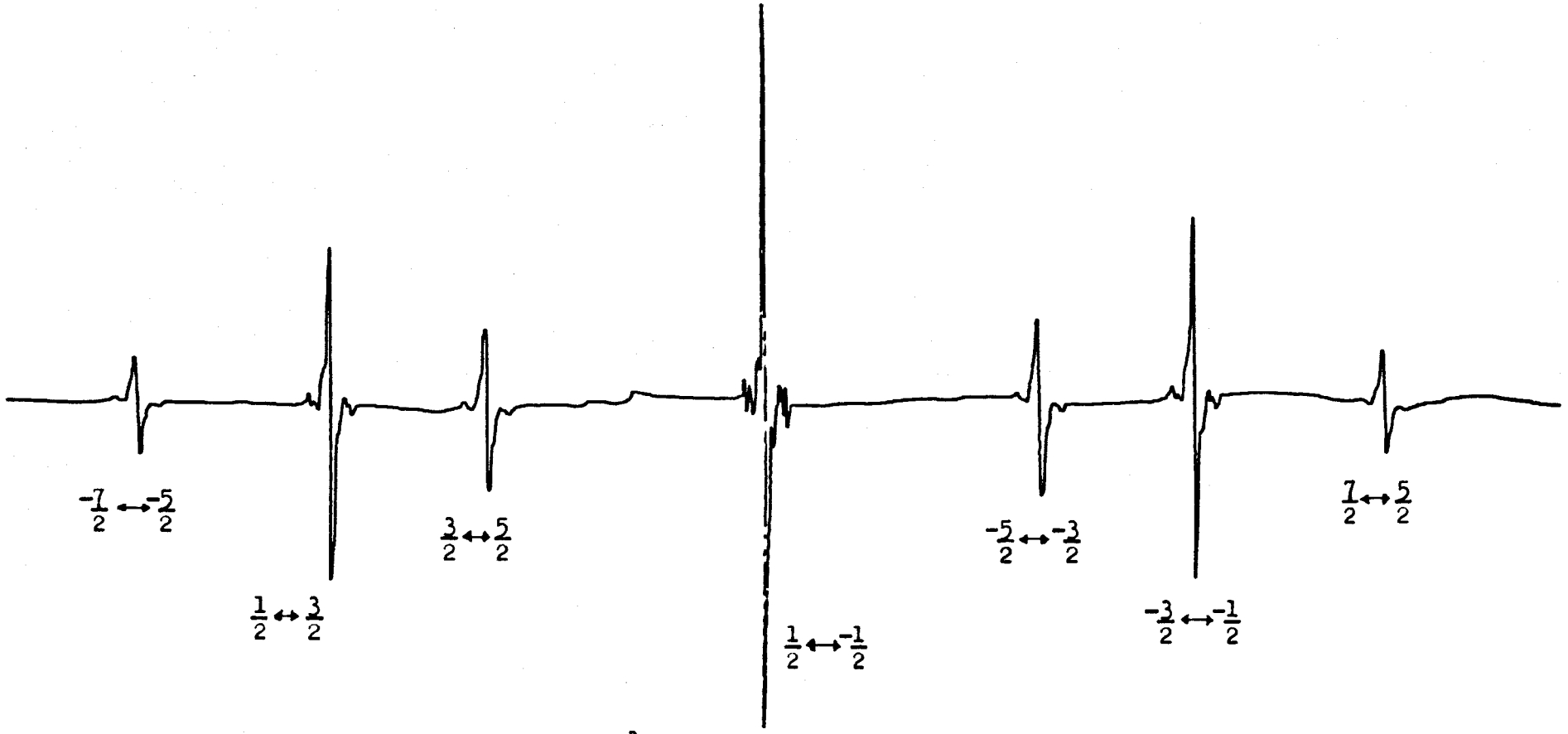

FIGURE 4.1 Cubic Gd^{3+} spectrum with $\underline{B} \parallel \langle 100 \rangle$. Note the hyperfine structure on the central line.

a diamagnetic host lattice, since it explains neither the g-shift from the anticipated free electron value ($g_e = 2.0023$) nor the partial lifting of the eight-fold spin degeneracy by the crystal field. Both of these effects are manifest in magnetic resonance and optical experiments. It is therefore interesting to study the ground state splittings of such S-state ions, in the hope that a large body of experimental results will indicate the areas which need further theoretical attention.

4.2 Preliminary experimental survey

The crystals used in this investigation were supplied by Dr.A.E.Hughes of UKAEA, Harwell. They were colourless but slightly cloudy in appearance, probably due to the presence of voids and precipitates. At room temperature the dominant feature in the EPR spectrum was the seven line spectrum due to octahedral Gd^{3+}. When the magnetic field was directed along a $\langle 100 \rangle$ crystal axis the lines were spread over a range of ~ 50 mT centred on $g \sim 2.0$ (Fig.4.1). These lines were easily identified by the characteristic hyperfine structure of Gd^{155} and Gd^{157}, each of which has nuclear spin $I = 3/2$ (Henderson and Tomlinson,1969). Their natural abundances are 14.7% and 15.6% respectively, and all the other gadolinium isotopes have zero nuclear spin. The Gd^{3+} concentration in the crystals was estimated to be $\sim$ 30 ppm (0.003 atom %) by comparing the intensity of this EPR spectrum with a standard sample of pitch in chalk.

Octahedral Gd^{3+} in CaO is well known, having been first reported by Shuskus (1962). As an independent check on earlier work, the orientation dependence of this spectrum was measured in a $\{100\}$ plane at both room temperature and 77 K. The measured fields were fitted by computer to the cubic symmetry form of equation 1.52 for $S = 7/2$, ignoring the hyperfine structure:

$$\mathcal{H} = g \mu_B \underline{B}.\underline{S} + B_4(O_4^0 + 5O_4^4) + B_6(O_6^0 - 21O_6^4). \qquad 4.1$$

The computer program MNES was modified by the author to include sixth order

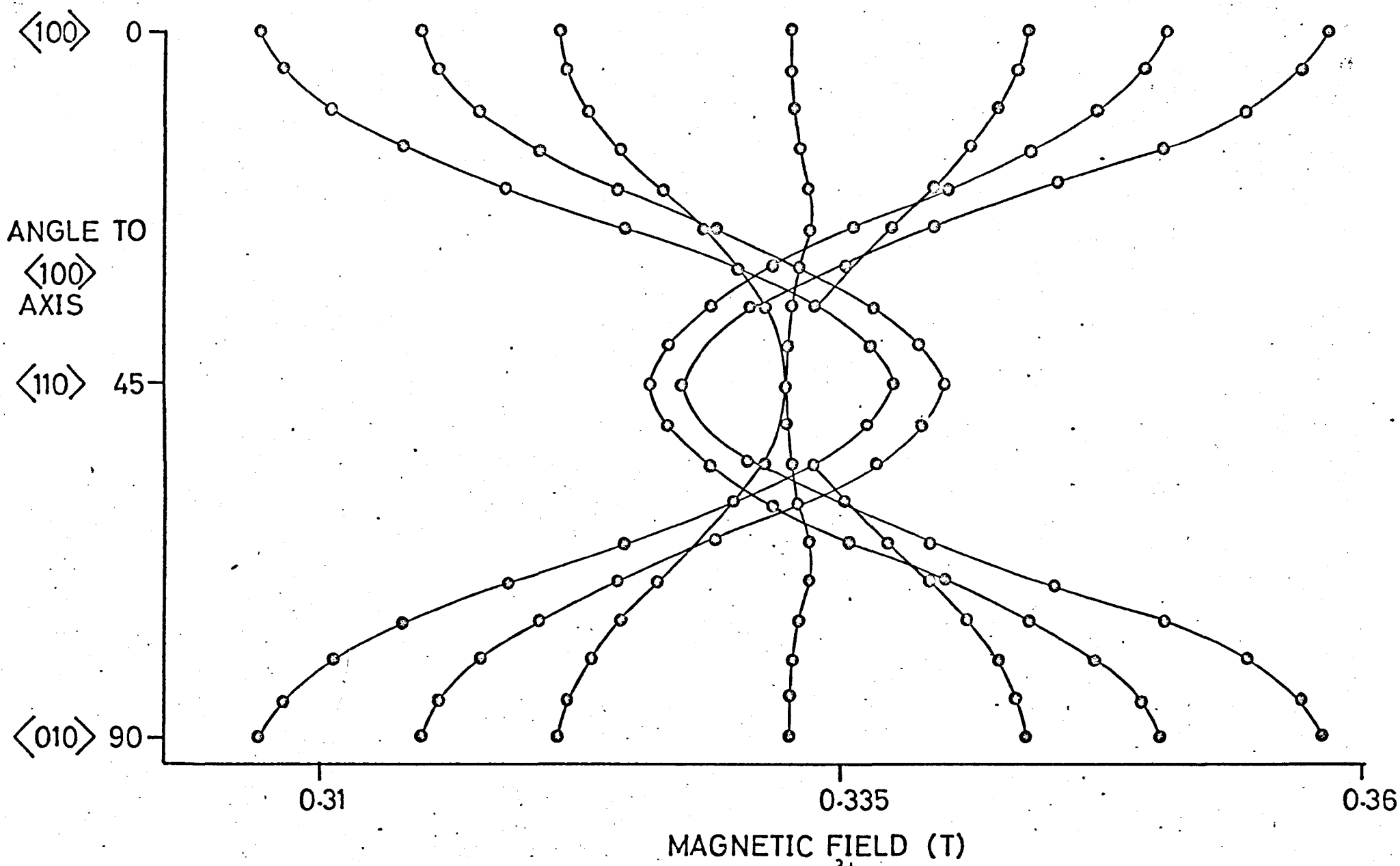

FIGURE 4.2 Angular variation of cubic Gd^{3+} at room temperature for $\underline{B}$ in a {100} plane.

crystal field terms and 8x8 spin matrices. The resulting fit to the room temperature data is shown as a function of orientation in Fig.4.2, when the mean deviation of calculated line position from experimental value was ~ 0.2 mT. At 77 K it was ~ 0.4 mT. The results, quoted in terms of the parameters $b_4 = 60B_4$ and $b_6 = 1260B_6$, are compared with those of Shuskus in Table 4.1.

Only the relative signs of the crystal field parameters can be obtained from the angular variation of the spectrum. The relative change in intensity of the outer lines at 4.2 and 1.6 K allows the absolute sign of b_4 to be determined. If $b_4 < 0$ the transition between the high energy $M_s = 7/2$ and $M_s = 5/2$ levels occurs at high field, whilst the transition between the low energy $M_s = -5/2, -7/2$ levels occurs at low field. If $b_4 > 0$ the former transition occurs at low field and the latter at high field. The mean difference in energy between the two pairs of levels is $6h\nu$, and at temperatures such that $kT < h\nu$, depopulation of the upper levels will occur according to Boltzmann statistics. The sign of b_4 is determined by noting which EPR transition decreases in intensity. Experimentally the low field line was more intense by a factor of 2:1 at 4.2 K and by 8:1 at 1.6 K, indicating that b_4 is negative. This result confirms the second assignment made by Shuskus (see Buckmaster and Shing,1972) and allows the transitions in Fig.4.1 to be unambiguously identified.

The few other lines observed at room temperature in addition to the cubic Gd^{3+} spectrum indicated the high purity of the crystals. Additional lines were observed at 77 K when the maximum available klystron power (100 mW) was incident on the cavity. Under these conditions the Gd^{3+} lines, which begin to saturate at ~ 30 mW power, are much decreased in intensity. One previously obscured spectrum, consisting of five lines centred on $g \sim 2.0$, was easily shown to be due to Fe^{3+} in cubic sites (Low and Rubins,1963). Several axially symmetric spectra from centres with $S = \frac{1}{2}$, $g_{\parallel} \simeq 2.00$ and $g_{\perp} \simeq 2.07$ confirmed the presence of trapped hole centres in the samples.

TABLE 4.1

Spin Hamiltonian Parameters for
cubic Gd^{3+} in calcium oxide

Temperature ^{o}K	g	b_4 $(10^{-4}cm^{-1})$	$b_6(10^{-4}cm^{-1})$	Reference
290	1.9913 ± 0.0005	-11.6 ± 0.1	1.15 ± 0.1	Shuskus(1962)
290	1.9918 ± 0.0002	-11.6 ± 0.3	1.07 ± 0.3	This work
77	1.9908 ± 0.0005	-12.1 ± 0.1	1.16 ± 0.1	Shuskus(1962)
77	1.9915 ± 0.0002	-12.2 ± 0.3	1.35 ± 0.3	This work

Three such centres, V_F, V_{OH} and V^- (see Henderson and Wertz,1968 and Hughes and Henderson,1972 and references therein) have been reported in the literature, but the differences in the g-values of various workers (Shuskus,1963, Unruh, Chen and Abraham,1973, Schrimer,1970 and O'Mara and Wertz,1970) made the unambiguous assignment of lines impossible. Other weak spectra near $g \sim 2.0$ were present but could not be examined in detail because of the nearby, incompletely saturated, Gd^{3+} resonances.

Two sets of lines which were just observed at room temperature were easier to study at 77 K. One group was centred near 0.167 T (half field for $g = 2.0$). The positions and intensities of these lines varied with orientation, and when the magnetic field was directed along ⟨100⟩ or ⟨110⟩ axes they were impossible to detect. These lines were investigated in detail; the results are presented in section 4.3. Groups of lines centred at ~0.185 T, ~0.23 T and ~0.78 T of roughly equal intensity were observed to be critically sensitive to the orientation of the crystal in the magnetic field. They were too weak at 77 K to be observed on the oscilloscope, which made a careful study of them difficult. Their sensitivity to misorientation suggested that an ion in a low symmetry site was involved, Gd^{3+} being most probable. Consequently one of the crystals was annealed at 1200 °C for 24 hours, this treatment being known to enhance the spectra of low symmetry trivalent ions in the alkaline earth oxides (Wertz and Auzins,1957,1967, Henderson et al,1971). The results of the study of these lines in the annealed sample are presented in section 4.4.

4.3 Forbidden Transitions in the octahedral Gd^{3+} spectrum

Electronic transitions for which the spin quantum number changes by more than one are well known in the spectra of transition metal ions in oxide crystals (Henderson and Wertz,1968). In general they are observed at magnetic fields reduced by a factor $\frac{1}{\Delta M_s}$ relative to $B_o = \frac{h\nu}{g\mu_B}$, with small transition probabilities which are sensitive to the orientation of

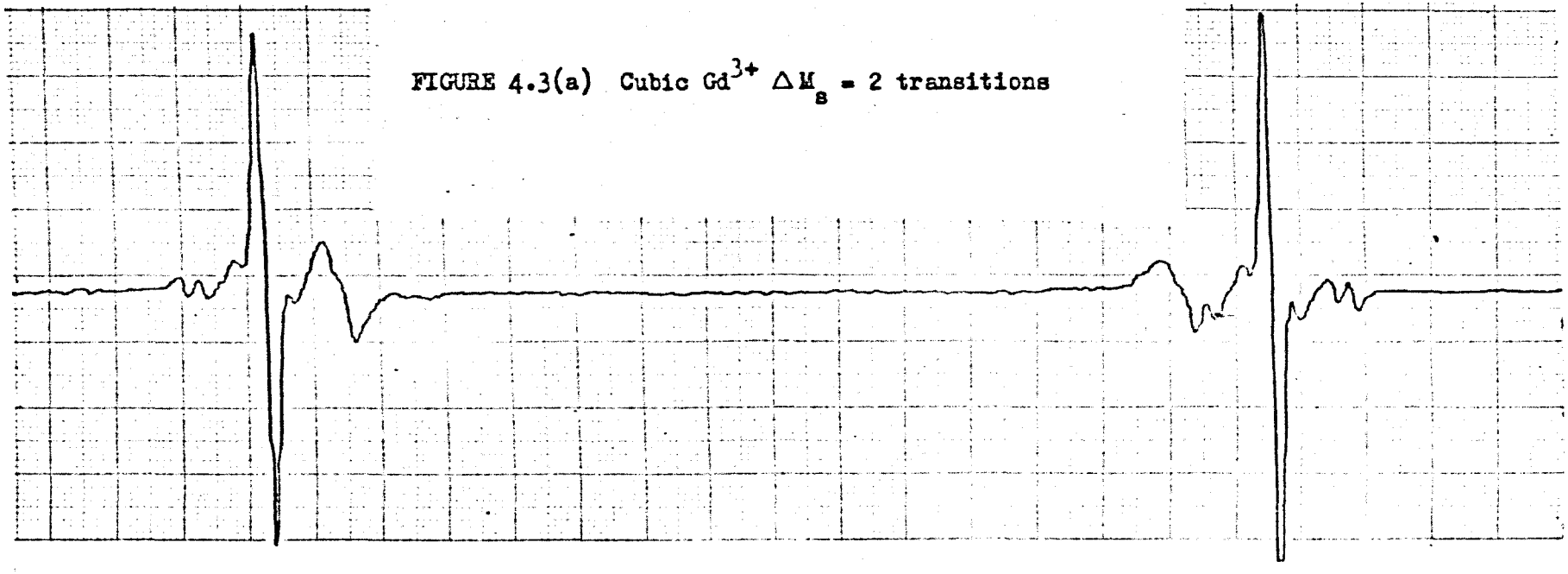

FIGURE 4.3(a) Cubic Gd^{3+} $\Delta M_s = 2$ transitions

FIGURE 4.3(b) Cubic Gd^{3+} $\Delta M_s = 3,4$ transitions. The above transitions would be about five times larger at the same gain.

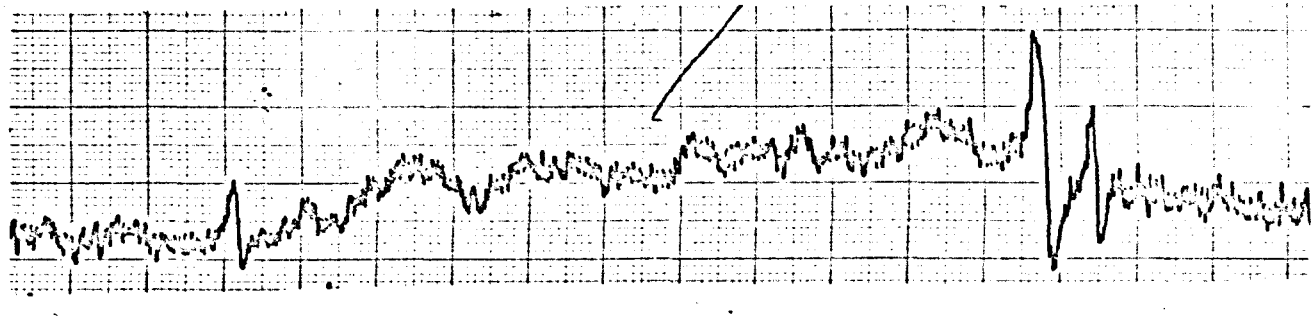

both static and oscillatory magnetic fields. In our experiments the $\Delta M_s = 2$ transitions of Gd^{3+} in O_h symmetry were observed first. A typical recording of these transitions is shown in Fig.4.3a, the hyperfine structure indicating the involvement of gadolinium nuclei. In order to assign these transitions, a computer program was written which calculated the transition probabilities and resonance fields of the 28 possible transitions of an eight level spin system at any orientation of the crystal in a magnetic field. The input parameters were the 77 K spin Hamiltonian parameters tabulated in Table 4.1. The results of this calculation indicated that some of the $\Delta M_s = 3$, 4 and 5 transitions should be detectable. These transitions, which were found at the appropriate magnetic field positions, are portrayed in Fig.4.3b. At the same detector level the peak-to-peak height of the $\Delta M_s = 2$ transitions would be $\sim$30 cm. Figure 4.4 represents a comparison between computed and measured forbidden spectra for a rotation of the magnetic field in a $\{100\}$ plane. Note that (i) the $\Delta M_s = 4$ transitions were observed only at $\theta = 30^\circ$ and 60°, and the $\Delta M_s = 5$ transitions at $\theta = 0^\circ$, (ii) the $\Delta M_s = 2$ and 4 transitions were not observed at $\theta = 0^\circ$ or 45°, (iii) an interfering resonance obscured the high field $\Delta M_s = 3$ transition at $\theta = 0^\circ$, and (iv) the outer $\Delta M_s = 2$ lines were not observed because their transition probabilities were too low. (It was calculated that the weakest observed lines were actually below the specified spectrometer sensitivity). In Fig.4.6 the energy levels of cubic Gd^{3+} are plotted against magnetic field for $\underline{B} \parallel \langle 100 \rangle$. The solid arrows indicate observed transitions, and the dotted arrows indicate 'transitions' which were not observed at this angle due to their having zero transition probability.

The variation in intensity of one of the $\Delta M_s = 2$ transitions in a $\{100\}$ plane is plotted against the calculated transition probability in Fig.4.5, the two curves having been normalized at the peak intensity. Except at the peaks and null points the experimental intensity has the

FIGURE 4.4 A comparison between the computed angular variation and measured line positions of cubic Gd^{3+} for $\underline{B}$ in a {100} plane. Crosses are unidentified lines.

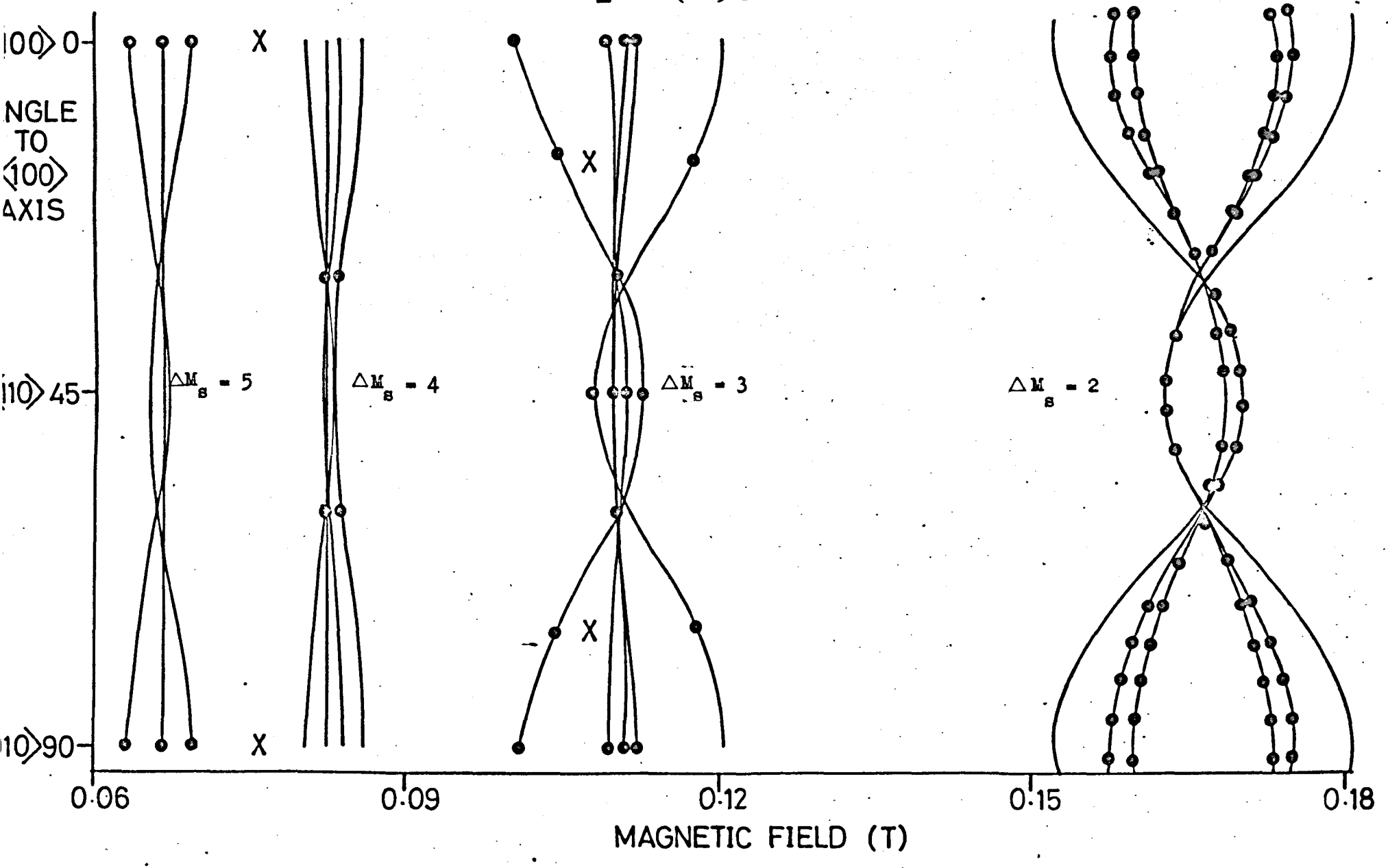

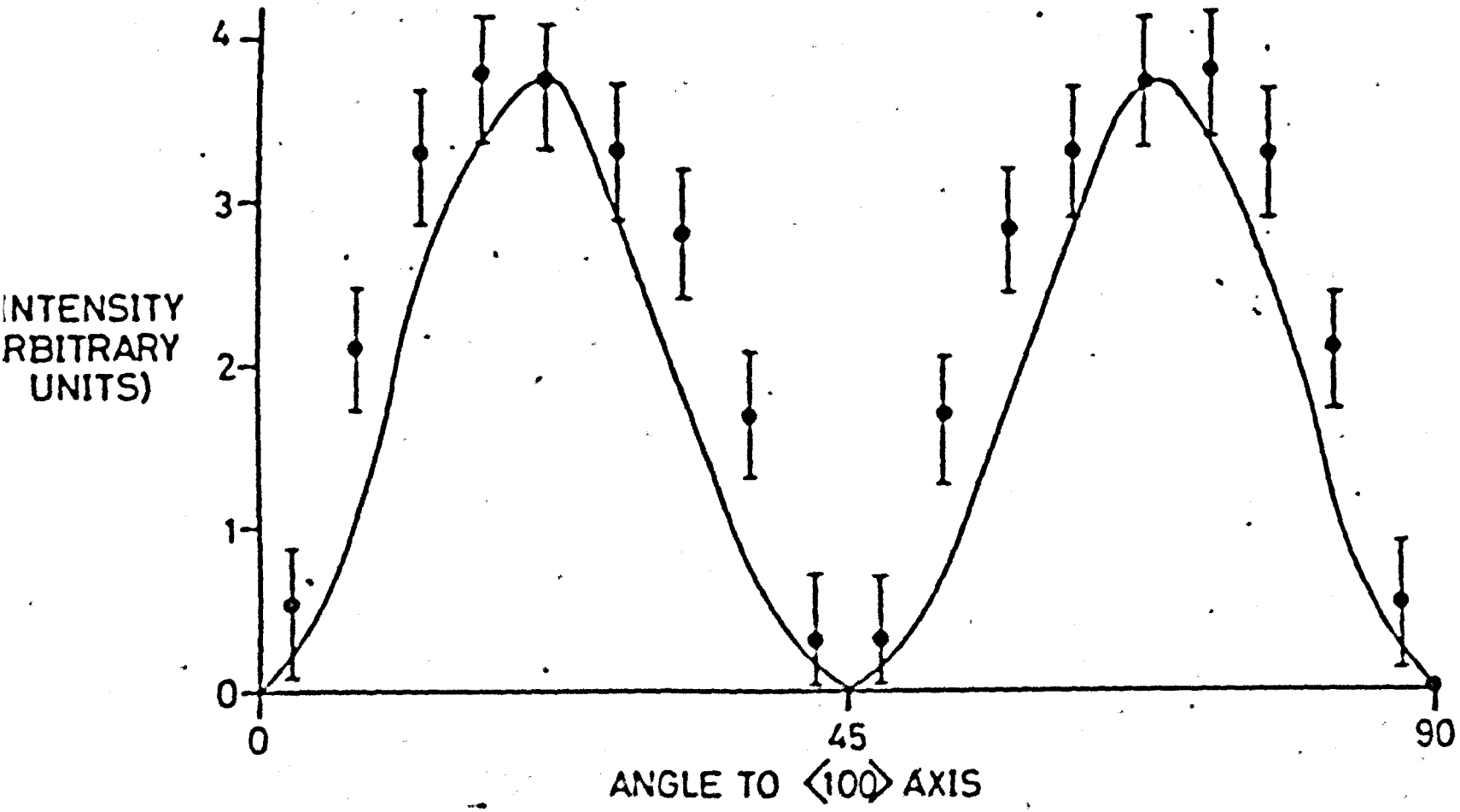

FIGURE 4.5 Variation of the intensity of a $\Delta M_s = 2$ transition and the intensity calculated by computer program of the same transition (solid line) plotted against angle for $\underline{B}$ in a {100} plane.

higher value. The explanation for this probably lies in the geometry of the EPR cavity. In order to observe the lines a large sample was used. Consequently parts of the sample were exposed to a component of the microwave magnetic field which was perpendicular to both the usual vertical component and the static magnetic field. This effectively allows both S_x and S_y to induce transitions, and the experimental intensity is expected to be higher than the intensity calculated by the computer program using S_y (or S_x) alone. Zero intensity at $\theta = 0^\circ$ arises because the operators S_x and S_y only connect states differing in their M_s value by ± 1, whilst the eigenvectors of the spin Hamiltonian are linear combinations of $|M_s\rangle$ with either $|M_s + 4\rangle$ or $|M_s - 4\rangle$. The intensity falls to zero at $\theta = 45^\circ$ because of cancellations between terms. At intermediate angles the transitions are observed because there is sufficient unsymmetrical mixing between states to allow S_x and S_y to connect them.

In view of the excellent agreement between theory and experiment in Figures 4.4 and 4.5, there can be little doubt that the spectra in Fig.4.3 are correctly attributed to forbidden transitions of the cubic Gd^{3+} ion.

4.4 Gd^{3+} at sites of orthorhombic symmetry

The intensities of the three orientation sensitive lines (section 4.2) and several others, spread over the whole magnetic field range available on the X-band spectrometers, were larger in the annealed sample by a factor of ~4. Some of the lines were visible on the oscilloscope, which made preliminary angular variation experiments in $\{100\}$, $\{110\}$ and $\{111\}$ planes possible. An accurate angular study was attempted in the $\{100\}$ plane because the lines were generally more intense. The results are plotted in Fig.4.7, in which the curves represent the most probable changes in line position. Some of the lines at low

FIGURE 4.6 Energy levels of cubic Gd^{3+} plotted against magnetic field for $\underline{B} \| \langle 100 \rangle$. Solid arrows indicate observed transitions, dotted arrows those transitions which were not observed due to them having zero transition probability.

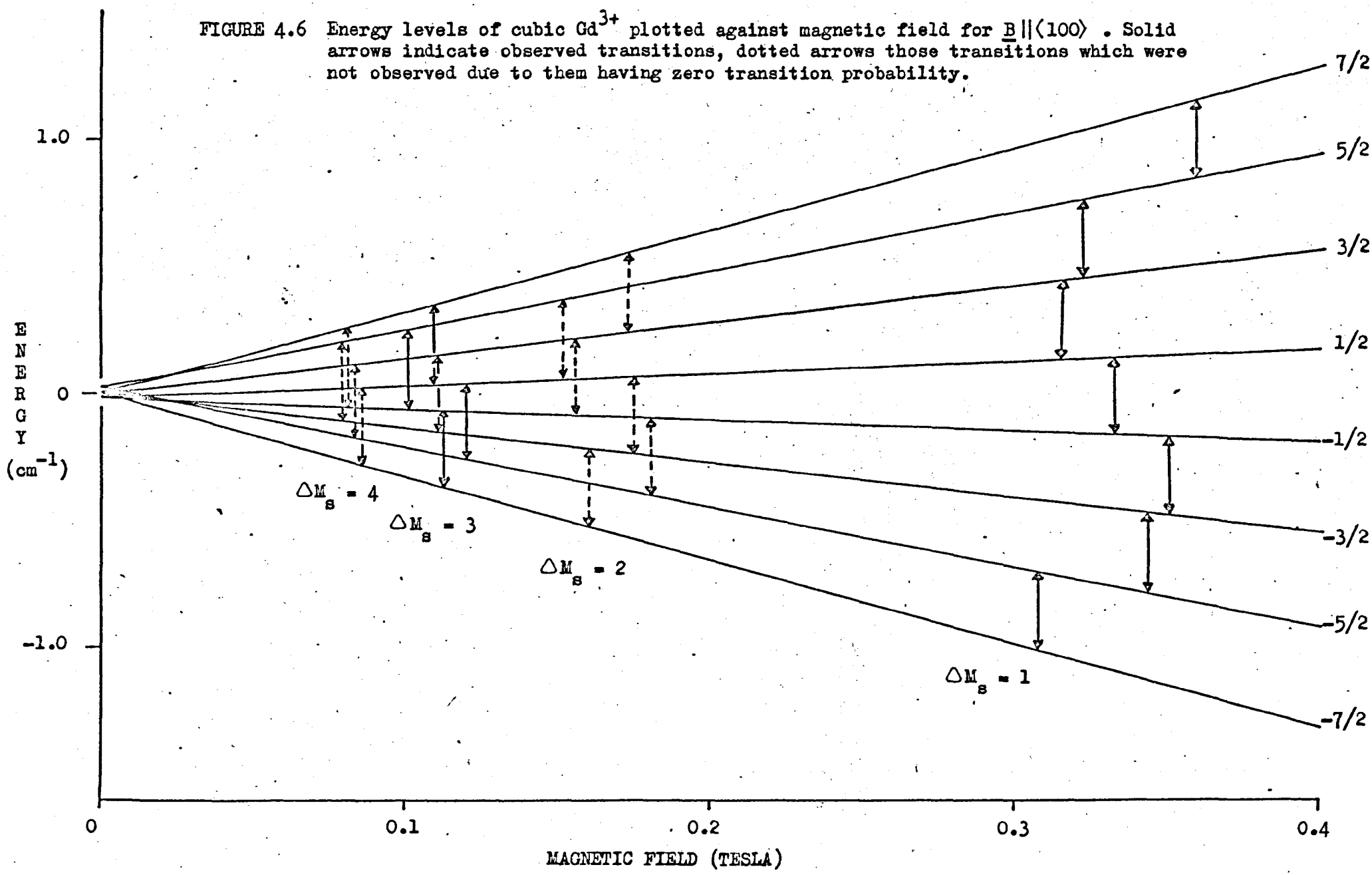

FIGURE 4.7 Angular behaviour of the other weak lines in the X-band spectrum, with $\underline{B}$ in a {100} plane.

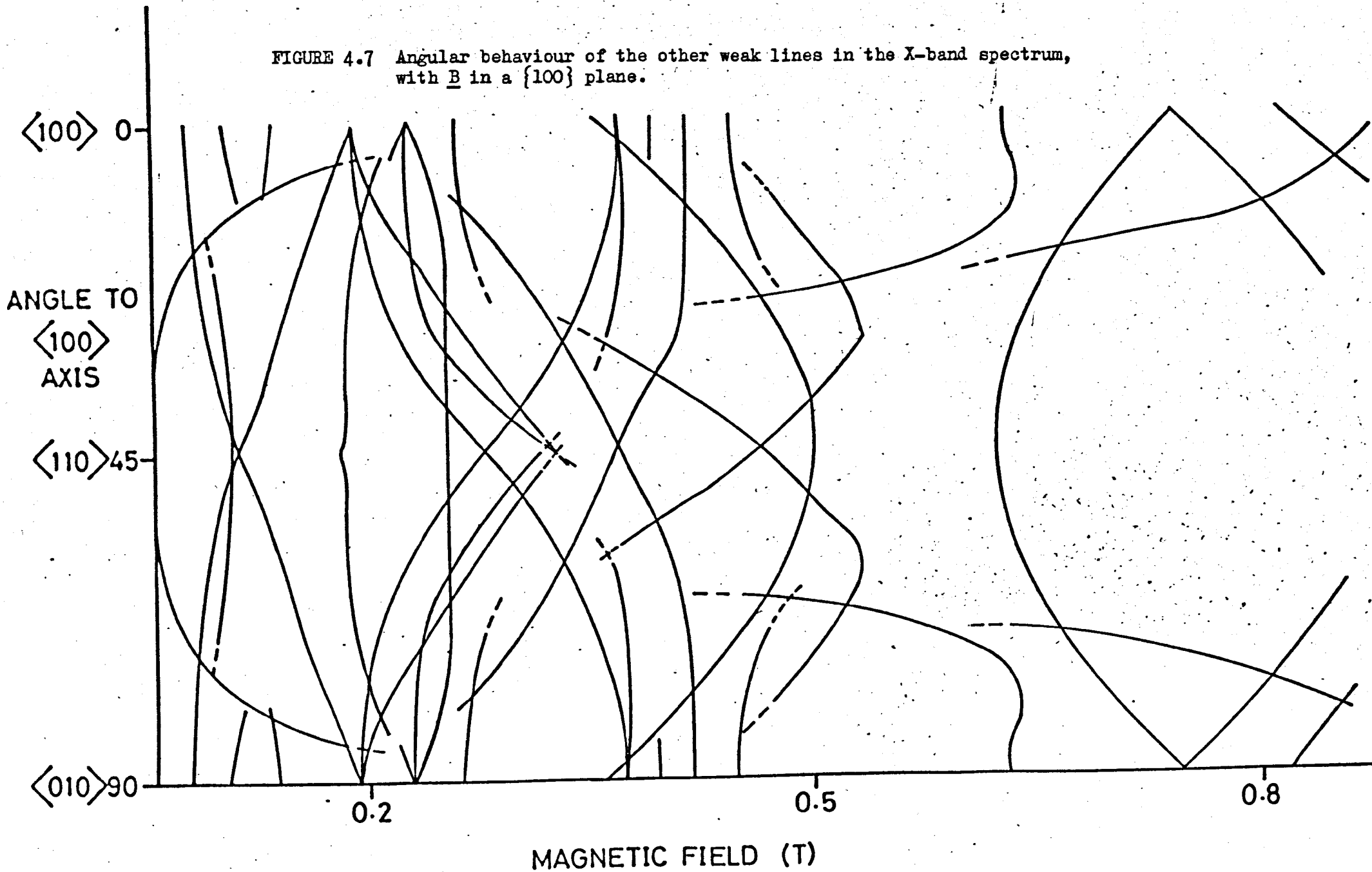

field disappeared as the sample was rotated, and others, indicated by broken lines were not easy to follow because a 5^{o} change in magnetic field direction caused them to move by $\sim$200 mT. Figure 4.7 shows none of the regularities which aid the interpretation of EPR spectra. Similar results for orientations in $\{110\}$ and $\{111\}$ planes suggested that some, if not all, of the lines were from a centre with zero-field splitting large compared to the X-band quantum. Clearly, measurements at Q-band frequencies, where the energy of the quantum is nearly four times the energy of the X-band quantum, offer a considerable advantage in the interpretation of such spectra.

Orientation of the small sample in the Q-band cavity was facilitated by observing the cubic Gd^{3+} spectrum, which allowed the $\langle 100 \rangle$ axes to be determined within $\sim 2^{o}$. At this orientation of the magnetic field there were some 25 weak lines in the field range 0.5 T to 1.55 T. These lines were clustered in groups, so attempts were made to reduce the splittings between lines in a group by making small adjustments to the position of the sample. An example of the simplification which can be introduced is shown in Fig.4.8. The lower trace shows the spectrum with $\underline{B}$ at $\sim 2^{o}$ to $\langle 100 \rangle$ and the upper trace, recorded with a slightly more compressed magnetic field sweep, is the reoriented version of maximum simplicity. The lines A4L and A3L missing from the lower trace did not split.

A preliminary Q-band survey was made for rotations of $\underline{B}$ about the three common axes of rotation in cubic crystals. Subsequently an accurate study was made of rotations in a $\{100\}$ plane, because this plane included the orientation for which the maximum splitting of the spectrum was obtained. The results of this study are presented in Fig.4.9, in which the curves connect equivalent EPR lines at different angles, evidence of linewidth, lineshape, intensity and splitting with misorientation having been taken into account. The lines which split

FIGURE 4.8 Orthorhombic Gd^{3+}. The upper trace shows all the visible spectrum for $\underline{B} \parallel \langle 100 \rangle$, the magnetic field ranging from 0.5 to 1.5 T. The lower trace, recorded with slightly expanded field sweep, shows the spectrum with $\underline{B}$ at ~2° to $\langle 100 \rangle$. The lines are labelled A or B depending on their splitting behaviour under the misorientation, and xL or xH depending on their relative position to Low or High field of $g \sim 2.0$.

when B was near to the ⟨100⟩ direction, designated type B, are shown at $\theta = 0^\circ$ and 90° as triangles. At intermediate angles the triangles represent lines which return to their original positions at $\theta = 0^\circ$ or 90°. Type A lines (which did not split) are shown as solid dots on the figure when $\theta = 0^\circ$ or 90°; at intermediate angles the dots represent lines which become type A at either of these angles. Unidentified lines are shown as solid squares. Figure 4.9 indicates that, when the magnetic field direction changed from ⟨100⟩ to ⟨010⟩, type A lines exchanged position with components of the type B lines. In detail the changes (using the labels of Figs.4.8 and 4.9) A3L to B3H, A2L to B2H and A2H to B2L were actually observed, but the following proposed changes, based on the same pattern, were not observed because the lines moved rapidly to fields higher than those available: A4L to B4H, A3H to B3L and A4H to B4L. The change A1 to B1 was obscured by the cubic Gd^{3+} lines.

The interpretation of Fig.4.9 was aided by a comparison with the angular variation of orthorhombic Gd^{3+} in $ThSiO_4$ (Reynolds et al,1972), which has similar exchanges of line position, but with an 18° phase shift between the spectra from inequivalent sites. By introducing a 90° phase shift it could be seen that the type A lines arose because, for some sites, the magnetic field was directed along an axis of major distortion in the crystal field. This axis, parallel to ⟨100⟩, was defined as the z axis for these sites because the type A lines exhibit the maximum overall splitting of the spectrum. The 90° variation to produce type B lines indicated that these arose because the magnetic field was in the plane perpendicular to the z axis of other sites (the xy plane of these sites), and the fact that the type B lines were approximately twice the intensity of the A lines confirmed this. Reference to Fig.4.10 makes the interpretation easier. Although there are six crystal directions for the z axes of different sites, only three need be considered since the positive and negative pairs of each are indistinguishable by EPR. In

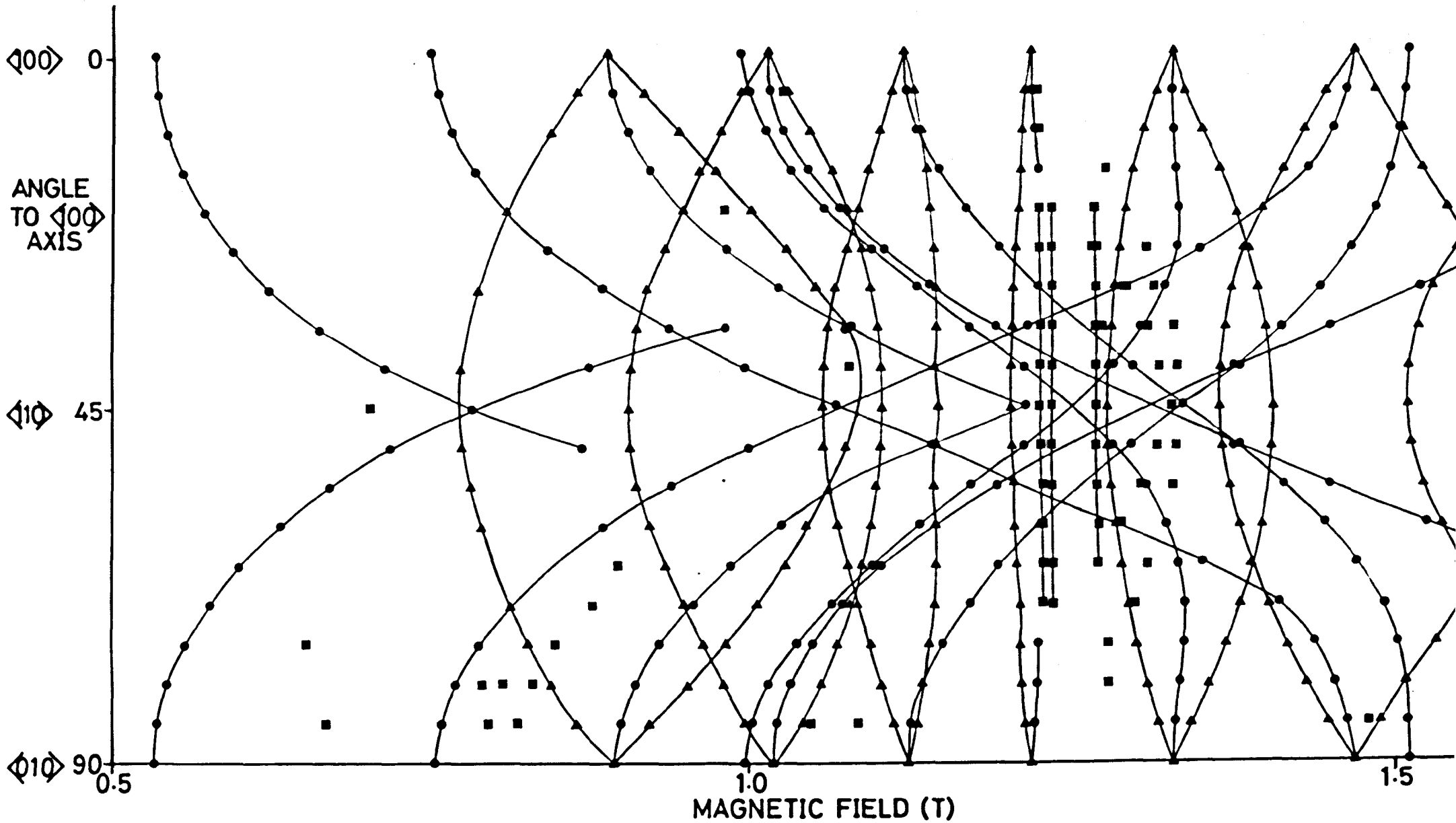

FIGURE 4.9 Angular variation of the orthorhombic Gd^{3+} spectrum at Q-band for $\underline{B}$ in a {100} plane.

Fig.4.10(i) the $\theta = 0^{\circ}$ orientation of the magnetic field (here θ is measured with respect to the crystal axes, and this orientation corresponds to $\underline{B} \parallel \langle 010 \rangle$) allows the observation of EPR lines from the xy plane of this centre, giving type B lines, but when $\theta = 90^{\circ}$ $\underline{B}$ is parallel to the z axis of the centre, $\langle 100 \rangle$, and type A lines are observed. For sites with z axes directed as in Fig.4.10(ii) the reverse occurs for the same change in magnetic field direction, so these two diagrams satisfactorily explain the A to B interchange. In Fig.4.10(iii) the plane of rotation of the magnetic field is the xy plane of the centres, perpendicular to the z axis. When $\theta = 0^{\circ}$ and 90° the lines from these sites are equivalent to the type B lines from the others, but when $\theta = 45^{\circ}$ one component ($\frac{1}{4}$ the intensity of the original type B line) has a high field turning point, and the other, of equal intensity, has a low field turning point (see Fig.4.9, curves with triangular points). These turning points correspond to the conventional assignment of the x and y directions of the crystal field, and in this case the turning points occurring farthest from the centre of the spectrum at $g \sim 2.0$ were assumed to arise because $\underline{B}$ was parallel to the x axes of some sites. Two additional pieces of information confirm this interpretation. Firstly, for a random orientation of the magnetic field the maximum number of components of an A-B line pair was six, indicating six distinguishable z axes. Secondly, the assignment of lines requires there to be seven lines from each site, but not all of these were observed. However, at highest magnetic field on Fig.4.9 the loop of triangular points between $\theta = 25^{\circ}$ and 65° corresponds to a low field component of line B4H, confirming the presence of seven type B lines.

In order to describe the angular behaviour of S = 7/2 orthorhombic spectra all even terms of the spin operators O_m^n up to sixth order are generally required in the spin Hamiltonian. The large overall splitting of the lines precluded the use of perturbation theory, so the spin

FIGURE 4.10 Inequivalent sites of orthorhombic Gd^{3+}.

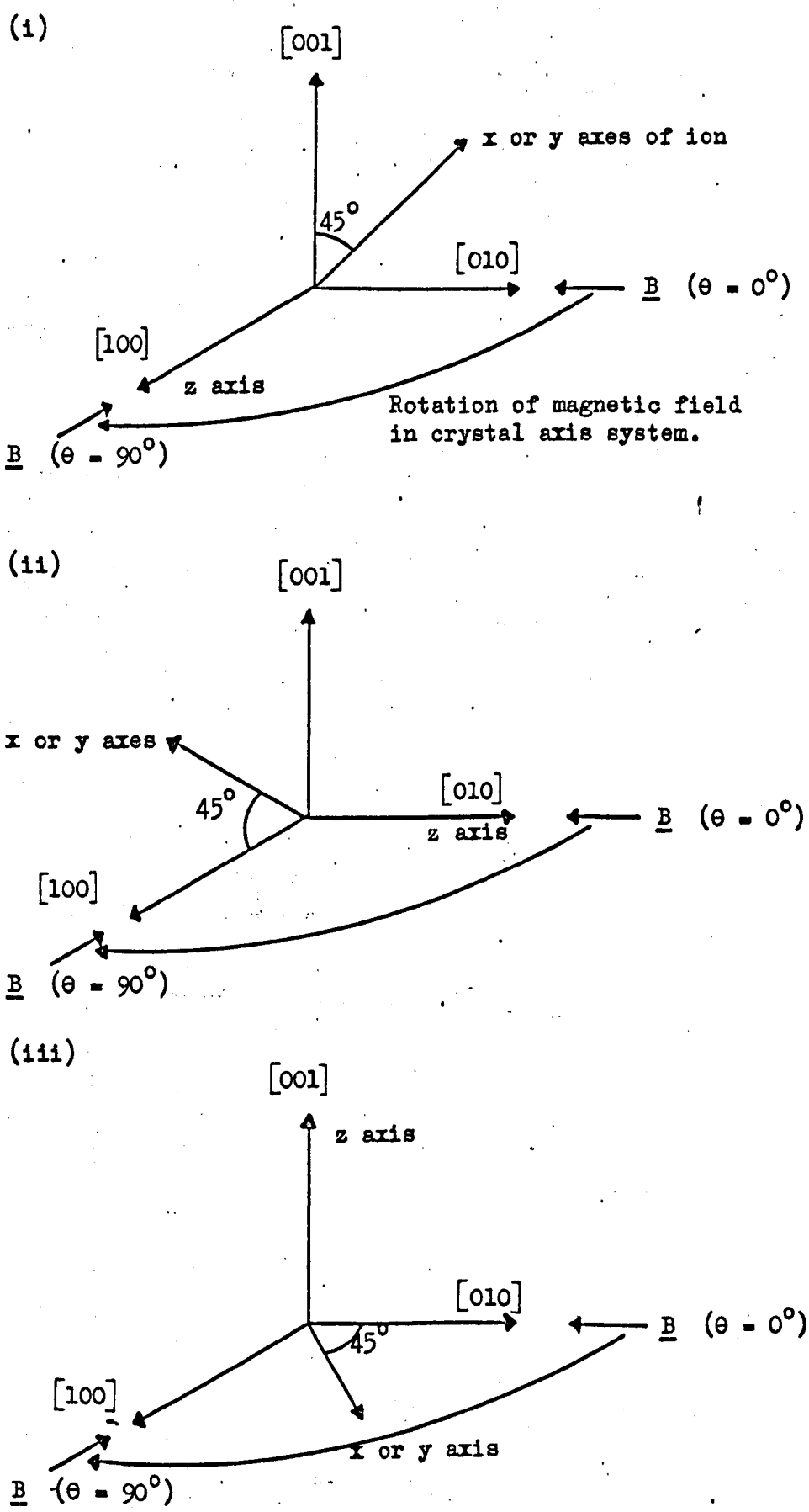

Hamiltonian parameters were determined by using a version of the least squares fitting computer program MNES. The program available contained only fourth order crystal field terms and the cubic sixth order terms, so this version was edited to include all the terms of the spin Hamiltonian

$$\mathcal{H} = g\mu_B \underline{B}.\underline{S} + \frac{1}{3}(b_2^0 O_2^0 + b_2^2 O_2^2) + \frac{1}{60}(b_4^0 O_4^0 + b_4^2 O_4^2 + b_4^4 O_4^4) + \frac{1}{1260}(b_6^0 O_6^0 + b_6^2 O_6^2 + b_6^4 O_6^4 + b_6^6 O_6^6). \qquad 4.3$$

Using the published data of Reynolds et al (1972) the general order of energy levels was determined by a small program written for this purpose, and the modified version of MNES was checked against this data. The program was run on the CDC 7600 Computer at the University of Manchester Regional Computer Centre. The maximum run time on this machine is only 30 minutes, sufficient for about a sixth of the calculations required to find the best fit parameters. This problem was partially overcome by restarting the program after each run using the parameters at the end of the last completed parameter variation. Unfortunately this decreases the power of the minimisation procedure, which involves finding one best fit and then searching from scratch for another which is an improvement on the first.

Two different computations were performed to check the spin Hamiltonian parameters. Firstly the input data consisted of the A to B line variation, and secondly the x to y axis variation. In terms of the usual polar angles these rotations are respectively from $\theta = 0^\circ$, $\phi = 45^\circ$ to $\theta = 90^\circ$, $\phi = 45^\circ$ and $\theta = 90^\circ$, $\phi = 0^\circ$ to $\phi = 90^\circ$. In both cases the input magnetic field positions were the mean of the two values obtained from equivalent lines at angles θ and $90 - \theta$. Data from ten different angles were used in each run. In the first case the best fit parameters gave a mean deviation between experimental and calculated field positions of ~1.2 mT, whereas in the second case the mean deviation was ~3.0 mT.

TABLE 4.2

Spin Hamiltonian Parameters for orthorhombic Gd^{3+} at Q-band

g	=	1.987	$\pm$ 0.001	
b_2^0	=	- 0.115	$\pm$ 0.001	cm^{-1}
b_2^2	=	0.019	$\pm$ 0.002	cm^{-1}
b_4^0	=	0.001	$\pm$ 0.001	cm^{-1}
b_4^2	=	- 0.005	$\pm$ 0.001	cm^{-1}
b_4^4	=	- 0.006	$\pm$ 0.001	cm^{-1}
b_6^0	=	0.000	$\pm$ 0.001	cm^{-1}
b_6^2	=	0.019	$\pm$ 0.001	cm^{-1}
b_6^4	=	- 0.001	$\pm$ 0.001	cm^{-1}
b_6^6	=	0.004	$\pm$ 0.003	cm^{-1}

The mean values of the best fit parameters for these two runs are listed in Table 4.2. Close agreement was found for all but b_6^6, a small parameter which as a consequence has the largest error attached to it. The negative sign of b_2^0 has been assumed, following Reynolds et al (op cit) who actually determined it from a depopulation experiment at 4.2 K, and the large body of other experimental results (Buckmaster and Shing,1972). No immediate explanation is offered for the discrepancy between the mean deviations of the two computer runs, but to put the errors into perspective, the points on Fig.4.9 are approximately 20 mT across.

Figure 4.11 is a plot of the energy of the eight M_s levels of orthorhombic Gd^{3+} in CaO as a function of magnetic field, with $\underline{B}$ directed along the z axis. In contrast to the energy levels of the ion in cubic symmetry, these levels are split into four doublets at zero field. The observed Q-band type A transitions are indicated by solid arrows, the dotted arrows representing transitions which are predicted to occur at fields higher than those available from our laboratory electromagnets. The line A1 was obscured by the Gd^{3+} cubic spectrum. Note that due to the close proximity of levels at low field some $\Delta M_s = 1$ transitions may be excited by quanta with frequencies in the X-band range. Furthermore, some of these transitions may occur twice, on each side of a "cross-over point", so adding to the complexity of the X-band spectrum.

Although the typical gadolinium hyperfine structure was obscured in the $\sim$3.5 mT linewidth, the spectrum is thought to arise from Gd^{3+} in an orthorhombic crystalline electric field. The only other common $S = 7/2$ ion is Eu^{2+}, but the characteristic hyperfine structure of this ion would have been easily distinguished. Although the EPR spectrum of cubic Gd^{3+} in CaO is well known, this orthorhombic spectrum has not been observed previously. A possible explanation for this is its instability, as in the course of this work the spectrum was found to be unstable at room temperature in the presence of ultra violet light.

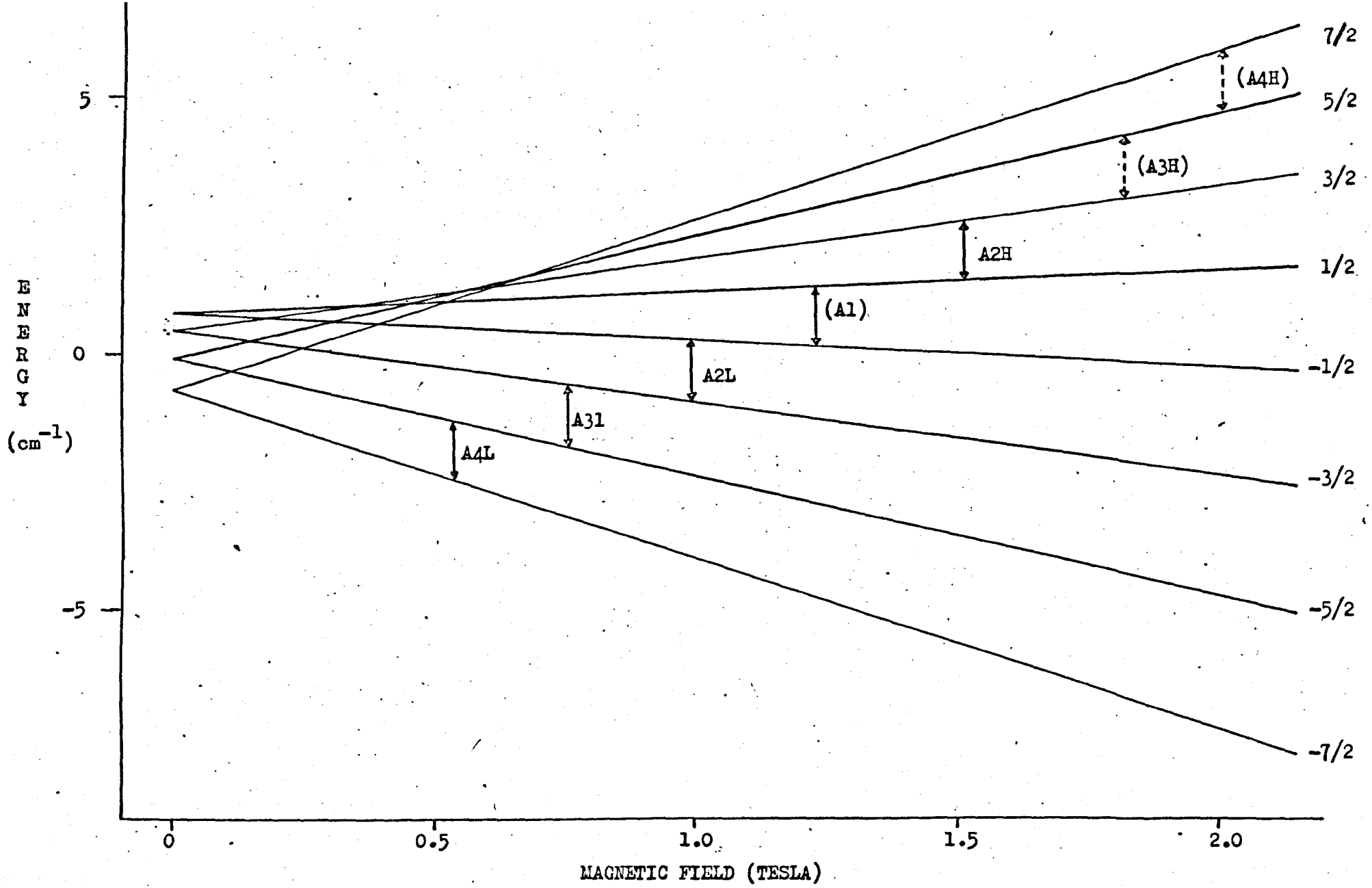

FIGURE 4.11 Energy levels of orthorhombic Gd^{3+} for $\underline{B} \| \langle 100 \rangle$. Solid arrows show observed type A transitions, dashed arrows those predicted to occur at fields higher than those available.

Buckmaster and Shing (op cit) have reviewed the EPR spectra of Gd^{3+} in ionic crystals. The present contribution to this growing body of experimental results is unique in that the size of the dominant b_2^o term in the spin Hamiltonian is almost 50% larger than typical values reported in the literature for orthorhombic Gd^{3+}. In common with other Gd^{3+} spectra the large b_2^o term is almost an order of magnitude larger than any of the other crystal field terms. This implies that the crystal field local to the Gd^{3+} ion is strongly axial in character.

The usual model proposed for the crystal surrounding impurity paramagnetic ions with orthorhombic spectra in the alkaline earth oxides involves the ion being perturbed by a single nearest neighbour cation vacancy along a ⟨110⟩ crystal direction, as in the case of Cr^{3+} and V^{2+} in MgO (Wertz and Auzins, 1967, Henderson and Codling, 1971). Although an attraction of this model is that one such defect compensates for the presence of two Gd^{3+} ions in the crystal, the major term in the spin Hamiltonian describing such centres is directed along ⟨110⟩ and not ⟨100⟩. In order for the largest crystal field term to be directed along a ⟨100⟩ type crystal axis it seems natural to suggest that there is a vacancy local to the ion in this direction. In this case the two ⟨110⟩ axes in the plane perpendicular to this direction are naturally equivalent, so for an orthorhombic spectrum to be observed there must be an associated distortion in one of these directions. The inequivalence of these directions could result from either the relaxation of the Gd^{3+} ion away from the usual lattice site, or from a second minor defect along one of these axes e.g. a monovalent ion at a nearest neighbour position. The disadvantage of a model involving two defects is that neither an axial nor another orthorhombic spectrum was observed. These should arise from ions perturbed by just one of the two associated defects. Using EPR alone it is impossible to distinguish between any of these models, but ENDOR experiments might indicate whether there was a nearby impurity ion

not normally expected to be present.

Further information on this centre would be gained by studying its behaviour when the crystal is annealed using both optical and EPR techniques. The examination of other freshly grown alkaline earth oxide crystals doped with gadolinium may allow similar spectra to be observed and, in conjunction with the temperature variation of the crystal field parameters, indicate experimental trends.

CHAPTER V

A DEFECT WITH HYPERFINE STRUCTURE IN NEUTRON IRRADIATED CALCIUM OXIDE

5.1 Introduction

The spectrum reported in this chapter was observed during a sequence of experiments designed, in collaboration with Dr.A.E.Hughes, to study the spectroscopy of ions implanted into crystalline solids. Implantation was performed at UKAEA, Harwell, by directing energetic beams of ions accelerated in a high voltage electric field at planar single crystals of both MgO and CaO. Among the species investigated were ionic bismuth, europium, gadolinium, gallium, lithium and chromium; energies up to 400 keV and fluences of 10^{14} to 10^{15} cm^{-2} were typical. No EPR which could be unambiguously ascribed to implanted ions was observed from any of these species. One of the major difficulties involved in attempts to observe such spectra was the presence in all the crystals of resonance lines from other impurities in the critical $g \sim 2.0$ region. These lines were often of higher intensity than those expected from the implanted ions. Larger fluences were not attempted due to the longer exposure times required, and because higher concentrations are not always helpful: the ions only penetrated to depths of ~ 1 micron, and the close proximity of similar ions can give rise to inhomogeneous broadening, making observation of the lines even more difficult. Samples of MgO, CaO and CaF_2, proton irradiated to fluences of 10^{15} cm^{-2} and 10^{16} cm^{-2}, were also examined, the dose being delivered in equal amounts at 100,200,300 and 400 keV. However, no EPR spectra due to atomic hydrogen were observed in the implanted samples, or in crystals annealed at 400 C, subsequent to proton irradiation.

In the course of these experiments very high purity samples of CaO were neutron, proton and electron irradiated. The spectrum discussed in this chapter was observed in a slightly cloudy, pale green crystal which had been neutron irradiated to a dose of $\sim 10^{17}$ nvt (energy greater

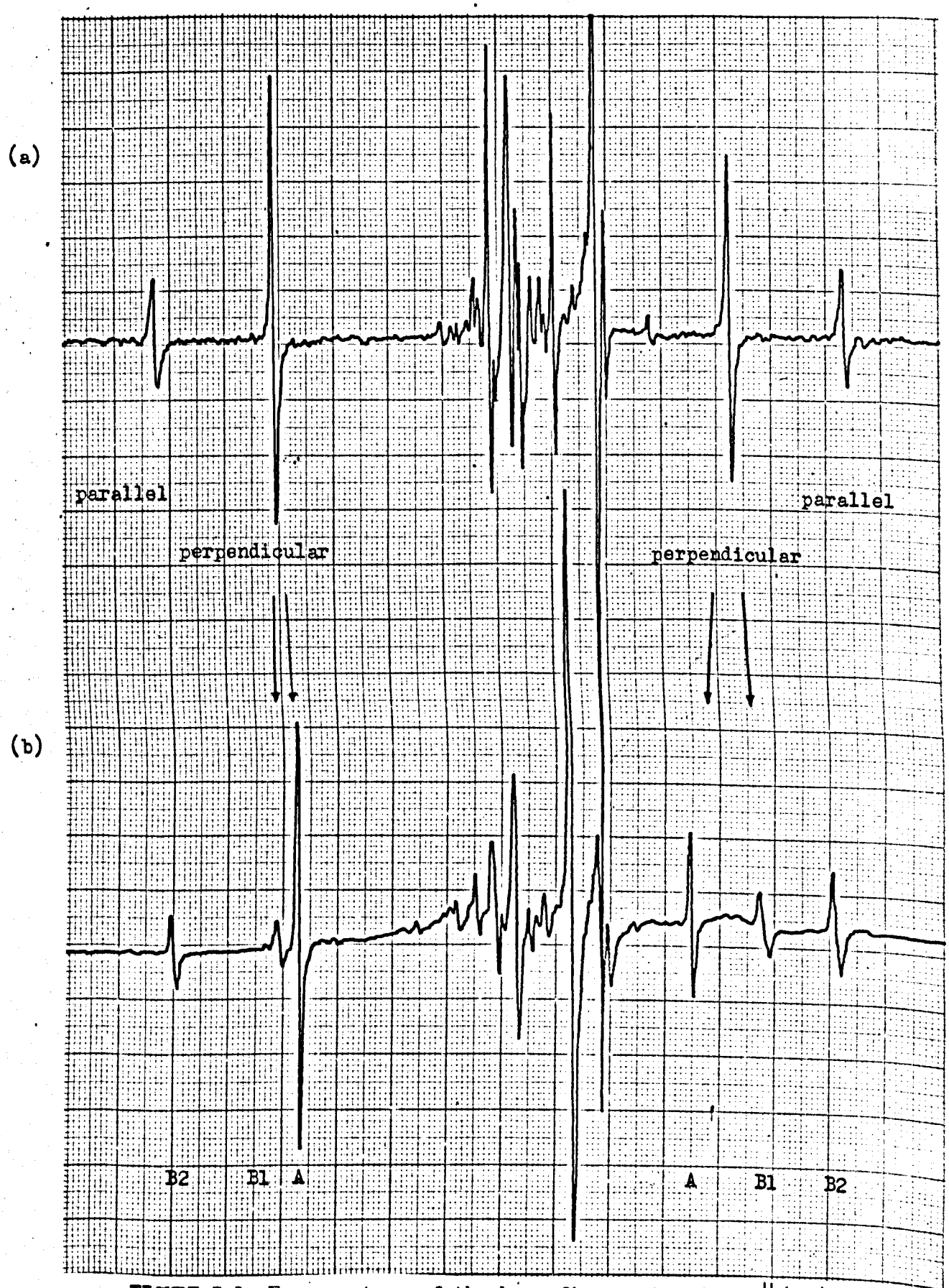

FIGURE 5.1 Epr spectrum of the hyperfine centre for $\underline{B} \parallel \langle 100 \rangle$
(a) at room temperature
(b) at 77 K.
The arrows indicate how the room temperature perpendicular lines split on cooling.

than 2 MeV). Similar spectra were not observed in the other crystals, which had been proton or electron irradiated to approximately the same level. Figure 5.1a shows the spectrum at room temperature with the magnetic field directed along a ⟨100⟩ crystal axis. Other defect resonances in the central $g \sim 2.0$ region were also observed. The spectrum consists of four lines equally spaced about $g \sim 2.0$. The outer pair of lines, split by ~7.5 mT, are roughly half the intensity of the inner pair, which are split by ~ 5.0 mT. On cooling the crystal each of the doubly intense inner lines split into two orientation sensitive components of different shape but similar intensity, the changes occurring in the temperature range 180 - 210 K. At 77 K (Figure 5.1.b) the low field pair split by less than the pair to higher field, destroying the symmetrical disposition of the lines. The outer singly intense lines moved slightly in position but did not split on cooling. None of the lines saturated at room temperature or 77 K when the maximum power available from the klystron was incident on the cavity.

5.2 Angular behaviour of the room temperature spectrum

The angular variation of the spectrum for magnetic field orientations in a {100} plane is illustrated in Figure 5.2. One component of each doubly intense inner line is invariant in this plane, whilst the other components exchange position with the singly intense lines outside them, crossing when $\underline{B} \parallel \langle 110 \rangle$. The common behaviour of the inner lines on cooling confirmed that all the lines were related, and so discounted an interpretation in terms of two spin Hamiltonians with axial symmetry and $S = \frac{1}{2}$. The only alternative was an $S = \frac{1}{2}$, $I = \frac{1}{2}$ hyperfine centre with axial symmetry. Confirmatory evidence was obtained when the sample was mounted with $\underline{B} \parallel \langle 111 \rangle$, when two triply degenerate lines were observed. At this orientation $\underline{B}$ makes an angle of 54.7° with each of the three different z axes distinguishable using EPR.

Although the spin Hamiltonian parameters of the spectrum could

FIGURE 5.2 Room temperature angular variation of the spectrum for $\underline{B}$ in a {100} plane.

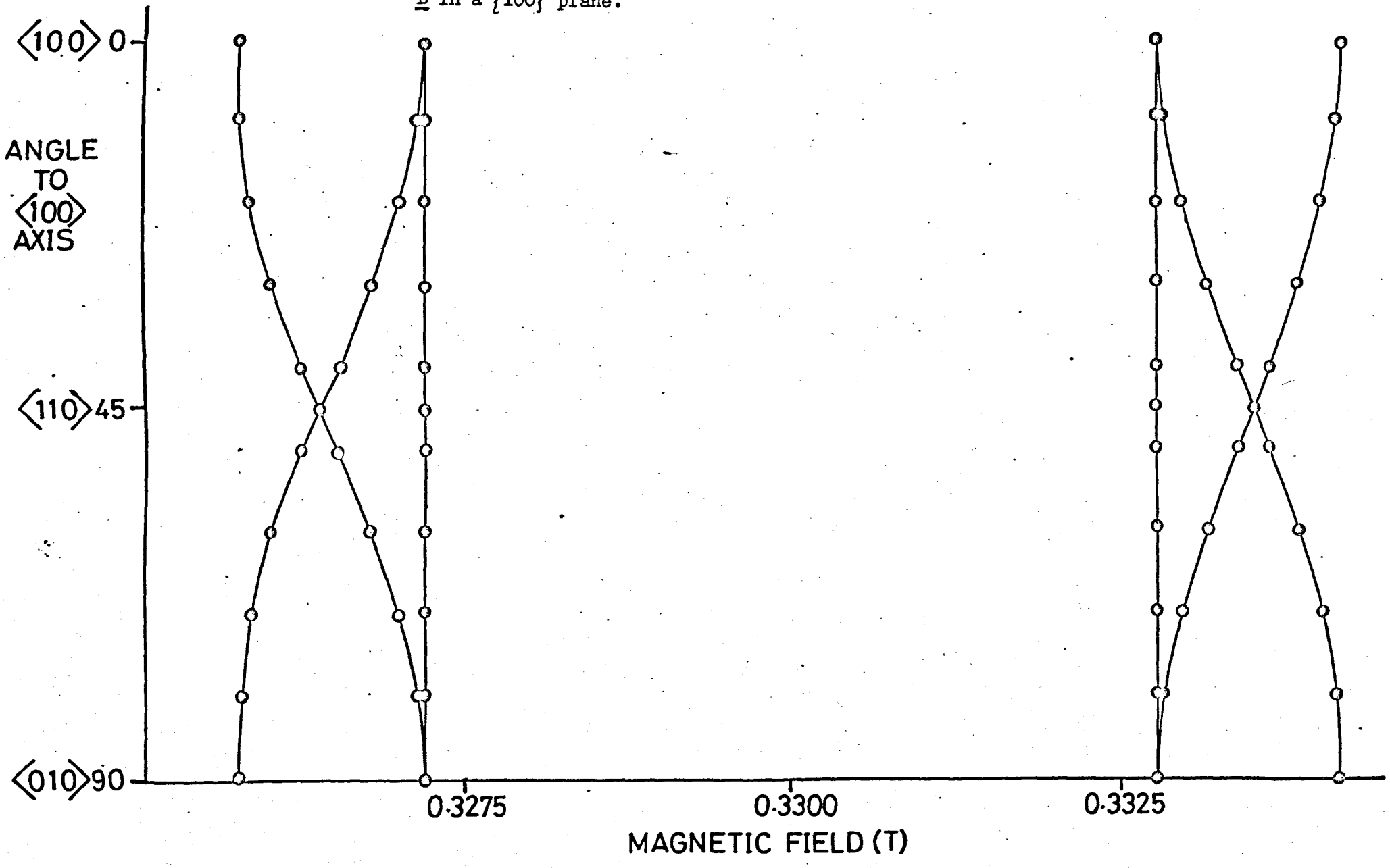

be determined accurately using perturbation theory, they were actually determined using computer program MNES. The input magnetic field positions, obtained using a proton resonance probe, were the mean values of those measured when $\underline{B}$ was parallel to all the $\langle 100 \rangle$, $\langle 110 \rangle$ and $\langle 111 \rangle$ axes available when the sample was rotated in both $\{100\}$ and $\{110\}$ planes. The best fit parameters to the spin Hamiltonian ($S = \frac{1}{2}$, $I = \frac{1}{2}$)

$$\mathcal{H} = g_{\parallel} \mu_B S_z B_z + g_{\perp} \mu_B (S_x B_x + S_y B_y) + A_{\parallel} S_z I_z + A_{\perp} (S_x I_x + S_y I_y) \qquad 5.1$$

were

$$g_{\parallel} = 2.0067 \pm 0.0001$$

$$g_{\perp} = 2.0064 \pm 0.0001$$

$$A_{\parallel} = 0.0077 \pm 0.0001 \ \text{cm}^{-1}$$

$$A_{\perp} = 0.0051 \pm 0.0001 \ \text{cm}^{-1} \ .$$

The mean deviation of the experimental field positions from those calculated using these parameters was ~ 0.02 mT.

5.3 Angular behaviour of the spectrum at 77 K

The more complex $\{100\}$ plane angular variation of the 77 K spectrum is illustrated in Figure 5.3. Generally in this plane there are sixteen lines, although this reduces to six lines for $\underline{B} \parallel \langle 100 \rangle$, and eight when $\underline{B} \parallel \langle 110 \rangle$. The six lines at $\theta = 0^\circ$ or 90°, labelled A and B in Fig.5.3, are respectively two-fold and three-fold degenerate. Otherwise the labelling convention follows that established in Chapter IV. Type A lines at $\theta = 0^\circ$ (90°) split and contribute one component each to lines B1 and B2 at $\theta = 90^\circ$ (0°). Apart from the components connected with type A lines, the B lines split into two further components. Each of these has a turning point at different angles, one to higher and the other to lower field, but the lines which were B1 at $\theta = 0^\circ$ (90°) both become B2 at $\theta = 90^\circ$ (0°), and vice versa. At $\theta = 45^\circ$ ($\underline{B} \parallel \langle 110 \rangle$) there are four two-fold coincidences on either side of

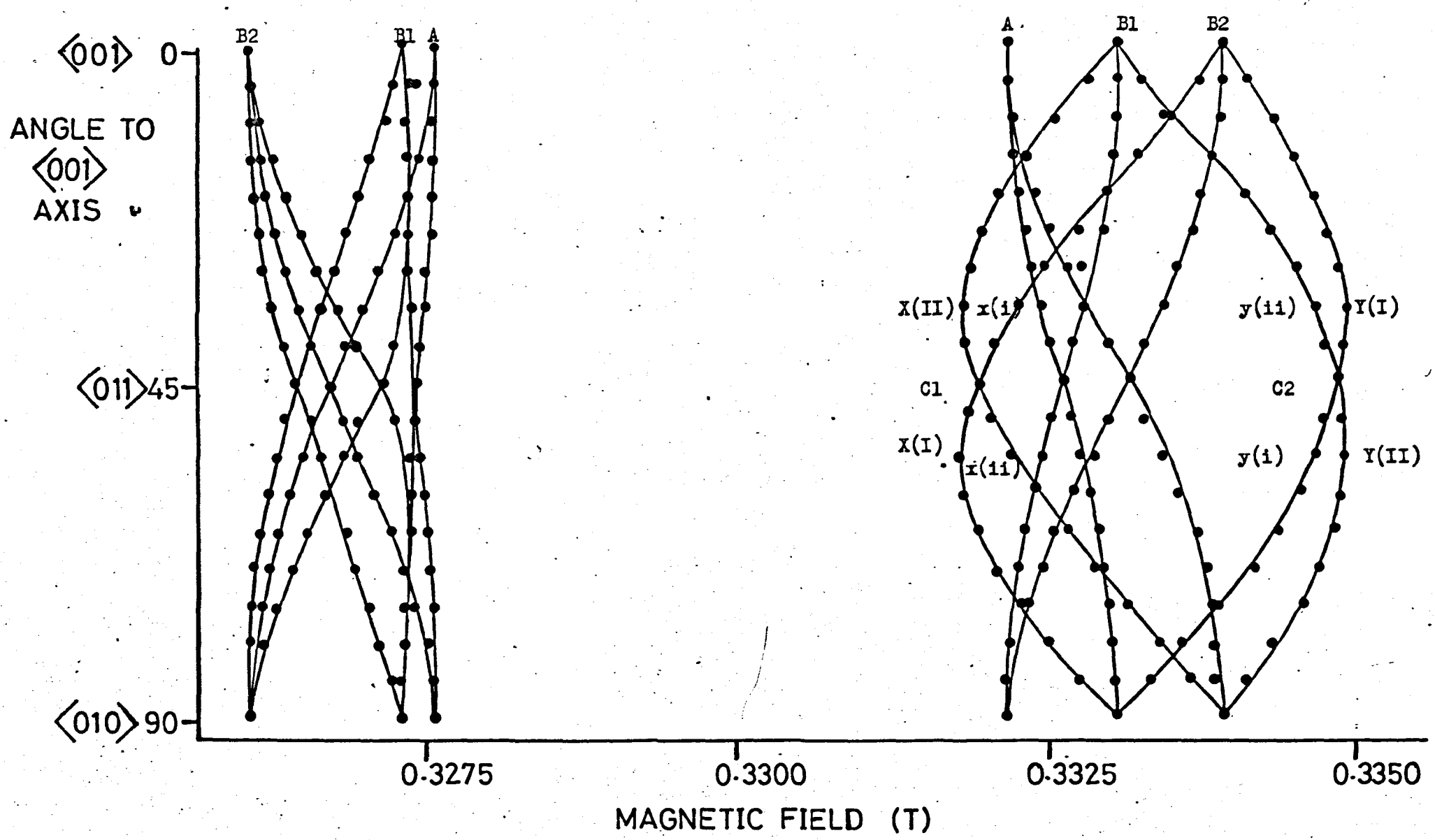

FIGURE 5.3 Angular variation of the spectrum at 77 K for $\underline{B}$ in a {100} plane. Labels are given in the text.

$g \sim 2.0$. The behaviour is easier to follow for the lines to higher field because of the asymmetry in the spectrum.

Following the assignment of the room temperature spectrum, another $S = \frac{1}{2}$, $I = \frac{1}{2}$ centre was anticipated, and the complex behaviour suggested that the symmetry was lower than axial. Sensitivity to mis-orientation, particularly for the type B lines, suggested orthorhombic symmetry, and the behaviour was explained using this assumption. The two components making up the A lines which collapse and have a turning point at $\theta = 0^\circ$ (90°) were interpreted as lines arising from two different centres for which $\underline{B}$ is parallel to similar axes, designated z axes, which are therefore parallel to $\langle 100 \rangle$. The 90° variation of these to produce type B lines, suggests, as with orthorhombic Gd^{3+}, that the lines originating as type B which do not become type A arise because the magnetic field is directed in the xy planes of other sites. Although the xy plane variation is more complex here than that illustrated in Figure 4.7, similar features would be obtained if the type B lines at $\theta = 0^\circ$ and 90° on either side of $g \sim 2.0$ coalesced, because the turning points which occur at 35° and 55° would then become coincident at $\theta = 45^\circ$, and the A to B1, B2 curves would also be super-imposed on each other. The occurrence of turning points 10° on either side of $\langle 110 \rangle$ indicated that the x and y axes, rather than being directed along $\langle 110 \rangle$, were actually at 35° or 55° to $\langle 100 \rangle$. This would give twice the number of type B lines for each type A line than was observed in the case of orthorhombic Gd^{3+}, a feature found experimentally. Reference to Figure 5.4, in which the change in magnetic field direction shown on Figure 5.3 is represented by the variation $\underline{B} \parallel [010]$ ($\theta = 0^\circ$) to $\underline{B} \parallel [100]$ ($\theta = 90^\circ$), aids the interpretation. In Figure 5.4(i) $\underline{B}$ starts at 90° to the z axes of these sites, but at both 35° and 55° to different x axes (55° and 35° to different y's), producing B1 and B2 lines in the EPR spectrum. At $\theta = 90^\circ$, with $\underline{B}$ now

FIGURE 5.4 Inequivalent axes describing the angular behaviour of the orthorhombic spectrum observed at 77 K.

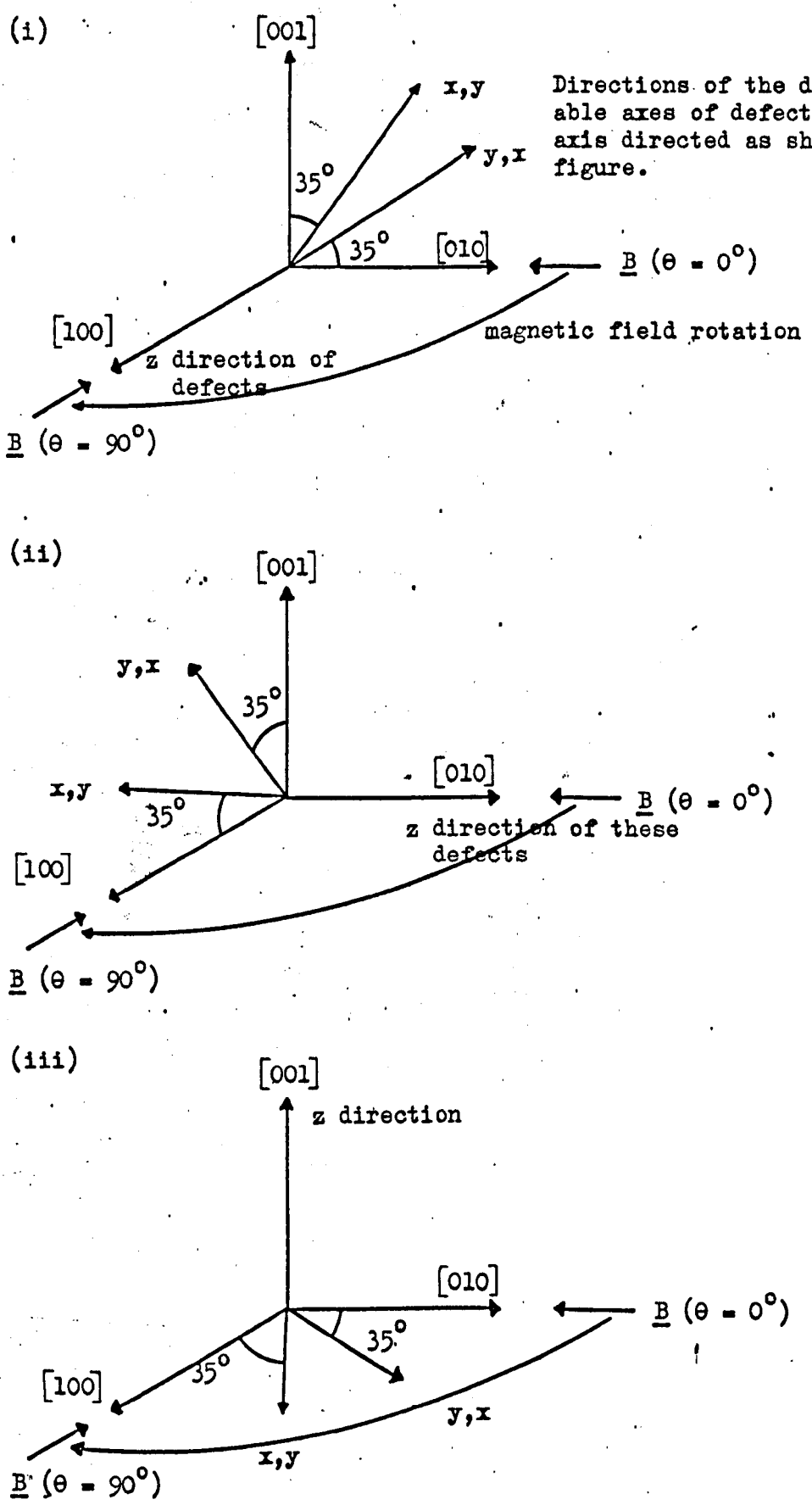

parallel to z, both these lines have become type A. The reverse occurs in Figure 5.4(ii) for the same change in magnetic field direction. The behaviour illustrated by Figure 5.4(iii), in which $\underline{B}$ is in the plane parpendicular to the z axes of these sites, is more interesting. $\underline{B}$ starts at both 35° and 55° to different x axes (55° and 35° to different y's) giving lines B1 and B2 in the EPR spectrum. When $\theta = 35^\circ$ $\underline{B}$ becomes parallel to both an x and a y axis, giving a lower field and a higher field turning point (X(II), Y(I) on Figure 5.3), and at the same time $\underline{B}$ is at 20° to other x and y axes (x(i), y(ii)), giving four lines in all. At $\theta = 45^\circ$ $\underline{B}$ is at 10° to either the x or y axis of all distinguishable axis systems with z axes perpendicular to the plane of the magnetic field, and the four lines collapse to two (C1, C2). When $\theta = 55^\circ$, the 'parallel' x and y axes at $\theta = 35^\circ$ are now at 20° to $\underline{B}$ (x(ii), y(i)) whilst those which were formerly at 20° are now parallel to $\underline{B}$ (X(I), Y(II)): four lines in all again. At $\theta = 90^\circ$ the x and y axes which were at 35° (55°) to $\underline{B}$ when $\theta = 0^\circ$ are now at 55° (35°), giving type B1 and B2 lines again, components having exchanged. Note that in the above discussion labels are only given for the high field angular variation because it is easier to follow: the variation to low field is a compressed reflection through $g \sim 2.0$. Confirmation of this interpretation was obtained from the number of lines observed at a general orientation of the magnetic field. As there are three distinguishable z directions each with four different combinations of x and y axes, the two halves of the spectrum should comprise 12 lines each. In the {100} plane eight are observed in each half, but with $\underline{B}$ directed $\sim 10^\circ$ out of this plane each A to B1, B2 line split into two, giving twelve in all.

The spectrum was fitted to the spin Hamiltonian ($S = \frac{1}{2}$, $I = \frac{1}{2}$)

$$\mathcal{H} = \mu_B(g_x B_x S_x + g_y B_y S_y + g_z B_z S_z) + A_x S_x I_x + A_y S_y I_y + A_z S_z I_z \qquad 5.2$$

in a similar manner to that employed at room temperature, and the best

fit parameters were

$$g_z = 2.0074 \pm 0.0001$$
$$g_y = 2.0042 \pm 0.0001$$
$$g_x = 2.0088 \pm 0.0001$$
$$A_z = 0.0044 \pm 0.0001 \ \text{cm}^{-1}$$
$$A_y = 0.0079 \pm 0.0001 \ \text{cm}^{-1}$$
$$A_x = 0.0040 \pm 0.0001 \ \text{cm}^{-1} \ .$$

The g and A tensors are coincident, g_z and A_z being directed along $\langle 100 \rangle$ axes. A_y, A_x, g_y and g_x are directed at $10 \pm 2^\circ$ to $\langle 011 \rangle$ axes in the $\{100\}$ plane perpendicular to the respective z axes, x and y components being at 90° to each other. The mean deviation between calculated and experimental field positions was ~ 0.1 mT. This error, roughly five times that obtained from the room temperature data, reflects the difficulties involved in orienting the crystal accurately and avoiding cavity drift at 77 K.

5.4 Discussion

The change in the spectrum from one of tetragonal symmetry to one of orthorhombic symmetry indicates that the low symmetry spectrum arises from the stable ground vibrational state of a defect. At higher temperatures thermally activated ionic motion allows some form of reorientation, and this results in a defect whose average configuration has the tetragonal symmetry already described. Two alternative hypotheses for the nature of the defect are (i) an unstable $S = \frac{1}{2}$ point defect in the lattice interacting with an $I = \frac{1}{2}$ impurity or (ii) an $I = \frac{1}{2}$ impurity ion with an $S = \frac{1}{2}$ valence state of low stability. In the former case either the point defect or the impurity (or both) is moving about in the lattice at higher temperatures, whilst in the latter case the ion would probably be off-centre with respect to a normal lattice site, motional averaging being accommodated by the ion jumping between

equivalent positions. The instability of the centre is in no doubt, because the spectra were only observed after neutron irradiation, and they were annealed out at 120° C. (There is some evidence that the centre can be generated by X-irradiation (Hall,1973)).

Speculation concerning the identity of the I = ½ impurity can be narrowed to one of two elements. There are only six elements which have 100% abundant I = ½ isotopes: hydrogen, fluorine, phosphorus, yttrium, rhodium and thulium. Of these ions, P is normally non-magnetic, and together with Rh, Tm and Y it is an uncommon impurity in the alkaline earth oxides. Both Tm^{2+} and Y^{2+} have been observed in CaF_2 using EPR. As expected for a lanthanide, the g-values of Tm^{2+} deviate markedly from 2.0 (Bessent and Hayes,1965), whilst those of Y^{2+} are closer to g_e, but resonance is only observed at 20 K and below (O'Connor and Chen,1964). EPR from Rh^0 in AgCl (Wilkens, de Graag and Helle,1965) and Rh^{2+} in $ZnWO_4$ (Whiffen and Orton,1965) has been observed, and in both cases g-value deviations from g_e of +0.2 were typical. On the basis of this evidence, taken with the fact that no other impurity resonances were observed in the experimental crystal, the accidental occurrence of one of these four elements is most unlikely. The other two elements, hydrogen and fluorine, are common impurities in the alkaline earth oxides, particularly the former in CaO due to hydrolysis (Henderson and Hughes, op cit), and one of these is thought to be involved in the defect. Although their nuclear properties are almost identical, they are far from identical chemically, and it is on this basis, together with some EPR evidence, that we can distinguish between them. Discounting the possibility of a paramagnetic ion of fluorine being involved in the defect, the most probable model involves a fluorine atom bonded to oxygen forming an S = ½ oxy-fluoro molecular ion. Possibilities are OF^{2-} and OF, and although neither of these has been prepared by conventional chemistry, the former has been

observed in neutron irradiated MgO (Rius and Cox,1968). The EPR spectrum was fitted to an axial spin Hamiltonian, with parameters $g_{||} = 2.0085$, $g_{\perp} = 2.0022$, $A_{||} = 424 \times 10^{-4}$ cm^{-1} and $A_{\perp} = 160 \times 10^{-4}$ cm^{-1}. These hyperfine constants are almost an order of magnitude larger than those reported here, and since no motional effects were observed, OF^{2-} is ruled out. The alternative hypothesis of a proton interacting with the magnetic electron is much more attractive (the small hyperfine parameters indicate that the electron is not actually orbiting the hydrogen nucleus). The proton is very small compared with fluorine, which results in much less stearic hindrance to its movement in the lattice. The least hindered direction in CaO is along ⟨111⟩ , and it is unlikely to be coincidental that the O-F bond in OF^{2-} points in this direction whilst in the present studies this axis was of no importance.

Assuming, therefore, that a proton is responsible for the hyperfine interaction, its position in the lattice assumes some importance. It would be unusual for a proton or neutral H atom to remain isolated in the crystal, and the most probable location for the former is combined with oxygen to form OH^- (Henderson and Sibley,1971). Although OH^- has an even number of electrons, a model for a defect involving this ion can be proposed. If the oxygen atom is situated at its usual lattice site and the hydrogen atom is bonded to it so that the O-H bond is directed approximately towards a unipositive calcium ion ($S=\frac{1}{2}$), a centre with the appropriate properties is obtained. Although OH^- is only slightly larger than O^{2-} (Wells,1962) the interaction between the positively polarized hydrogen atom and the larger Ca^+ ion would probably be sufficient to cause the displacement of the O-H bond vector away from the 'in line' ⟨100⟩ direction. One major disadvantage of this model is the involvement of Ca^+, a species which is chemically unknown. Indeed, studies of the Ca - CaX_2 (X = halide)

solid system which would be most favourable to its formation have failed to reveal the ion (Emons,1963). This is best explained in terms of the exceptionally high stability of Ca^{2+}, which has the argon inert gas electronic configuration. An unlikely variation on this model is the replacement of Ca^{2+} by a single electron trapped in a calcium vacancy. The properties of this centre would be similar to those of $Ca^{+} - OH^{-}$, but an electron surrounded by five O^{2-} ions and one OH^{-} would be highly destabilized: the site would be charged -3 relative to the perfect lattice, requiring a considerable amount of energy for formation.

The most attractive model for the defect involving hydrogen is the analogue of OF^{2-}, OH^{2-}, which could be formed during irradiation by an OH^{-} group capturing an additional electron. As the charge of this molecular ion is the same as the oxygen ion which it is assumed to replace, the only destabilizing influence could come from its increased size. Although OH^{-} is marginally larger than O^{2-}, with a bond length of $\sim$1.0 A (Wells,1962), OH^{2-} would be bigger, because the additional magnetic electron enters an antibonding σ^{*} type molecular orbital formed from the H 1s and O^{2-} $2p\sigma$ orbitals. This orbital is the partner of the fully occupied σ type bonding orbital which holds OH^{-} together, and the presence of the additional electron reduces the bond order from 1.0 to 0.5, resulting in increased bond length, and therefore size, of OH^{2-} over OH^{-}.

Before the spin Hamiltonian parameters can be examined for evidence to reinforce the conclusion that OH^{2-} is responsible for the spectra reported here, it is necessary to consider the information which can be gained from the changes which occur in the spectrum on cooling. This is because the spin Hamiltonian parameters can only be discussed quantitatively if the direction of the supposed O-H bond is known relative to the g- and A- tensor axes. Implicit in this

FIGURE 5.5 Model for the averaging motion of OH^{2-}. x,y and z axes represent ⟨100⟩ crystal axes.

(a) Room temperature.

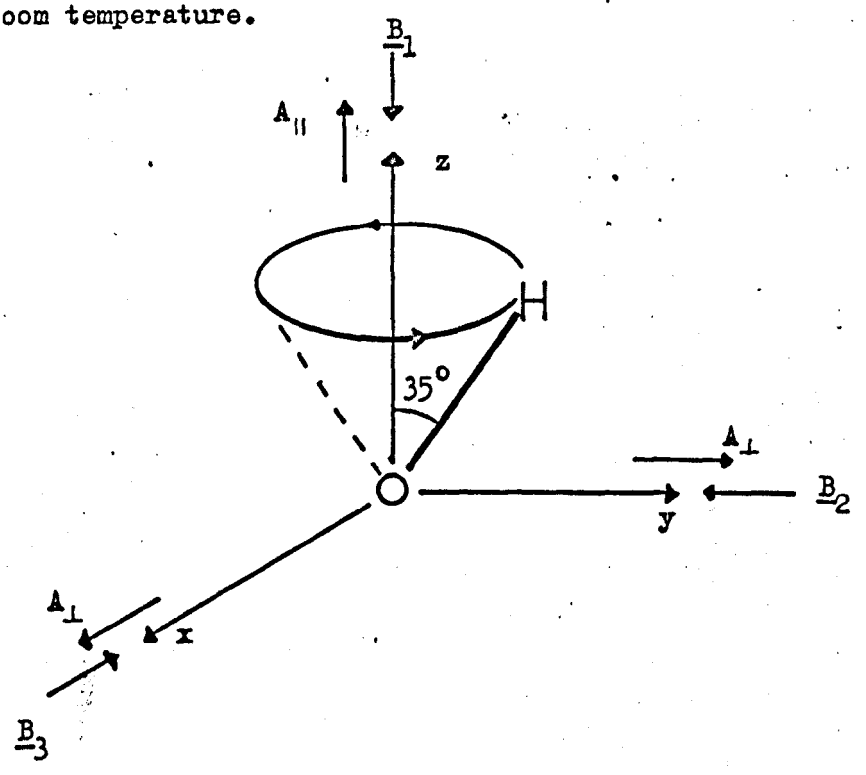

(b) 77 K

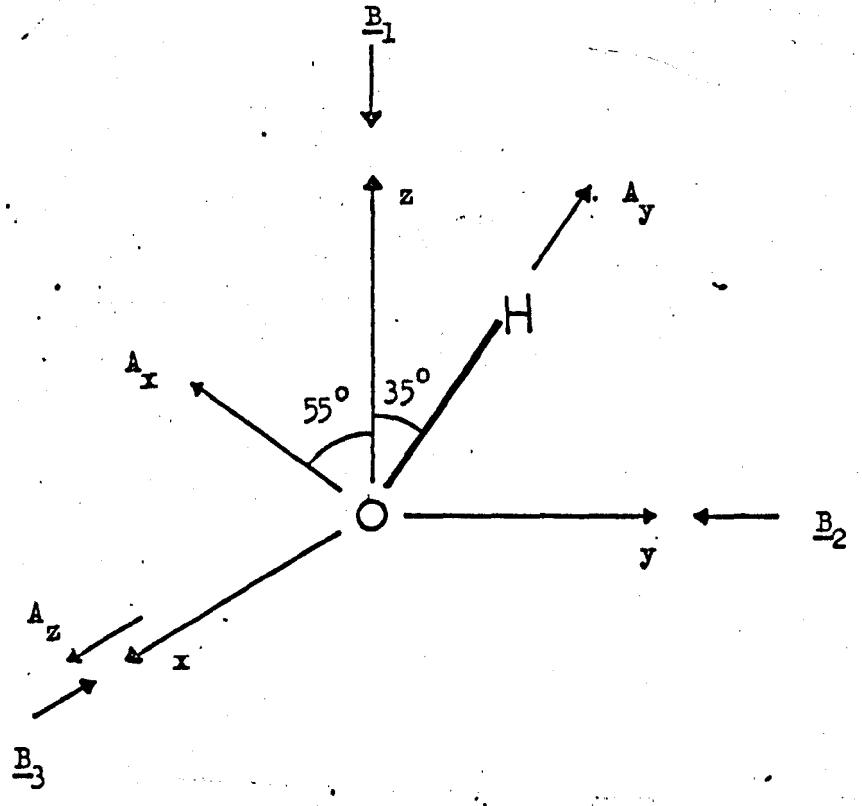

discussion is the assumption that the bond direction is coincident with the direction of one of the principal values of the g- and A-tensors. The model which best fits the experimental results is illustrated in Figure 5.5. This model bears some resemblance to the pyramidal motion of $H_A(Li^+)$ in $KCl:Li^+$ described by Schoemaker and Yasaitis (1972). At room temperature the OH bond is imagined to describe a conical surface of half angle 35° whilst the hydrogen atom moves in a circle perpendicular to a ⟨100⟩ crystal axis. The oxygen atom is fixed at its usual lattice site. Observation of this defect with the three magnetic field directions $\underline{B}_1$, $\underline{B}_2$, $\underline{B}_3$ allows the reconstruction of the actual spectrum observed for $\underline{B} \parallel \langle 100 \rangle$ in the real crystal, when the magnetic field is directed along the conical axis of some defects and is perpendicular to the axes of two other sets. When observing the defect with field $\underline{B}_1$, singly intense 'parallel' lines would be observed. Observation with fields $\underline{B}_2$ and $\underline{B}_3$ gives rise to equivalent 'perpendicular' lines twice the intensity of the 'parallel' lines. At 77 K the motion has ceased, the OH bond being frozen into a {100} plane, but still at 35° to the z axis. The most natural directions for the principal values of g and A for this defect are along the bond, along ⟨100⟩ perpendicular to the bond, and at right angles to both these. Observation of the defect with magnetic field $\underline{B}_1$ gives one of the type B EPR lines because $\underline{B}_1$ is at 35° to the direction of principal tensor components. Magnetic field $\underline{B}_2$ gives the other type B EPR lines, the field now being at 55° to the above tensor components. Type A EPR lines are observed using magnetic field $\underline{B}_3$, because this is the only direction of magnetic field which is parallel to principal values of the two tensors describing this defect. These EPR lines therefore have a turning point along ⟨100⟩ directions, and by comparison with the EPR spectrum the tensor components must be A_z and g_z. The other principal value of the A-tensor perpendicular to

the direction of the O–H bond is chosen to be A_x because its value closely matches A_z, the small difference between the two being assumed to be due to the different crystal environment in these two directions. A_y is naturally taken to be parallel to the bond because of its large value compared with the other two. Evidence for the reasonableness of this assignment can be gained from the room temperature hyperfine parameters. $A_\perp$ describes the situation roughly perpendicular to the bond, whilst $A_{||}$ describes that roughly parallel: $A_{||}$ compares favourably with A_y, and $A_\perp$ with both A_x and A_z. Two other models for OH^{2-} were considered. The first involved the hydrogen atom rotating in a $\{100\}$ plane and stopping with the O–H bond at 10° to a $\langle 110 \rangle$ direction, and the second had the bond describing a conical motion and stopping as above, but with the half angle of the cone being 55° instead of 35°. The first of these alternatives was discarded because it does not allow a perpendicular room temperature line to acquire $\langle 100 \rangle$ character on cooling, or the parallel room temperature line to acquire '35°' character, as was observed experimentally. With this model each of the room temperature perpendicular lines would split to give type B EPR lines and the parallel lines would become type A. The proposed model fulfills these conditions because the perpendicular line observed with field $\underline{B}_3$ at room temperature has a $\langle 100 \rangle$ turning point at 77 K whilst field $\underline{B}_1$ gives a parallel line at room temperature but a '35°' one at 77 K. Although the second model does comply with this condition, it was discarded because it does not allow a satisfactory comparison between the hyperfine tensor components at room temperature and 77 K.

Having established that the 77 K y-tensor components are most likely directed along the bond a discussion of the spin Hamiltonian parameters can be attempted. The 77 K hyperfine parameters can be separated into isotropic and anisotropic components

using a calculation similar to that performed in Chapter III (see Equations 3.29, 3.30). In the classical Fermi-Segre form the isotropic interaction, a, is related to the square of the wavefunction of the electron at the nucleus concerned, $|\psi(0)|^2$, by

$$a = \frac{8}{3} g \mu_B g_N \mu_N |\psi(0)|^2. \qquad 5.4$$

Here a is simply the average of the three principal hyperfine components, giving

$$a = \frac{1}{3}(A_x + A_y + A_z) = 54 \times 10^{-4} \text{ cm}^{-1}.$$

Hence

$$|\psi(0)|^2 = 0.244 \times 10^{24} \text{ cm}^{-3}.$$

This value is almost one tenth the corresponding quantity for atomic hydrogen, indicating that the magnetic electron is typically remote from the proton, a feature which correlates with it being in an antibonding molecular orbital. The anisotropic interaction, b, can be derived from the equations

$$\begin{aligned} A_y &= a + 2b \\ A_x &= a - b - b^1 \\ A_z &= a - b + b^1 \end{aligned} \qquad 5.5$$

It can be considered to depend upon the dipolar interaction between electronic and nuclear spins:

$$b = \frac{1}{6}[2A_y - (A_x + A_z)] = \frac{1}{2} g \mu_B \mu_N g_N \left\langle \psi \left| \frac{3\cos^2\theta - 1}{\underline{r}^3} \right| \psi \right\rangle \qquad 5.6$$

where $\underline{r}$ is the electron proton separation vector and θ is the angle between $\underline{r}$ and the symmetry axis y. Here $b = 0.0012$ cm^{-1}, giving

$$r = 1.3 \text{ A}$$

when $\theta = 0^\circ$. Again, this value of r correlates with the electron being in an antibonding molecular orbital, as it is 30% larger than the value of r in OH^-. This, together with the electropositive nature of the hydrogen atom, is probably sufficient to cause the molecular ion to have a stable configuration in which the O-H bond is pointing away

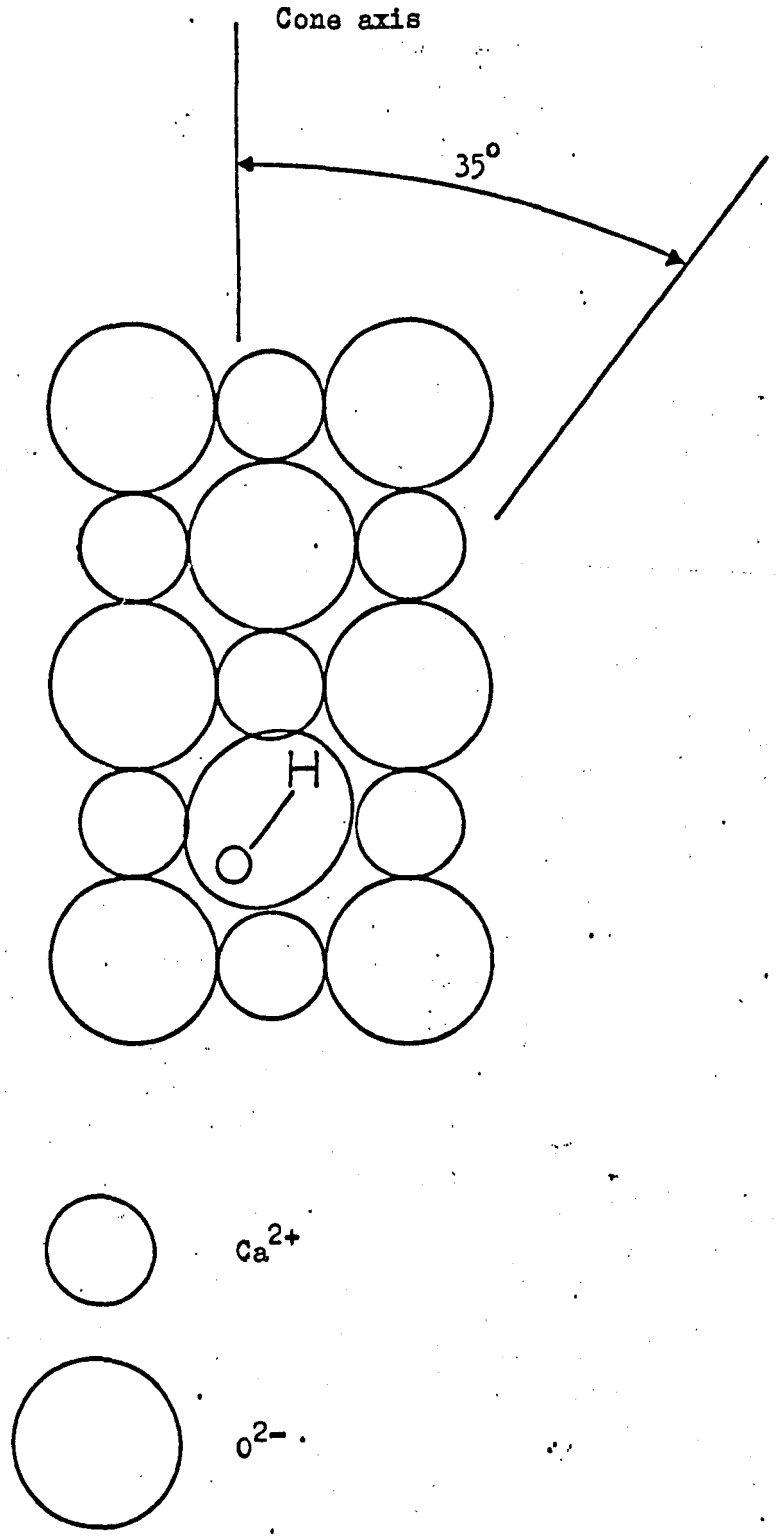

FIGURE 5.6 Schematic diagram of the model of the defect, with O–H shown in a {100} plane.

from the Ca^{2+} ion along $\langle 100 \rangle$. Inter-electron repulsion will stop the bond from being directed towards O^{2-} in a $\langle 110 \rangle$ direction, because the latter ion is 50% larger than Ca^{2+}. This situation is illustrated in Figure 5.6.

The difference in the size of the hyperfine parameters of OH^{2-} and OF^{2-} already mentioned can be explained by the difference in character between the respective σ^* anti-bonding orbitals in which the magnetic electrons are found. In particular, the anisotropic contribution is proportionately much larger in OF^{2-}, and this reflects the increased p-character in the σ^* orbital which is formed from $2p\sigma$ orbitals on both oxygen and fluorine. This is in contrast to the σ^* orbital of OH^{2-} derived from H 1s and O^{2-} $2p\sigma$ orbitals, which would also be expected to give rise to g-values near g_e. This is confirmed experimentally, the maximum departure being 0.0065.

In conclusion, it is clear that the evidence from the spin Hamiltonian parameters reinforces the conclusion that the molecular ion OH^{2-} is responsible for the observed spectra. This defect is analogous to the F centre containing a water molecule in KCl observed by Rusch and Seidel (1971), and the disappearance of its spectra on slight heating is probably due to the formation of OH^- by loss of an electron.

5.5 Activation Energy for the averaging motion

Anderson (1954) has calculated the effect of motional narrowing on EPR lines. He uses a model which assumes that the precessing magnetic moment gives rise to a radiated electromagnetic wave which is undergoing frequency-modulation because the magnetic interactions in the crystal act to change the frequency of precession. The frequency-modulation is changing in a random way in time due to the effect of the non-magnetic motions on the magnetic interaction: the Hamiltonian $\mathcal{H}_m$ describing the motional effects commutes with all

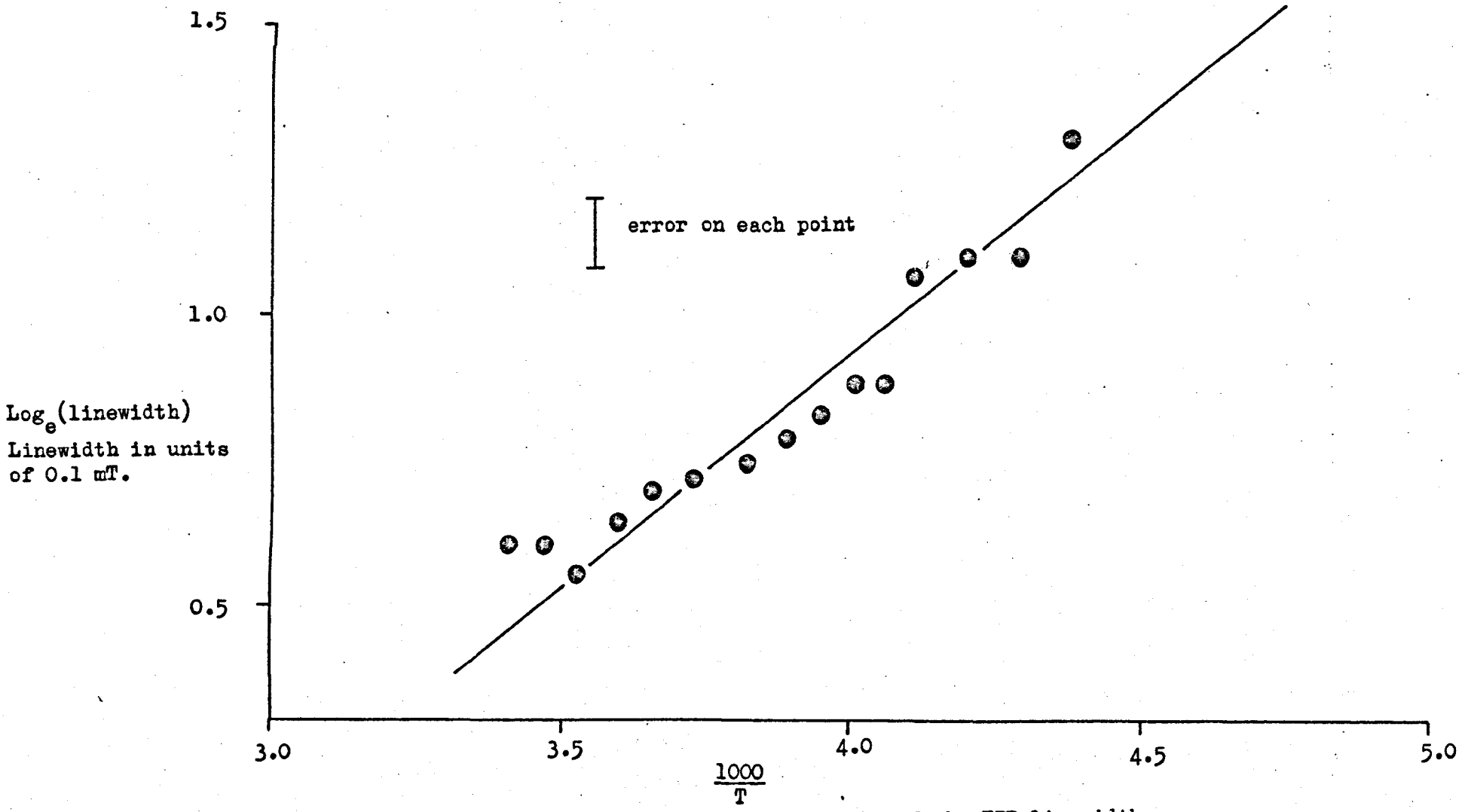

FIGURE 5.7 Plot of the natural logarithm of the EPR linewidth against reciprocal temperature in the range 210 - 300 K.

Hamiltonians describing the system except $\mathcal{H}_p$, which describes the linewidth, so $\mathcal{H}_m$ can cause $\mathcal{H}_p$ to be time dependent. For a system exhibiting hyperfine structure Andersons treatment allows two extreme cases. In the first case, when the frequency splitting between lines which coalesce dominates the frequency of reorientation, the lines should draw closer together before transferring to the opposite regime in which jumping predominates. This feature was observed experimentally at the beginning of the transition temperature range. In the reorientation dominated region to higher temperature when the lines have coalesced the linewidth is calculated to be

$$\Delta\omega = \frac{\omega_o^2}{2\omega_e} \qquad 5.7$$

where ω_o is half the frequency separation between the two lines before motional effects are observed, and ω_e the frequency of reorientation. For a normal thermally excited motion ω_e should be given by

$$\omega_e = \omega_1 \exp - \frac{E}{kT} \qquad 5.8$$

where E is the activation energy for reorientation, k is Boltzmanns constant, and T the absolute temperature. Hence

$$\Delta\omega = \frac{\omega_o^2}{2\omega_1} \exp \frac{E}{kT} \quad . \qquad 5.9$$

Clearly a graph of the linewidth against reciprocal temperature above the transition temperature will allow the activation energy to be determined. This plot is illustrated in Figure 5.7, the gradient allowing the value E = 0.07 $\pm$ 0.01 eV to be calculated. This is a typical result (Schoemaker and Shirkey,1972, Schoemaker and Yasaitis, op cit, Tohver et al,1972). From the intercept we can calculate that ω_1 = 118 MHz.

5.6 Further work

Two features of the defect reported in this chapter warrant

further study. ENDOR experiments would firstly be useful in identifying unambiguously the nucleus involved in the hyperfine structure, and secondly they would be useful for studying the reorientation process. This latter aspect could also be pursued by observing how the EPR lineshape varies with temperature.

APPENDIX A

COMPUTER PROGRAMS BY R.DOWSING

A.1 Introduction

The spin Hamiltonian, Equation 1.52, contains all the terms which are normally required to describe the results of EPR experiments. It is the meeting ground between theoretician and experimentalist, the responsibility of the latter being the determination of the parameters which describe the resonance behaviour of the experimental system with maximum accuracy. In all but the most simple situations computer programs are required for this purpose.

The eigenfunctions $|M_S, M_I\rangle$ of the Hamiltonian 1.52 are characterized by the quantum numbers M_S and M_I, which are derived from the electronic (S) and nuclear (I) spins of the experimental system; the range of M_S extends from +S to -S in steps of 1, (2S+1) values, whilst M_I ranges from +I to -I in similar steps, giving (2I+1) values. The matrix elements

$$\langle M_S', M_I' | \mathcal{H} | M_S, M_I \rangle \quad ,$$

where M_S, M_S' and M_I, M_I' may be the same or different, connect any two eigenfunctions and are arranged in a (2I+1)(2S+1) x (2I+1)(2S+1) array. This matrix is the focus for the interpretation of EPR results, and the size of its elements depends on both the magnitude and direction of the magnetic field (through the Zeeman terms), on the magnitudes of the principal values of the other interaction tensors, and on the directions of these principal values with respect to the axis system used to specify the magnetic field direction, usually the crystal field axis system.

In minimisation program MNES all the matrix elements are found at every value of the magnetic field, in both magnitude and direction, at which an EPR transition was observed. Once generated,

the matrix is diagonalized to find the eigenvalues, and in this process the eigenvectors become linear combinations of the original $|M_S, M_I\rangle$ functions. For a particular value of B, the energy difference between levels connected by a transition probability greater than a specified level which is closest to the energy of the incident microwave quantum is considered to be the transition which was actually observed. Alternatively the energy levels involved in this transition can be specified in the input data by labels indicating their relative energy. The discrepancy between the energy of the incident quantum and the energy gap between the levels measures the closeness of the fit, and this procedure is repeated for every transition at various angles of the magnetic field to gauge the overall quality of the fit. Alteration of the starting parameters and the orientations of the axis systems to which they are referred allows a best fit to be determined . This iteration can be either mechanical, or it can be programmed. In MNES a subroutine performs the minimisation without calculating derivatives (Powell,1965): parameters and angles are varied cyclically one at a time, in an order specified by the operator, until the sum of the absolute values of the energy deviations between calculated and observed transitions is a minimum.

An alternative approach, used in program ESRS, involves calculating the magnetic field positions at which transitions would be observed for a given set of parameters and axis systems. The program operates by calculating the matrix elements at incremental magnetic field values for a given magnetic field direction (which can also be varied). Following diagonalization at two consecutive field values, the change in sign of the energy difference between two levels compared with the energy of the incident quantum indicates that in the last magnetic field gap a 'transition' has occurred, and the exact field value is obtained by interpolation. The transition probability

is then calculated and printed out together with the field value, the eigenfunctions of the two levels involved, and the position of these levels in a list of all the levels arranged in descending order. At each orientation of B energy differences between all the levels are examined. ESRS allows a spectrum to be reconstructed from given parameters, and this is a useful facility which increases the power of the minimisation programs, with which it is used, by helping to avoid ambiguity. Alternatively this program can be used alone to find a best fit to the results by mechanical iteration.

A.2 Programming details

The most important parts of an ESR program are the subroutines which calculate the matrix elements and diagonalize the resultant matrix, because these operations are performed many times during a run. For example, a six line spectrum examined at ten different angles requires 60 such operations for a given set of parameters. In a complete minimisation run the operations would be performed approximately 200,000 times. In both MNES and ESRS the matrix elements are calculated in subroutine TSETUP, and the matrix is diagonalized in subroutine EIGEN.

A.2.1 SUBROUTINE TSETUP

This subroutine is always called via subroutine TENSYS. TENSYS converts principal values of all the interaction tensors, g, g_N, A, D, A_L, Q, into components referred to an appropriate axis system (specified by Euler Angles) by calling subroutines TFORM (which generates the transformation matrix) and TENSOR, which performs the rotation. The principal values are specified in the input data, but in MNES they are varied by minimisation subroutine VA04A. Rotation angles can also be varied by VA04A if this is required, but usually the magnetic field is specified with respect to the symmetry axes of the

centre rather than those of the crystal, making this unnecessary. Tensor components transformed into appropriate axis systems are passed to TSETUP, in which all necessary spin matrices are calculated using subroutines XYMAT (generates S_x, S_y and S_z matrices) and MATMPY (multiplies two matrices to form S_x^2, S_xS_z, S_x^4, S_y^6 etc.). Matrix elements A(I,J) are calculated by cycling I and J over a range determined by S, I, and including in each only those interactions which give non-zero contributions. Furthermore, only non-zero matrix elements are calculated to save time i.e. elements A(I,J) involving spin operators O_4^4 and O_6^4 are calculated only when I = J + 4 or I = J - 4. The incorporation of 8 x 8 spin matrices and additional fourth and sixth order terms into this subroutine were the major changes made by the author to the programs.

A.2.2 SUBROUTINE EIGEN

Matrix elements containing S_y are typically imaginary, but these elements are arranged in a separate part of matrix A as real quantities. Imaginary contributions to element A(I,J) are placed in A(I,J+N), where N is the dimension of the matrix. This results in a matrix of dimension N x 2N, but the size is doubled to give a square array by the relations

$$A(I + N) = A(I, J + N) \qquad A2$$

$$A(I + N, J + N) = A(I,J) \quad . \qquad A3$$

This procedure is adopted because the eigenvalues of the actual matrix

$$\left[(x,z) + iy\right] \quad , \qquad A4$$

which is complex Hermitean, can be found by diagonalizing

$$\left[\begin{array}{c|c} (x,z) & -y \\ \hline y & (x,z) \end{array}\right] \quad , \qquad A5$$

which is real symmetric, and the operation is much easier to perform. The eigenfunctions of A4 are the set u + iv. The eigenvalues of A4 occur as degenerate pairs in the solution to A5, in which the

corresponding eigenfunctions are one of the set u and +v with one of the set v and -u (Greenstadt,1962). Diagonalization is performed using the method originated by Jacobi and adapted by von Neumann (1962) for large computers.

A.2.3 Transition probabilities

Transition probabilities are calculated using Equation 1.54 in subroutines TPROB and SIMP, a facility being incorporated for fixing the direction of the microwave magnetic field with respect to both the static field (normally 90^{o}) and the crystal axis system.

REFERENCES

von Neumann (1962) Mathematical Methods for Digital Computers (Ch.7) Ed. A.Ralston & H.S.Wilf, Wiley, New York.

J.Greenstadt (1962) In the above volume.

REFERENCES

Abragam,A. and Bleaney,B. (1970) "EPR of Transition Ions" OUP.

and Pryce,M.H.L. (1951) Proc.Roy.Soc. A 206, 164 .

Anderson,P.W. (1954) J.Phys.Soc.Jap. 9, 316 .

Azarbayejani,Y.G.H. (1965) Bull.Am.Phys.Soc. 10, 1131.

and Merlo,A.L. (1965) Phys.Rev. 137, 4489.

Bessent,R.G. and Hayes,W. (1965) Proc.Roy.Soc. A 285, 430.

Beswick,J.R. (1973) Ph.D. Thesis, University of Keele.

Bleaney,B., Bowers,K.D. and Pryce,M.H.L. (1955) Proc.Roy.Soc. A 228, 166.

Birchurin,M.I. et al (1971) Soviet Phys.-Solid State 13, 594.

Buckmaster,H.A. and Shing,Y.H. (1972) Phys.Stat.Sol.(a) 12, 325.

Chu,K.C. and Kikuchi,C. (1965) Bull.Am.Phys.Soc. 10, 614.

Cotton,F.A. and Wilkinson,G. (1966) "Advanced Inorganic Chemistry", Interscience.

Dowsing,R.D. (1970) Program communicated by its Author.

Emons,H-H. (1963) Zeit.anorg.Chem. 323, 114.

Figgis,B.N. (1966) "Introduction to Ligand Fields",Wiley, London.

Freeman,A.J. and Watson,R.E. (1965) in "Magnetism" Vol.IIa, Ed.G.T.Rado and H.Suhl. Academic Press.

Freeman,A.J. and Watson,R.E. (1967) "Hyperfine Interactions" p.53, Academic Press.

Garrison,A.K. and DuVarney,R.C. (1971) Phys.Stat.Sol.(b) 45, 259.

Griffiths,J.S. (1961) "Theory of Transition Metal Ions", CUP.

Hall,T.P.P. (1973) Private communication to Dr.B.Henderson.

Hempstead,C.F. and Bowers,K.D. (1960) Phys.Rev.118, 131.

Henderson,B. (1965). Unpublished.

and Codling,A.J.B. (1971) J.Phys.C. 4, 1409.

et al. (1971) J.Phys.C. 4, 1409.

and Sibley,W.A. (1971) J.Chem.Phys. 55, 1276.

and Tomlinson,A.C. (1969) as in latters Ph.D. Thesis, University of Keele.

Henderson,B.,Kolopus,J.L. and Unruh,W.P. (1971) J.Chem.Phys. 55, 3519.

and Wertz,J.E. (1968) Advances in Physics 17, 749.

Hughes,A.E. and Henderson,B. (1972) in "Point defects in solids, Vol.I" Ed. J.H.Crawford & L.M.Slifkin. Plenum.

Hutchings,M.T. (1964) Solid State Physics 16, 227.

Jahn,H.A. and Teller,E. (1937) Proc.Roy.Soc. A 161, 220.

Kedzie,R.W. et al. (1964) Phys.Lett. 11, 286.

Kirton,J. (1965) Phys.Rev. 139, A1930.

Kramers,H.A. (1930) Proc.Acad.Sci.Amsterdam 33, 959.

Lederer,L.M.,Hollander,J.M. and Perlmann,I. (1967) "Table of Isotopes", 6th. Edition, John Wiley, New York.

Lingam,K.V. et al. (1969) Proc.Ind.Acad.Sci. 70(1), 29.

Low,W. and Rubins,R.S. (1963) Phys.Rev. 131, 2527.

Mims,W.B. (1965) Phys.Rev. 140, A531.

and Gillen,R. (1966) Phys.Rev. 148, 438.

O'Connor,J.R. and Chen,J.H. (1964) App.Phys.Lett. 5, 100.

O'Mara,W.C.,Davies,J.J. and Wertz,J.E. (1969) Phys.Rev. 179, 816.

and Wertz,J.E. (1970) Solid State Comm. 8, 807.

Orton,J.W. (1968) "Electron Paramagnetic Resonance" Iliffe Books.

Owen,J. and Thornley,J.H.M. (1966) Rep.Prog.Phys. 29, 675.

Powell,M.J.D. (1965) Computer Journal 7, 303.

Reynolds,R.W. et al. (1972) J.Chem.Phys. 56, 5607.

Rusch,W. and Seidel,H. (1971) Solid State Comm. 9, 231.

Rius,G. and Cox,R. (1968) Phys.Lett. 27A, 76.

Schoemaker,D. and Shirkey,C.T. (1972) Phys.Rev.B. 6, 1562.

and Yasaitis,E.L. (1972) Phys.Rev.B. 5, 4970.

Schrimer,O.F. (1970) J.Phys.Chem.Solids 32, 499.

Shuskus,A.J. (1962) Phys.Rev. 127, 2022.

(1963) J.Chem.Phys. 39, 849.

Stoneham,A.M. (1969) Rev.Mod.Phys. 41, 82.

Tohver,H.T. et al. (1972) Phys.Rev.B. 5, 3276.

Uitert,L.G. van and Soden,R.R. (1960) J.App.Phys. 31, 328.

Unruh,W.P. (1971) J.Phys.C. 4, 2992.

Chen,Y. and Abraham,M.M. (1973) Private comm. to Dr.B.Henderson.

Weightman,P. (1968) Ph.D. Thesis, University of Keele.

et al. (1972) Phys.Stat.Sol.(b) 49, 221.

et al. (1973) Phys.Stat.Sol.(b) 58, 321.

Wells,A.F. (1962) "Structural Inorganic Chemistry", OUP.

Wertz,J.E. and Auzins,P.V. (1957) Phys.Rev. 106, 484.

(1967) J.Phys.Chem.Solids, 28, 1557.

Whiffen,P.A.C. and Orton,J.W. (1965) Br.J.App.Phys. 16, 567.

Wilkens,J.,de Graag,D.P. and Helle,J.N. (1965) Phys.Lett. 19, 178.

Wycoff,R.W.G. (1960) "Crystal Structure", Wiley, New York.